# Atomistic Simulation of Shock Waves: From Simple Crystals to Complex Quasicrystals

Habilitationsschrift zur Erlangung
der Lehrbefugnis für das Fach Theoretische Physik
an der Universität Stuttgart

vorgelegt von
Johannes Roth
aus Großbottwar

Institut für Theoretische und Angewandte Physik
Universität Stuttgart
2005

*To Antje,*
*Jonathan,*
*Stephan,*
*and Althea*

## A shock wave in the wild west

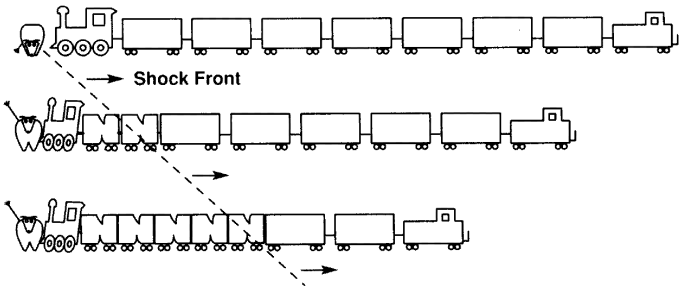


From [25]

Parts of this work have been published already:

J.Roth, R.Schilling, H.-R.Trebin, Stability of monoatomic and diatomic quasicrystals and the influence of noise, *Phys.Rev.B* **41** (1990) 2735.
J.Roth, Comment on Formation of a dodecagonal phase in a simple monatomic liquid, *Phys.Rev.Lett.* **49** (1997) 4042.
J.Roth, F. Gähler, Self-diffusion in dodecagonal quasicrystals, *Eur.Phys. J.B* **6** (1998) 425.
M.Hohl, J.Roth, H.-R.Trebin, Correlation functions and the dynamical structure factor of quasicrystals, *Eur.Phys.J.B* **71** (2000) 595.
J.Roth, The fluid-solid transition of Dzugutov's potential, *Eur.Phys.J.B* **14** (2000) 449.
J.Roth, Jumps in icosahedral quasicrystals, *Eur.Phys.J.B* **15** (2000) 7.
J.Roth, Shock waves in quasicrystals, *Mat.Sci.Eng.A* **294-296** (2000) 753.
J.Roth, A.Denton, Solid phase structures for the Dzugutov pair potential, *Phys.Rev.E* **61** (2000) 6845.
G.Schaaf, J.Roth, H.-R.Trebin, R.Mikulla, Numerical simulation of dislocation motion in three-dimensional icosahedral quasicrystals, *Phil. Mag.A* **80** (2000) 1657.
J.Roth, Shock waves in quasicrystals, *Ferroelectrics* **250** (2001) 365.
J.Roth, Large-scale molecular dynamics simulations of shock waves in Laves-crystals and icosahedral quasicrystals, *AIP Conf.Proc.* **620**, (2002) 378.
G.Schaaf, J.Roth, H.-R.Trebin, Dislocation motion in icosahedral quasicrystals at elevated temperatures: Numerical simulation, *Phil.Mag.* **83**, (2003) 2449.
J.Roth, Shock waves and solitary waves in bcc crystals, *AIP Conf.Proc.* **706** (2004) 302.
J.Roth, Shock Waves in Complex Binary Solids: Cubic Laves Crystals, Quasicrystals, and Amorphous Solid, *Phys.Rev.B* **71** (2005) 064102.
J.Roth, Shock Waves in Materials with Dzugutov-Potential Interaction, *Phys.Rev.B* **72** (2005) 014125.
J.Roth, $\omega$-Phase and Solitary Waves Induced by Shock Compression of BCC Crystals, *Phys.Rev.B* **72** (2005) 014126.

# Contents

# List of Symbols

This list contains the more frequently used symbols. A more detailed explantation may be found in the sections where the symbols are introduced.

**Variables and Parameter**

| | |
|---|---|
| $a$ | half the edge length of the tiles |
| $b$ | in-plane lattice constant of the $\omega$-phase |
| $b_0$ | equilibrium in-plane lattice constant of the $\omega$-phase |
| $c$ | arbitrary velocity of sound |
| $c_{11}$, $c_{12}$ | elastic constants of an isotropic material |
| $c_b$ | bulk velocity of sound: $c_l = \sqrt{K/\rho}$ |
| $c_l$ | longitudinal velocity of sound: $c_l = \sqrt{F/\rho}$ |
| $c_t$ | transversal velocity of sound: $c_l = \sqrt{G/\rho}$ |
| $c_x$ | velocity of sound for structure or direction $x$ |
| $d$ | perpendicular lattice constant of the $\omega$-phase |
| $d_0$ | equilibrium perpendicular lattice constant of the $\omega$-phase |
| $E_{\mathrm{pot}}$ | potential energy |
| $E_x$ | potential energy of structure $x$ |
| $F$ | uniaxial elastic constant |
| $G$ | shear modulus |
| $K$ | bulk compressibility |
| $kT$ | temperature in energy units |
| $k_0$ | reciprocal lattice constant along the three-fold axis of bcc |
| $P$ | hydrostatic pressure: $P = (P_{xx} + P_{yy} + P_{zz})/3$ |
| $P_0$ | unit of pressure and stress: $P_0 = \epsilon/a^3$ |
| $P_{ii}$ | uniaxial pressure (stress) along direction $i$ |
| $r_{ab}$ | distance between an atom of type $a$ and an atom of type $b$ |
| $r_C$ | cut-off radius |
| $r_s$ | relative strength $v_d/v_e$ |
| $S$ | shear pressure (stress): $S = P_{xx} - (P_{yy} + P_{zz})/2$ |

| | |
|---|---|
| $S_e$ | shear pressure (stress) at the end of the sample |
| $S_p$ | peak shear pressure (stress) |
| $t$ | time |
| $t_0$ | unit of time: $t_0 = a\sqrt{m/\epsilon}$ |
| $T$ | temperature |
| $t_r$ | time to ramp up the piston velocity |
| $u$ | unspecified shock front velocities |
| $u_i$ | velocity of the flyer plate |
| $u_p$ | piston velocity |
| $u_{p,\mathrm{eff}}$ | effective piston velocity |
| $u_s$ | in a closer sense: shock wave velocity, frequently used for all types of wave velocities |
| $v_0$ | unit of velocity: $v_0 = \sqrt{\epsilon/m}$ |
| $v_d$ | potential minimum for diagonal interactions |
| $v_e$ | potential minimum for edge interactions |
| $w$ | position of the $B$ and $C$ layers with respect to the lattice constant $d$ in bcc and the $\omega$-phase |
| $Y$ | yield stress |
| $\epsilon$ | energy unit |
| $\epsilon_{ij}$ | strain tensor |
| $\Delta t$ | time interval |
| $\lambda$, $\mu$ | Lamé constants |
| $\nu$ | Poisson ratio |
| $\rho$ | density |

**Reduced Units**

Reduced units are used throughout the thesis. Lengths are given in $a$, and energies in $\epsilon$. All other units are converted into $a$, $\epsilon$ and the mass $m$. Thus there are the following relations: $t_0 = a\sqrt{m/\epsilon}$, $v_0 = \sqrt{\epsilon/m}$, and $P_0 = \epsilon/a^3$

# Deutsche Zusammenfassung

**Übersicht**

Diese Habilitationsschrift handelt von Molekulardynamiksimulationen an geordneten Festkörpern. Im ersten Teil werden die Grundlagen der Stoßwellenphysik kurz zusammengefasst, gefolgt von einem Überblick über die Simulation von Stoßwellen in Festkörpern. Ein weiterer Abschnitt enthält die Beschreibung der untersuchten Strukturen, Wechselwirkungen und relevanten Phasendiagramme.
Im zweiten Teil der Arbeit folgt die Beschreibung der Ergebnisse: Im ersten Kapitel werden binär ikosaedrische Quasikristalle und verwandte Laves-Phasen behandelt, im zweiten monoatomar zwölfzählige Quasikristalle, eng verwandte tetraedrisch dicht gepackte Phasen und kubisch innenzentrierte Kristalle. Das dritte Kapitel handelt von der intermediären $\omega$-Phase und solitären Wellen, die in den innenzentrierten Kristallen bei Stoßwellen entlang von dreizähligen Symmetrierichtungen auftreten.
In allen Fällen gibt es drei Bereiche unterschiedlichen Materialverhaltens: bei schwachen Stoßwellen findet man elastische Deformationen, in einem mittleren Bereich elastische und plastische Deformation bzw. Phasenübergänge. Im Bereich starker Stoßwellen werden die Ausgangsstrukturen amorphisiert.

**Stoßwellenphysik in Festkörpern**

Stoßwellen treten überall im Universum und in allen Zuständen der Materie auf. Man findet sie sowohl in der Bugwelle der Heliosphäre oder in Supernovaexplosionen als auch bei der Sonolumineszenz und beim Überschallknall.
Stoßwellen existieren auch in Festkörpern und ermöglichen dort die Untersuchung von Materiezuständen, die mit anderen Methoden nicht erreicht werden können:

- die Bestimmung der Zustandsgleichung bei sehr hohen Drücken und Temperaturen wie zum Beispiel im Erdinnern,
- die Untersuchung des mechanischen Verhaltens von Festkörpern bei plötzlichen Lastwechseln,
- die Analyse dynamischer Phasenübergänge, die an den Stoßwellenfronten auftreten.

- In Simulationen ermöglichen sie die Untersuchung von ausgedehnten Defekten wie Versetzungen und Stapelfehler, die sonst künstlich eingebaut werden müssten. Dieses Vorgehen spielt insbesondere bei komplexen Kristallstrukturen und Quasikristallen eine Rolle.

Eine Stoßwelle (Abs.1.2) ist definiert als eine sich fortbewegende Unstetigkeit der thermodynamischen Größen. Stabile Stoßwellen propagieren mit Überschallgeschwindigkeite bezüglich des Ausgangsmediums und langsamer als der Schall im komprimierten Medium. In Gasen und Flüssigkeiten stellen diese Definitionen wegen der fehlenden Rückstellkräfte kein Problem dar, wohl aber in Festkörpern. Hier versteht man unter einer Stoßwelle eine permanente Änderung von Atompositionen, das heißt es muss Plastizität oder Phasenübergänge auftreten. In dieser Arbeit haben wir uns allerdings nicht an diese rigorose Definition gehalten, sondern alle abrupten Änderungen thermodynamischer Größen als Stoßfronten bezeichnet.

Grundlage der Stoßwellenphysik sind die Rankine-Hugoniot-Gleichungen (Abs.1.5). Sie stellen nichts anderes dar als eine Umformulierung der Erhaltung von Masse, Impuls und Energie über die Stoßfront hinaus. Ursache ist die unterschiedliche Materiegeschwindigkeit auf beiden Seiten der Stoßfront.

Im Festkörper (Abs.1.6) können wegen der endlichen Festigkeit mehrere Wellen entsehen. bei schwachen Stoßwellen findet nur eine elastische Verformung statt. Ist die Welle stärker als die elastische Hugoniotgrenze (HEL), so folgt nach der elastischen Welle eine plastische oder eine Phasenumwandlung. bei starken Stoßwellen sind elastische und plastische Front nicht mehr unterscheidbar. Im Bereich des elastisch-plastischen Schocks ist die Stoßwelle nicht stationär.

In den Simulationen spielt auch die Dimensionalität der Stoßwelle eine wichtige Rolle (Abs.1.10): Ist die Temperatur zu niedrig oder der Anfangszustand nicht äqulibriert, so fehlt die Koppelung der Bewegung longitudinal und transversal zur Stoßwelle. Das System verhält sich rein eindimensional, es tritt keine Thermalisierung eine lineares Anwachsen der Stoßfrontdicke und starke Solitonen auf. Dieses Verhalten ist nicht zu verwechseln mit dem in Kapitel 6 berichteten Auftreten von solitären Wellen.

### Simulation von Stoßwellen in Festkörpern

Simulationen von Stoßwellen in Festkörpern (Abs.2.1) haben vor etwa vierzig Jahren begonnen. Wegen der begrenzten Rechnerleistung wurden Vereinfachungen gemacht, die dazu führten, dass die Strukturen sich wie im vorigen Abschnitt beschrieben eindimensional verhielten, was zu der (falschen) Ansicht führte, dass es in Festkörpern gar keine Stoßwellen gäbe. Im Laufe der Zeit konnte gezeigt werden, dass Stoßwellen in Festkörpern existieren und zu Plastizität durch Abscherung führen. Im Jahre 1998 gelang schließlich der Durchbruch mit der ersten Simulation eines flächenzentriert kubischen Kupferkristalls mit mehreren Millionen Atomen. Erstmls konnten einzelne Stapelfehler isoliert werden. Seither hat man eine Vielzahl neuer und unerwarteter Phänomene wie nichtstationäre Stoßwellen, verschiedene Phasenübergänge und solitäre Wellen gefunden und konnte beispielsweise Modelle der Entstehung von Plastizität durch Versetzungen überprüfen.

Für die Simulation von Stoßwellen in Festkörpern werden Standard-Molekulardynamikprogramme eingesetzt (Abs.2.4). Der Ausgangszustand sollte gut äquilibriert sein, was mit Hilfe von isothermen und isotherm-isobaren Ensembles erreicht wird. Die eigentlichen Simulationen werden mikrokanonisch durchgeführt.

Zur Erzeugung der Stoßwellen werden mehrere Methoden verwendet (Abs.2.2): zwei Klötze werden mit konstanter Geschwindigkeit aufeinander zubewegt, sobald sie sich treffen, entstehen im Zentrum zwei Stoßwellenfronten. Man kann das Verfahren modifizieren indem man einen der Klötze durch einen Spiegel ersetzt, der alle Teilchenimpulse umkehrt. Quer zur Stoßwellenrichtung werden periodische Randbedingungen verwendet um ein Auseinanderbrechen der Probe zu verhindern.

### Strukturen und Potentiale

Ein Ausgangspunkt dieser Arbeit war die Frage, ob sich die Auswirkung von Stoßwellen in aperiodisch geordneten Quasikristallen und in Kristallen unterscheidet. In Quasikristallen sind beispielsweise zusätzliche lokalisierte und ausgedehnte Defektmoden möglich (Abs.3.1).

Die Simulation von Stoßwellen stellt hohe Anforderungen an simulierbare Modellstrukturen: es sollten vergleichbare quasikristalline und kristalline Strukturen existieren, die Modelle sollten möglichst stabil sein, die Ergebnisse, insbesondere eventuelle Defekte, gut analysierbar wer-

den können und brauchbare Wechselwirkungen sollten bekannt sein.

Alle untersuchten Modelle sind tetraedrisch dicht gepackt (Abs.3.2). Simuliert wurden binär ikosaedrische Quasikristalle wie sie experimentell als (AlCu)Li und (AlZn)Mg bekannt sind und vereinfacht als Dekoration von Rhomboedern dargestellt werden können. Da bisher keine realistischen Wechselwirkungen bekannt waren, wurden Lennard-Jones-Potentiale verwendet. Die Potentialparametern wurden an die Geometrie angepasst. Als kristallinen Vergleichsstruktur wurde die kubische Laves-Phase untersucht, die zum Beispiel bei $MgCu_2$ auftritt.

Stabile monoatomare ikosaedrischen Quasikristallmodelle sind nicht bekannt. Die einzige Struktur, die sich für Stoßwellensimulationen eignet, ist ein zwölfzähliger Quasikristall. Hier existiert ein Modell, das aus dekorierten Drei- und Viereckprismen besteht und in der dritten Dimension periodisch ist. Der Quasikristall wird durch das Dzugutov-Potential (Abs.3.4) stabilisiert und wurde bei Abkühlsimulationen aus einer Schmelze entdeckt. Das Minimum des Dzugutov-Potentials gleicht dem Lennard-Jones-Potential, aber es existiert noch ein Maximum, das verhindern soll, dass sich bei Abkühlsimulationen flächenzentriert kubische Kristalle bilden. Die Prismen lassen sich zu vielen kristallinen und aperiodischen tetraedrisch dicht gepackten Phasen zusammenbauen und durch rhombische und hexagonale Prismen ergänzen. Eine der kristallinen Phasen, die sogenannte $\sigma$-Phase, kann als Approximant verstanden werden und ist stabiler als der Quasikristall.

Die Suche nach Grundzuständen für das Dzugutov-Potential (Abs.3.4.3) zeigt jedoch, dass im Gegensatz zu den beim Abkühlen entstehenden Strukturen eine ganz andere Phase, nämlich ein kubisch innenzentrierter Kristall, bei $T = 0$ und $P = 0$ stabiler als alle anderen Phasen ist.

Bei den Stoßwellensimulationen wurde eine weitere Phase beobachtet, die $\omega$-Phase (Abs.3.5). Bekannt ist sie heutzutage als die Struktur von $MgB_2$, sie tritt auch bei den Elementen Ti, Zr und Hf und bei vielen Legierungen auf. Die $\omega$-Phase entsteht aus innenzentriert kubischen Kristallen, wenn zwei der drei Gitterebenen parallel zur dreizähligen Achse zusammenfallen. Diese Phasenumwandlung wird verursacht durch eine allgemeine Instabilität innenzentriert kubischer Kristalle bei Verformung entlang dieser Richtung.

### Stoßwellen in kubischen Laves-Phasen und binär ikosaedrischen Quasikristallen

Vergleicht man das elastische Verhalten von Kristall und Quasikristall (Abs.4.4.1), so stellt man wie erwartet fest, dass der Kristall anisotrop ist, während sich der Quasikristall isotrop verhält.

Eine gute Übersicht (Abs.4.4.3) über die Ergebnisse erhält man aus dem Hugoniotdiagramm, das ist die Auftragung der Geschwindigkeiten der Wellenfronten, auch Pistongeschwindigkeit genannt, gegen die Geschwindigkeit, mit der die Klötze sich bewegen. Man beobachtet drei Bereiche, die allerdings oft nicht scharf abgegrenzt sind: ein elastischer Bereich, ein Bereich zweier Wellenfronten (elastisch-plastisch) und ein rein plastischen Bereich. Auch bei den Geschwindigkeiten der plastischen Wellen findet man den Unterschied in der Anisotropie zwischen Kristall und Quasikristall. In der Arbeit wird insbesondere der Bereich mittelstarker elastisch-plastischer Stoßwellen genauer untersucht. Bei sehr starken Stoßwellen tritt vollständige Fragmentierung auf, ein Verhalten, das vollständig unabhängig von der Ausgangsstruktur und deshalb für die Untersuchung von Defektstrukturen nicht besonders interessant ist.

Bei den Laves-Kristallen (Abs.4.4.7) zerbricht der Ausgangskristall in Kristallite, die gegen einander verdreht sind. Die Grenzen der Kristallite laufen diagonal durch den Kristall und sind bis zu zehn Atomabständen dick. Die entstehenden Strukturen lassen sich besser untersuchen, wenn der Kristall nach dem Durchlaufen der Stoßwelle abgeschreckt wird, denn dann verschwinden die Verdrehungen. Das Zerbrechen setzt direkt an der elastische Hugoniotgrenze (HEL) ein. Mit steigender Stoßwellenintensität wird die Fragmentierung immer feiner und geht kontinuierlich in den Bereich starker Stoßwellen über.

Bei den Quasikristallen (Abs.4.4.8) findet man grundsätzlich ein analoges Verhalten, allerdings treten hier zusätzliche Defekte auf. Verwendet man das vereinfachte Quaskristallmodell, so beobachtet man Ringprozesse bei denen fünf Atome auf alternative Positionen springen. Dieses Verhalten ist schon ohne Stoßwellen vorhanden, wird aber durch die Stoßwellen intensiviert. Mit steigender Stoßwellenstärke degenerieren die Ringprozesse erst zu Ketten, dann zu Netzen, und durchziehen schließlich das ganze Material. Letzten Endes führt dieses Verhalten zu einer Ausschmierung der elastischen Hugoniotgrenze und zu einem kon-

tinuierlichen Übergang zwischen elastisch und elastisch-plastisch. Verwendet man ein verbessertes Quasikristallmodell, so verschwinden die Ringprozesse und es gibt nur noch einzelne Sprünge der Atome. Die Stabilität der Proben wird erhöht und das Verhalten dem des Laves-Kristalls ähnlicher.
Zusammenfassend kann man sagen, dass sich die hier simulierten binären Kristalle und Quasikristalle weitgehend wie ionische Materialien verhalten. Erklären kann man dies durch die Wahl der Potentialparameter. Bei den Quasikristallen wurden zusätzliche Defekte gefunden, die zu einer Schwächung des Materials führen. Da die Ringprozesse aber nicht zu einer Änderung der Zellstruktur der Quasikristalle führen, kann man sie nicht als quasikristallspezifische Defekte auffassen. Sie können auch in anderen komplexen Kristallstrukturen mit partieller Besetzung von Gitterplätzen aufteten.

**Stoßwellen in Materialien, die über Dzugutov-Potentiale wechselwirken**

Auch bei den monoatomaren Strukturen wurde zunächst das elastische Verhalten untersucht. Die Quasikristalle sind in der quasiperiodischen Ebene isotrop, senkrecht dazu aber nicht. Alle anderen Strukturen sind wie erwartet anisotrop.
Die Ergebnisse sollen wieder anhand des Hugoniotdiagramms (Abs.5.4.2) dargestellt werden. Auf den ersten Blick sieht es so aus, als ob es hier nur den elastisch-plastischen und den plastischen Bereich gäbe. Dies liegt am Phasendiagramm: schon bei schwachen Stoßwellen tritt ein Übergang von den Ausgangsstrukturen zu dichten Kugelpackungen auf, also den Phasen, die nach Konstruktruktion des Dzugutov-Potentials eigentlich ungünstig sein sollten. Deshalb taucht der elastische Bereich im Phasendiagramm gar nicht auf. Da das Potential sehr kurzreichweitig ist, ist die Stapelfolge in den dichtgepackten Phasen zufällig und nicht rein kubisch flächenzentriert oder hexagonal dicht gepackt.
Es wurden viele Ausgangsstrukturen und -orientierungen untersucht. Die detaillierten Ergebnisse können hier nicht im Detail geschildert werden (Abs.5.4.3). Ausgezeichnet ist die vierzählige Richtung bei innenzentrierten Ausgangskristallen: hier findet der Phasenübergang innerhalb ein- bis zwei Atomlagen statt und führt zu fast defektfreien Einkristallen oder Zwillingen. Mit zunehmender Stoßwellenintensität treten aber mehr und mehr Defekte auf. Bei anderen Ausgangsstruk-

turen und -orientierungen verschieben oder drehen sich oft die Atomebenen senkrecht zur Stoßwellenrichtung. Die Ausgangsordnung bricht in mehreren Stufen zusammen, und es entstehen dicht gepackte Kristalle mit vielen Defekten, die nur langsam ausheilen. Verwendet man den Impulsspiegel in der Simulation, so wirkt dieser als Keim für fast defektfreie Kristallschichten. Für die Analyse der entstandenen Strukturen wurden vor allem radiale und Winkelverteilungsfunktionen eingesetzt.
Spezielle Phänomene beobachten man bei Quasikristallen und Approximanten, wenn die Stoßwellenrichtung in der Grundebene der Struktur liegt (Abs.5.4.5): In diesem Fall treten zwischen der elastischen und der plastischen Stoßwellenfront Flips auf, das heißt die Zellstruktur ändert sich. Zusätzlich zu den Dreiecks- und Viereckseprismen findet man rhombische und hexagonale Prismen, die sich als Verallgemeinerung der Ausgangszellen verstehen lassen und bei Flips in Quasikristallen auftreten müssen.
Die Simulationen mit Dzugutov-Pontentialen lassen sich überraschenderweise qualitativ mit Stoßwellensimulation an Eisen vergleichen, bei denen spezielle Embdedded-Atom-Wechselwirkungen eingesetzt wurden (Abs.5.5.1). Ursache ist die qualitative Ähnlichkeit des Phasendiagramms von Eisen und dem Dzgutov-Potential. So findet man für die innenzentriert kubischen Ausgangsstrukturen ähnliche Endstrukturen. Auch solitäre Wellen, die im nächsten Abschnitt detailliert beschieben werden, sind beim Eisen beobachtet worden.
Zumsannefassend kann man sagen, dass sich das Dzugutov-Potenial nicht sehr gut für Stoßwellensimulationen von Quasikristallen eignet, da die Stabilität verglichen zu gering ist. Im Gegensatz zum binären Fall wurden hier aber eindeutig quasikristallspezifische Defekte, nämlich Zellflips, aufgefunden. In beiden Fällen zeigt sich, dass Auftreten der Defekte durch die Deformation der Probe verstärkt wird.

**Die $\omega$-Phase und solitäre Wellen**

Innenzentrierte kubische Kristalle besitzen einen inhärente Instabilität entlang der dreizähligen Achse, was durch das Verschwinden der Summe der $k$-Vektoren im reziproken Raum bei zwei Dritteln der Zonengrenze verursacht wird. Dies führt bei vielen Materialien zu einem Phasenübergang in die $\omega$-Phase.
In unserem Fall ist die $\omega$-Phase nur in einem kleinen Kompressionsbereich stabil (Abs.6.7.2), so dass eine Hin- und Rücktransformation zwi-

schen $\omega$-Phase und innenzentriert kubischer Phase stattfindet solange die Phasenumwandlung sich langsamer als die Schallgeschwindigkeit ausbreitet (Abs.6.4). Wird die Schallgeschwindigkeit überschritten, so entstehen solitäre Wellen, die im Innern die $\omega$-Phase enthalten. Erhöht man die Temperatur bei der Simulation, so verschwinden die solitären Wellen nach und nach.
Bei sehr großen Proben mit einem Querschnitt von 40x40 Atomabständen beobachtet man auch bei niedrigen Temperaturen ein Abklingen der solitären Wellen (Abs.6.4.4). Betrachtet man die Probe als eine Ansammlung von Atomketten parallel zur Stoßwellenrichtung, so findet man, dass die Amplitude der Stoßwellen entlang der Ketten nicht abnimmt, sondern die Korrelation zwischen benachbarten Ketten verloren geht. Bewegt man sich mit dem Maximum des Drucks in der solitären Welle mit so beobachtet man, dass diese Front zunächst flach ist, dann zu fluktuieren anfängt, und am Ende sich einige langwellige Moden aufschaukeln, die gerade in den Querschnitt der Simulationszelle passen.
Nach solitären Wellen wurde auch in anderen Symmetrierichtungen gesucht (Abs.6.4.5). Dabei wurde festgestellt, das es in Spiegelebenen und entlang der vierzähligen Richtungen keine solitären Wellen gibt. Im übrigen hängt das Auftreten stark von der Methode der Stoßwellenerzeugung ab. Um den Einfluss der unendlich starken Beschleunigung am Anfang der Simulation zu verringern, wurden Simulationen mit langsam ansteigenden Pistongeschwindigkeiten durchgeführt. Die solitären Wellen treten dennoch auf. Sie konnten auch bei Stoßwellensimulationen in Eisen mit realistischen Wechselwirkungen beobachtet werden und waren dort sogar stabiler als in den hier vorgestellten Simulationen.
Für die Beschreibung der $\omega$-Phase und der solitären Wellen existiert ein phänomenologisches Landau-Ginzburg-Modell (Abs.6.7), das alle beobachteten Phänomene voraussagt. Aus diesem Grund wurde die Anwendbarkeit des Modells untersucht (Abs.6.7.4). Leider wurde festgestellt, dass die Vorraussetzungen für die Landau-Ginzburg-Beschreibung nicht gegeben sind. Auch die Dispersionsrelation der Phononen (Abs.6.7.3) wurde bestimmt und ein Weichwerden der longitudinalen Mode gefunden. Allerdings liegt dies nicht bei zwei Dritteln der Zonengrenze sondern fast bei der Hälfte, solange sich die Probe in der innenzentrierten Phase befindet. Wird sie aber uniaxial komprimiert, so wandert die Instabilität zum erwarteten $k$-Wert.

Solitäre Wellen wurden auch in flächenzentriert kubischen Kristallen entlang der zweizähligen Achse beobachtet (Abs.6.8). Auffällig ist dabei, dass es sich ebenfalls um eine Richtung handelt, in der die Atome den kürzesten Abstand haben. Auch bei den zwölfzähligen Quasikristallen und Approximanten findet man Ansätze von solitären Wellen senkrecht zur Grundebene. Hier sind sie aber nicht stabil, da die Atomketten mit kurzem Atomabstand sozusagen ausgedünnt sind. Es stellt sich deshalb die Frage, ob solitäre Wellen auch in einfach kubischen Kristallen entlang der vierzähligen Achse existieren. Nun sind aber einfach kubische Kristalle instabil. Dieses Problem wurde gelöst, indem Wechselwirkungen nicht nur zwischen nächsten sondern auch zwischen zweitnächsten Nachbarn eingeführt wurden. Es konnten tatsächlich solitäre Wellen entlang der vier- und zweizähligen Richtung erzeugt werden je nach dem, ob die kürzeren oder längeren Wechselwirkungen stärker waren.
Zusammenfassend führen diese Beobachtungen zu einem einfachen Modell: solitäre Wellen in einer bestimmten Richtung treten auf, wenn die Atome ununterbrochene Ketten mit kürzesten Atomabständen bilden. Die solitäre Welle stellt einen Stoßpuls wie bei harten Kugeln dar, der die Atomkette entlang läuft und von eindimensionalen Ketten harter Kugeln wohlbekannt ist. Die atomaren Ketten müssen dicht gepackt sein, da sonst die Korrelation zwischen benachbarten Ketten verloren geht und die solitäre Welle verschwindet.
Die Frage einer analytischen Beschreibung der solitären Wellen wurde ebenfalls diskutiert. Der Zerfall der solitären Wellen zeigt, dass eine dreidimensionale Beschreibung notwendig ist. Da solche nichtlinearen Gleichungen aber nur numerisch lösbar sind, wurde dieser Weg bisher nicht weiter verfolgt.

**Amorphe Strukturen**

Bei den diatomaren und bei den monoatomaren Simulationen wurden auch das Verhalten von amorphen Ausgangsstrukturen mit denselben Wechselwirkungen und Zusammensetzungen wie bei den Quasikristallen und Kristallen untersucht (Abs.4.4.9 und 5.4.7). Die amorphen Phasen wurden durch Abkühlen einer Schmelze gewonnen.
Erwartet wurde, dass es hier keine elastische Hugoniotgrenze gibt, und dementsprechend keinen Bereich mit elastisch-plastischer Welle, sondern dass sich das Material verhält wie eine Flüssigkeit. Bei den binären Strukturen ist dies tatsächlich der Fall. Die Stoßwellengeschwindigkeit

ist im ganzen untersuchten Bereich eine lineare Funktion der Geschwindigkeit, mit der die Klötze bewegt werden.
Die Stoßwellengeschwindigkeiten bei der monoatomaren amorphen Phase weichen von der Linearität ab: bei Pistongeschwindigkeiten bis etwa 15% der Schallgeschwindigkeit hat man nichtstationäre dispersive Wellen, die sich etwa mit Schallgeschwindigkeit bewegen. Erst dann setzt das lineare Verhalten ein. Eine Ursache für den quasielastischen Bereuch ist nicht bekannt.

**Schlußbemerkungen und Ausblick**

In dieser Arbeit konnten erste Ergebnisse von Stoßwellensimulationen in komplexen geordneten Strukturen berichtet werden. Bei den Quasikristallen konnten tatsächlich neuartige Plastizitätsmoden beobachtet werden, die nun im Detail in Gleichgewichtssimulationen weiter untersucht werden sollten.
Bisher wurden Modellpotentiale verwendet. Inzwischen sind auch für Quasikristalle spezifische Wechselwirkungen berechnet worden. Zusammen mit verbesserten Modellen sind nun auch realistische Simulationen möglich.
Für manche Phänomene wie dem Ausheilen der Defekte und dem Erreichen stationären Stoßwellenzustände sind noch wesentlich größere Proben und längere Simulationszeiten notwendig. Hier sei auch noch auf die Entwicklung des Hugoniostaten hingewiesen, eines Ensembles zur Gleichgewichtssimulation des Zustands hinter der Stoßwellenfront.
Spekulativ ist auch immer noch die Beobachtung der solitären Wellen. In den Simulationen wurden sie unter verschiedenen Umständen beobachtet und ihre Existenz nach allen Seiten abgesichert. Jetzt wären experimentelle Untersuchungen sehr hilfreich.
Bisher wurden Stoßwellen nur in dreidimensionalen Quasikristallen studiert und der zweidimensionale Fall vernachlässigt, obwohl ein wohluntersuchtes binäres Modell existiert und die Analyse der Ergebnisse viel einfacher sein sollte. Diese Simulationen sollen nachgeholt werden.
Eine Zukunftsvision stellt die Simulation der Laserabtragung dar. Hier treten Stoßwellen, Risse und Versetzungen auf. Zur Simulation werden mehrere Millionen Atome benötigt. Eine besondere Rolle spielt das Elektronengas bei der Wärmeleitfähigkeit. Sein Einfluss muss mit finiten Elementen modelliert werden, was bedeutet, dass Multiskalensimulationen notwendig werden.

# Introduction

With the advent of large massively parallel supercomputers it has become possible to carry out multi-million atom molecular dynamics simulations. One of the most spectacular applications is the atomistic scale study of defects generated by shock waves in three dimensions. Before it was not possible to resolve the details of the defects [101], and the simulations were limited to four-fold symmetry directions of fcc crystals. Thus it occurred as a surprise when Germann et al. [72] found that even simulations of one of the simplest systems, fcc-crystals with Lennard-Jones interactions, yielded quite complicated phenomena if shocked along the two- and three-fold directions, for example martensitic phase transitions and non-steady wave fronts. The phenomena are still partially unexplained [206]. One of the surprises included different kinds of solitary wave trains along the three-fold direction. Meanwhile non-steady solitary waves have been observed in bcc-iron along the three-fold direction by Kadau [118] and by the present author in a simple cubic structure along the four-fold direction.

Atomistic simulations of shock waves have spread out in different directions: other crystal structures like diamond for example [56, 237] are studied, pre-existing defects [101, 26] are built in, and poly-crystals [116] are simulated. In the present thesis I added yet another direction: the extension to binary crystal structures and to even more complex aperiodic structures, namely the quasicrystals. The wealth of behavior observed indicates that I may have scratched up to now only the surface of possible phenomena.

The other central topic of this thesis is the study of solitary waves related to shock waves. Holian and Straub [102, 204, 97] have treated the subject in one dimension and have generalized it to three dimensions. Today two kinds of solitons have to be distinguished: one-dimensional locked-in solitons and non-steady solitary waves. My simulations for the first time have revealed solitary waves which require a three-dimensional treatment since they develop transverse modulations. For the case of solitary waves in bcc-crystal shocked along the three-fold direction I could show that they are the super-sonic continuation of a sub-sonic intermediate phase transition to a hexagonal $\omega$-phase.

The habilitation thesis is devoted to two research communities which

have nearly no overlap: the community which studies shock compression of solids, and the people working on quasicrystals. To make the thesis as comprehensible as possible for both groups I have included sections on the fundamentals of shock wave physics and on the foundations of quasicrystals. Each section may seem superfluous for the other group, but then I ask people to apologize and simply skip the section.

I will start in Part I with a repetition of the general basics of shock waves in condensed matter. The essential equations required to understand the behavior of shock waves are given and the difference between shocks in fluids and solids are specified. An overview of the literature on shock compression of solids follows. The next topic is the state of the art of large-scale shock wave simulations. I address the methods to generate shock waves in simulations and shortly characterize our general purpose molecular-dynamics code IMD suitable for massively-parallel simulations.

In a short overview the crystallographic characteristics of quasicrystals are exposed and the path to atomistic structures and new kinds of defects is drawn. The structure models investigated in the simulations are explained subsequently. A description of the special Dzugutov potential applied in the simulation and a discussion of its phase diagram follow. Part I ends with the presentation of experimental results related directly or indirectly to the model materials studied here.

The starting point of my research was to compare the behavior of periodic and aperiodic materials under the influence of shock waves. Due to the rather limited number of suitable models I had not many choices. The outcome of this attempt is the central part of this thesis exposed in Part II. It is subdivided into three chapters: a diatomic case, a monatomic case, and the solitary wave phenomena together with the $\omega$-phase.

If the most frequent icosahedral quasicrystals are to be studied one has to resort to binary models. It turned out that this is a huge task since up to now large scale shock wave studies do not exist even for ordinary crystals. The results on diatomic quasicrystals are given in the first chapter.

If arbitrary crystal symmetries are permitted a monatomic dodecagonal model endowed with the special Dzugutov potential [53] can be applied. The results are the content of the next chapter. The ground state of this model, however, is not a quasicrystal but an ordinary bcc-phase.

So I could extend my exploration to a number of crystalline and quasicrystalline phases stabilized by the Dzugutov potential.
The peculiar behavior of shock waves along the three-fold axis of the bcc crystals leads to the final chapter of Part III: non-steady solitary waves are observed. Since all attempts to eliminate these waves and all alterations of the initial conditions were fruitless I have come to the conclusion that these solitary waves are not an artefact but deserve a more closer look. Results obtained by other researchers confirm this opinion [118]. The solitary waves are closely related to a bcc-lattice anomaly and an intermediate phase transition. Analytical theories for the transformation [29,30,181,182] have been examined and it has been shown that generalizations are necessary.
The thesis ends with a consideration of the prospects of shock wave simulations: its extension to polyatomic materials for example and to technologically relevant applications like laser ablation.

# Part I

# Shock Wave Physics, Shock Wave Simulations, Structures and Interactions

Chapter 1

# Shock Wave Physics

## 1.1 Why study shock waves in solids?

The scientific study of shock waves is simply appropriate due to the fact that they are everywhere and occur in all states of matter [123]: from the bow shocks of the sun and the earth, from the explosion of supernovae down to the shock waves that ignite thermonuclear fusion, cause sonoluminescence or a sonic boom.

If we assume that shock waves exist in solids (which is well known from experiment, and meanwhile from simulations also) then there are a number of good reasons to study them in computer simulations:

- Shock waves permit to compute the equation of state under extremely high pressure and/or high temperature conditions, for example to look for the metalization of hydrogen.

- Shock waves allow to study the mechanical properties of solids under sudden load change.

- Shock waves can be used to excite plasticity modes without introducing defects artificially. This can be helpful in the case of complicated structures like quasicrystals.

  Strong enough shock waves will produce defect structures which can be analyzed post mortem. The generation of extended defects is also possible.

- Shock waves frequently lead to phase transitions. Thus they permit to study the dynamics of the transition.

We may in sort say with Jim Asay [8]: Shock waves are useful to study properties of materials which are inaccessible to other methods.

## 1.2 The definition of shock waves

The definition of shock waves depends to some degree on the point of view and on the application. Although it is possible to define shock waves in continuum models rigorously by their mathematical properties, namely as an infinitesimal jump, such a definition may not be suitable for physical applications due to the discrete nature of the atomic structure. This is true already for fluids where shock fronts always have a finite width, but even more for solids due to the rigid nature of the lattice.

Usually shock waves are defined by a moving discontinuity of a physical observable like pressure, stress, density or material velocity [37]. There is no problem with this definition in liquids or gases since any value of the jump of the physical observables at the discontinuity surface is allowed due to the lack of retention forces. Viscous flow can occur and steady or stationary waves are permitted. The shock waves can be described by the Navier-Stokes equations despite the large gradients which are present at the discontinuity interface [100, 104].

In solids there is a problem with this definition since they possess finite yield strength. If the shock stress is above, then the solid will behave like a fluid. But shock waves are possible already at lower shock intensities. Then two waves are observed, namely an elastic precursor wave and a plastic wave.

According to Boslough and Asay for example [25] (See also Bethe [19]) stable shock waves have to be super-sonic with respect to the unshocked material and sub-sonic with respect to the shocked state.

If we use the definition that a shock wave is a wave which causes permanent rearrangement of the atoms [94] (in contrast to strong elastic waves), then super-sonic elastic waves which cause transient deformations are excluded, since only plastic waves lead to permanent modifications. Another distinction is given by Wallace [217]: In a sound wave dissipation can be neglected, but not for a shock wave where dissipation is essential.

We will not be rigorous with our notation, but will call any type of wave front with an abrupt change of thermodynamic quantities a shock wave [123].

Dislocations and slip planes with stacking faults for example are generated by plastic flow and relax the uniaxial stress to hydrostatic compres-

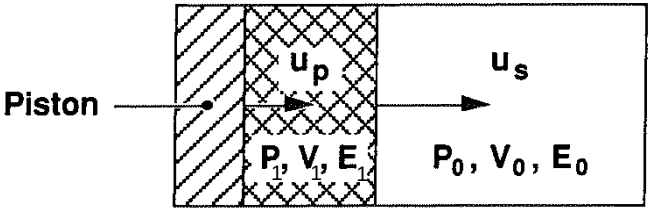


**Figure 1.1:** Definition of the basic variables. Unshocked state: $P_0$, $V_0$, $E_0$, $u_0 = 0$. Shocked state: $P_1$, $V_1$, $E_1$, $u_1 = u_p$. The interface between shocked and unshocked moves with the shock wave velocity $u_s$. The shocked material is driven by the piston and moves with velocity $u_p$.

sion. In contrast to the fluid the stress will not be relaxed completely but only down to the level of the yield strength of the material. True shock waves, which lead to steady profiles [101], have to be accompanied by dissipative, irreversible flow transverse to the shock direction. The flow is extended due to the dislocations and the stacking faults for example [93, 101, 94]. In fluids viscous flow is found in the shock front [100, 104]. Thus the flow is localized to a small region.

## 1.3 Definition of the basic observables

The terminology of shock wave physics originates from the generation of shock waves by a piston in a tube filled with gas. The same expressions are used even if we have a solid instead of a gas and a flyer plate or a laser instead of a piston. The thermodynamic state of the material is typically characterized by the pressure $P$, the volume $V$, the internal energy $E$, and a velocity $u$ (Fig. 1.1). The temperatures of the shocked and unshocked material do not show up directly in the equation of state (See Appendix A) and are therefore omitted in the figure and anywhere else. In the unshocked material the observables are indexed with "0". In the standard experiment the unshocked material is at rest: $u_0 = 0$, and therefore $u_0$ is often neglected. The shocked material is indexed with "1" and is driven with the piston velocity $u_1 = u_p$. Sometimes $u_p$ is called particle velocity since it is the velocity with which the shocked material moves.

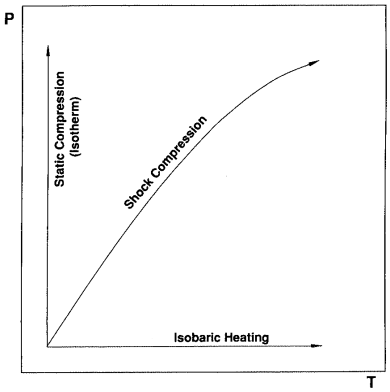


**Figure 1.2:** Change of state in three basic transformation processes: static isothermal compression, isobaric heating and shock compression.

There is an important difference between $u_p$ and $u_s$ which comes into play if there are several shock fronts or if the material is pre-shocked or shocked several times: $u_p$ is defined in a volume like the state observables $P$, $V$, $E$ whereas $u_s$ is defined for an interface. In the case of several shock fronts there is a $u_s$ for each interface and a $u_p$ for each volume in between.
In a solid, the pressure $P$ has to be replaced by the stress $P_{xx}$ if $x$ denotes the direction of the shock wave. In shock wave physics the stress $P_{xx}$ is frequently called $P_{xx}$ in analogy with the pressure $P$.

## 1.4 The equation of state

As noted in the introduction, shock compression offers new possibilities to evaluate the equation of state of a material. In the pressure-temperature plane shock compression lies between static compression and isobaric heating (Fig. 1.2).
Now lets consider a fluid or a material beyond its yield strength. If the equations of state for isothermal and adiabatic compression in the pressure-volume ($P$-$V$) diagram with shock compression (Fig. 1.3) are compared it is found that the growth of the pressure is the strongest

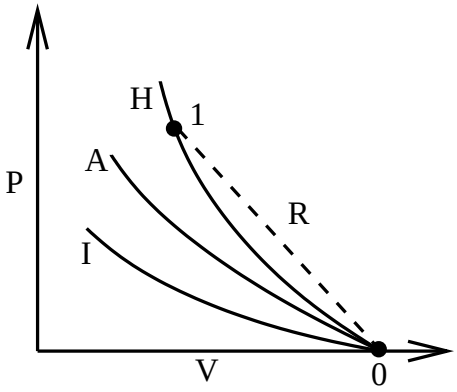


**Figure 1.3:** Pressure-volume equation of state of a fluid. The system moves along $I$ in an isothermal and along $A$ in an adiabatic process. The Hugoniot curve is denoted by $H$, and the straight Rayleigh line by $R$. In a shock experiment the system starts at 0 and *jumps* to 1.

in shock compression, provided the starting point is the same for all processes (here denoted 0).
There is a very important point to note: in an isothermal or adiabatic process the system moves along the lines in Fig. 1.3. In shock compression the system *jumps* from the initial state 0 to the final state (denoted 1). The Hugoniot curve $H$ is now defined as the collection of end-points of all experiments or simulations starting at the same point 0. Thus the Hugoniot curve is not an ordinary path of a thermodynamical process. If the system starts from ambient conditions, the Hugoniot curve is called "principal", otherwise "secondary" or "reshocked". In the isothermal or adiabatic processes the work is the area below the curve. In shock compression the work is the area below the Rayleigh line (Fig. 1.3).

## 1.5 The Rankine-Hugoniot equations

The Rankine-Hugoniot equations are the basic equations of shock wave physics, describing the change of the equation of state across a single shock front in a simple medium. The equations have been derived several times (originally in Ref. [150, 109, 110], reprinted in Ref. [151, 107,

108]). The Rankine-Hugoniot equations are truly valid in solids only if the stress is higher than the yield strength. Then the solids are in a state of hydrostatic thermal equilibrium, more precisely in a steady state.

The Rankine-Hugoniot equations are the consequence of the conservation of mass, momentum and energy across the shock front interface. If $\rho$ is the density, $P$ the hydrostatic pressure, and $E$ the internal energy[1] with index 0 on the one side and index 1 on the other side of the discontinuity then we may write down the following equations (Compare Sec. 1.3) with respect to the interface velocity $u_s$:

mass conservation:

$$\rho_0 u_s = \rho_1 (u_s - u_p), \tag{1.1}$$

momentum conservation:

$$P_0 + \rho_0 u_s^2 = P_1 + \rho_1 (u_s - u_p)^2, \tag{1.2}$$

energy conservation:

$$E_0 + P_0/\rho_0 + \frac{1}{2}u_s^2 = E_1 + P_1/\rho_1 + \frac{1}{2}(u_s - u_p)^2, \tag{1.3}$$

where we have already substituted $u_0$ by $u_s$ and $u_1$ by $u_s - u_p$. If the compressed state is not hydrostatic, then $P$ has to be replaced by the uniaxial stress $P_{xx}$. Frequently it is assumed that the state 0 is uncompressed and $P_0$ is set to zero in Eqs. 1.2 and 1.3.

From the conservation equations one can derive the Hugoniot equations:

$$\rho_0/\rho_1 = (u_s - u_p)/u_s \tag{1.4}$$

$$P_1 = \rho_0 u_s u_p + P_0 \tag{1.5}$$

$$E_1 - E_0 = \frac{1}{2}(P_1 + P_0)(V_0 - V_1). \tag{1.6}$$

If we carry out a simulation with given piston velocity $u_p$, initial pressure $P_0$, volume $V_0$, and energy $E_0$, and measure the shock wave velocity $u_s$

[1] More precisely, $E$ denotes the energy density per unit mass (See for example [48]), but to avoid confusion we will stay with the common sloppy labeling "internal energy".

then we can derive from the Hugoniot equations the quantities $P_1$, $V_1$, and $E_1$ which means that we are able to determine the equation of state. The equations may be solved for $u_s$, $u_p$ and $E_1 - E_0$:

$$\begin{aligned} u_s &= V_0[(P_1 - P_0)(V_0 - V_1)]^{1/2} && (1.7)\\ u_p &= [(V_0 - V_1)(P_1 - P_0)]^{1/2} && (1.8)\\ E_1 - E_0 &= P_1 u_p V_0/u_s - u_p^2/2. && (1.9) \end{aligned}$$

Now we can compute $u_p$, $u_s$ and subsequently $E_1 - E_0$ if we know the pressure-temperature equation of state. Apparently there are two equivalent representations: instead of the $P$-$V$-diagram we can draw a $u_s$-$u_p$-diagram (or a mixture of both). The $u_s$-$u_p$-diagram is often called Hugoniot diagram.
In the shock wave simulations it is sometimes advisable to work in a coordinate system where the unshocked medium 0 moves at velocity $u_i$. Then the Hugoniot equations read [25]:

$$\begin{aligned} \rho_0/\rho_1 &= 1 - (u_p - u_i)/(u_s - u_i) && (1.10)\\ P_1 - P_0 &= \rho_0(u_s - u_i)(u_p - u_i) && (1.11)\\ E_1 - E_0 &= \frac{1}{2}(P_1 + P_0)(V_0 - V_1) = \frac{1}{2}(u_1 - u_i)^2. && (1.12) \end{aligned}$$

The Rankine-Hugoniot relations may be found in many publications [156, 25, 1, 14]. Duvall and Graham [48] list generalized equations for an arbitrary sequence of multiple shock fronts, Henderson [83] compares different coordinate systems, and Davis [34] presents a long list representations of the Rankine-Hugoniot equations.

## 1.6 Two wave structure from material rigidity

In a solid, both the $P$-$V$- and the $u_s$-$u_p$-Hugoniot diagram look more complicated than in a fluid. Discontinuities exist which indicate that several shock fronts are present at a given time.
There are two major reasons for multiple shocks [76]: either the shock strength is beyond the dynamical yield strength of the solid (Sec. 1.8),

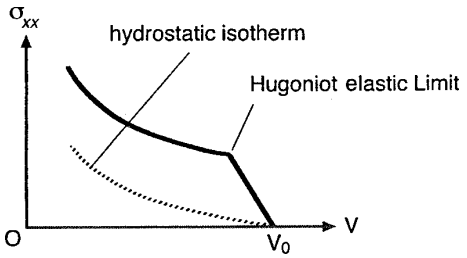


**Figure 1.4:** Hugoniot curve of an elastic-plastic solid. The full line is the reaction upon shock compression, the dotted line the path for hydrostatic compression. From [144].

then an elastic and a plastic wave is present, or there is a phase transition [48], then a plastic wave and a transformation wave are observed. In both cases the $u_s$-$u_p$-Hugoniot curves look rather similar. In the simulations the elastic-plastic behavior (Chap. 4) and an elastic-phase transformation behavior (Chap. 5) have been observed. A high-pressure solid-solid transformation has not been found in our model systems.
If a solid is compressed hydrostatically, its volume shrinks and the pressure rises (Fig. 1.4) [156]. The hydrostatic curve is smooth as a function of stress and volume. If the solid is compressed uniaxially stress and pressure will also increase until the maximal resolved shear stress of the material is reached. Then it will yield and change from the uniaxially compressed state to hydrostatic compression. In the $P$-$V$-diagram this event is visible through a cusp, called the Hugoniot elastic limit (HEL). The location of the cusp is estimated in Sec. 1.8.
Fig. 1.5 shows schematically the typical behavior of a solid with finite yield strength. The left part is the $P$-$V$-diagram, the right part contains typical stress profiles. The $P$-$V$-diagram can be divided into three parts with stresses $P_a$, $P_b$, and $P_c$. The borders of the regions are defined by the points denoted HEL and OD. The latter is the overdrive stress defined as the end-point of the line continuing the $P$-$V$-curve under the HEL straight on.

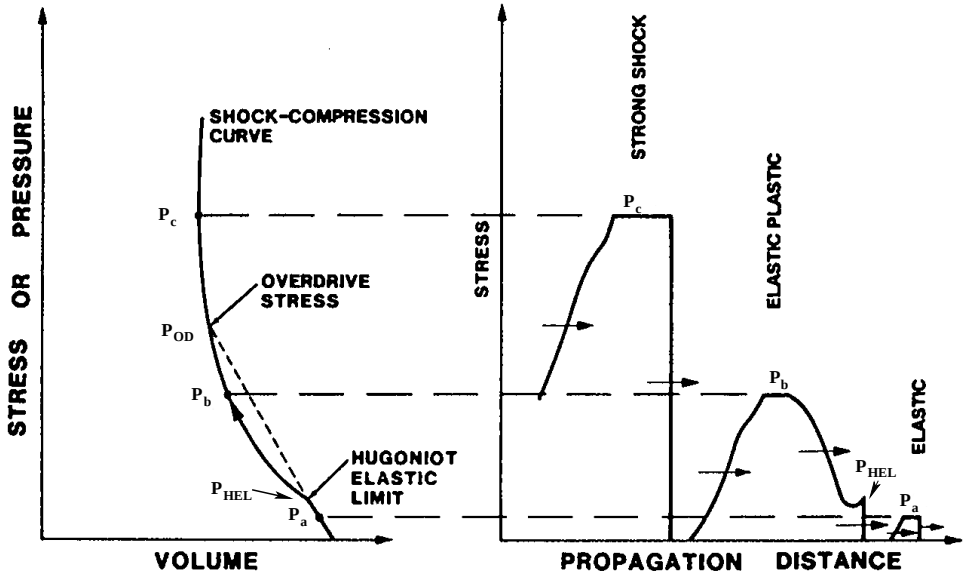


**Figure 1.5:** $P$-$V$-diagram (left) and corresponding wave profiles (right) of a solid with finite yield strength. The short dashed line in the left part is the direct continuation of the $P$-$V$-curve below the HEL. From [76].

Below the HEL the solid reacts elastically with peak stress $P_a$. We find a single jump of the wave pulse in the diagram on the right. Between HEL and OD a two-wave structure is observed. The stress builds up as long as the material has not yielded and an elastic precursor wave is generated with height is $P_{HEL}$. Subsequently the stress increases in the plastic precursor part until the final plastic wave follows with peak stress $P_b$. Ideally there would be two jumps in the stress profile: the elastic precursor and the plastic front. In reality the second jump is smeared out by the plastic precursor in between [216]. Beyond OD is the overdriven regime. There is still an elastic wave but it is invisible since the system jumps immediately to the plastically deformed state at stress $P_c$.

In experiment and in simulations the plateau stresses $P_a$, $P_b$, and $P_c$ can not last forever. They are released by a so-called rarefaction wave which cannot be a shock wave due to the stability criteria of shock waves [25, 19]. While the shock wave sharpens, the rarefaction wave spreads out in time.

If the wave profile is a time-independent function moving at fixed velocity, then the wave is called steady. This is true for shocks in the elastic and overdriven regime as long as the driving pressure has not been released. In the case of a two-wave profile (Part b in Fig. 1.5) the shock wave is steady only if the velocity of the elastic and the plastic wave are the same which is the exception. Thus the wave is non-steady in general, but the elastic and plastic part taken separately may be steady.

Fig. 1.6 finally represents the correspondence between the typical $u_s$-$u_p$- Hugoniot diagram and the $P$-$V$- or more generally $P_{xx}$-$V$-Hugoniot diagram of a solid. The information contained in both plots is the same since they are related by the Rankine-Hugoniot equations. Usually we will represent the $u_s$-$u_p$-Hugoniot since it is easier to obtain in the simulations.

## 1.7 Different representations of a stressed state

A typical shock compression experiment involves simultaneous loading of all points of a planar surface [75], and leads to a uniaxial deformed

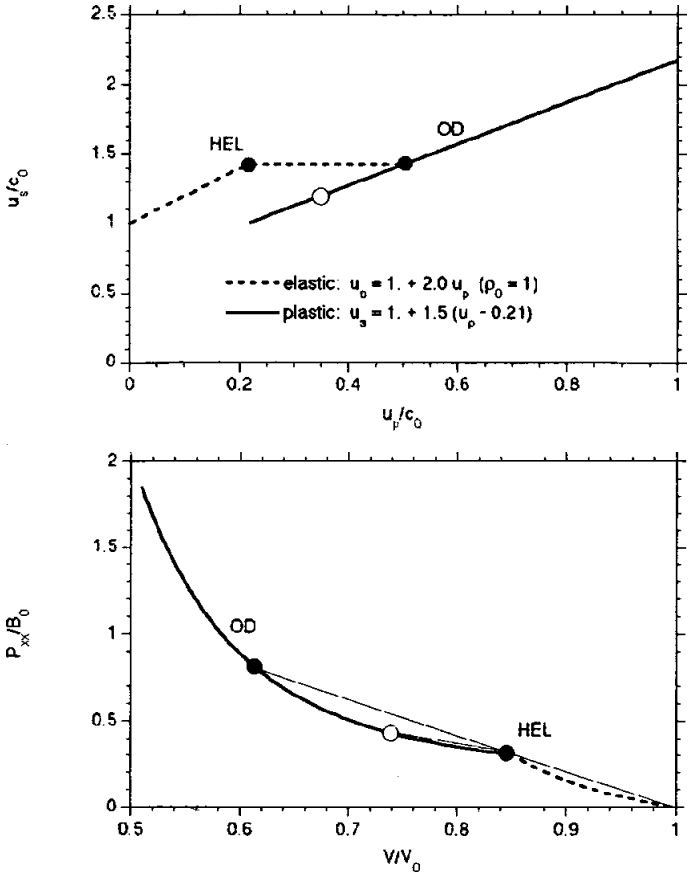


**Figure 1.6:** Schematic Hugoniot curves of an elastic-plastic solid showing the correspondence of the $u_s$-$u_p$ and $P_{xx}$-$V$ representations. HEL is the Hugoniot elastic limit, OD the beginning of the overdriven regime. Upper part: the $y$-axis intercept $c_0$ is the longitudinal velocity of sound, the virtual intercept of the full line is the bulk velocity of sound. Lower part: the long straight line is the Rayleigh line through the HEL. Below HEL is the elastic regime. The dots mark the borders of the elastic-plastic regime. Above OD is the overdriven or plastic regime usually studied in experiment. The open circle marks a typical elastic-plastic shock. From [95].

state. If a material can resist shear deformation then this uniaxially stressed configuration results in shear stresses, as the longitudinal and lateral stress components are not equal. The stress configuration can be decomposed into a mean or hydrostatic pressure $P$ and the shear stress $S$. Every plane in the body except those parallel or perpendicular to the shock normal is subjected to shear stress.
The hydrostatic pressure is given by

$$P = \frac{1}{3}(P_{xx} + P_{yy} + P_{zz}), \tag{1.13}$$

the $P_{ii}$ are the uniaxial stresses (in shock wave physics frequently called "uniaxial pressures"), $P_{ij} = 0$, if $i \neq j$. For isotropic and homogeneous materials $P_{yy} = P_{zz}$. Therefore

$$P = P_{xx} - \frac{2}{3}(P_{xx} - P_{yy}), \tag{1.14}$$

and the shear stress is maximized on planes lying at 45 degrees to the shock normal:

$$S = \frac{1}{2}(P_{xx} - P_{yy}). \tag{1.15}$$

The stress $S$ is called the maximal resolved shear stress. The uniaxial stresses can be expressed by:

$$P_{xx} = P + \frac{4}{3}S \tag{1.16}$$

$$P_{yy} = P_{zz} = P - \frac{2}{3}S. \tag{1.17}$$

## 1.8 Yield strength of a solid and the Hugoniot elastic limit (HEL)

For the elastic shock wave, stress and strain at the shock front are given by [144, 156]:

$$P_{xx} = (\lambda + 2\mu)\epsilon_{xx}, \tag{1.18}$$

$$P_{yy} = P_{zz} = \lambda\epsilon_{xx}, \tag{1.19}$$

where $\epsilon_{xx}$ denotes the one-dimensional strain component, and $\lambda$ and $\mu$ are the Lamé constants.
If yielding occurs behind the elastic precursor wave, the shock yield stress $Y$ can be given by

$$Y = 2\mu\epsilon_{xx}. \tag{1.20}$$

This result is obtained by assuming either a maximal shear stress or the von-Mises criterion for yielding due to the condition of one-dimensional strain.
The hydrostatic pressure at the wavefront is defined by

$$P = \left(\lambda + \frac{2}{3}\mu\right)\epsilon_{xx}. \tag{1.21}$$

The difference between the Hugoniot curve and the hydrostatic compression curve is given by (Fig. 1.4):

$$P_{xx} = P + \frac{4}{3}\mu\ \epsilon_{xx} = P + \frac{2}{3}Y = \left(\frac{2\mu}{3} + \lambda\right)\frac{Y}{2\mu} + \frac{2}{3}Y. \tag{1.22}$$

This is the value of the stress $P_{xx}$ at the Hugoniot elastic limit (HEL) and the factor $2\mu/3 + \lambda = K$ is the bulk compressibility modulus.
The yield strength includes a rate-dependent parameter and a pressure dependency as well. It is found that $Y$ is an increasing function of hydrostatic pressure. In general the propagation of elastic-plastic waves is a very complicated phenomenon strongly dependent on material which can be modeled only roughly by the simple considerations presented here.
An alternative description is given by the stress components:

$$P_{xx} = (K + \frac{4}{3}\mu)\epsilon_{xx}, \tag{1.23}$$

$$P_{yy} = P_{zz} = \left(\frac{\nu}{1-\nu}\right)\epsilon_{xx}. \tag{1.24}$$

$K$ is the bulk compressibility, $\nu$ the Poisson ratio. Then the maximal resolved shear stress can be written as

$$S = \frac{1}{2}(P_{xx} - P_{yy}) = \mu\epsilon_{xx} = \left(\frac{1-2\nu}{2(1-\nu)}\right)P_{xx}. \tag{1.25}$$

## 1.9 Velocity of sound

In the simulation of anisotropic monocrystals the question arises: Which is the correct velocity of sound useful to scale the shock velocity $u_s$ and the piston velocity $u_p$ such that the Hugoniot curves for shock waves in different directions can be compared directly? There exist two positive constants $c$ and $s$ in the expansion $u_s = c + su_p + \ldots$, as shock waves are always super-sonic and the limit for $u_p \to 0$ is the velocity of sound $c$. Because the velocity of sound is related to an elastic constant $E$ and the density $\rho$ through $c = \sqrt{E/\rho}$, the question amounts to the correct elastic constant.
According to Nagayama [144] the velocity $c$ is related to the hydrostatic or adiabatic bulk compressibility $K$ through $c^2 = K/\rho$. It is the velocity of a virtual longitudinal sound wave due to the hydrostatic compression. We call $c$ the bulk sound velocity or hydrodynamic sound speed [189] and denote it by $c_b$. It is related to the ordinary longitudinal velocity of sound $c_l$ and the transverse velocity of sound $c_t$ through

$$c_b^2 = \frac{K}{\rho} = \frac{K + \frac{4}{3}G}{\rho} - \frac{4}{3}\frac{G}{\rho} = c_l^2 - \frac{4}{3}c_t^2. \tag{1.26}$$

$G$ is the shear modulus. These are the usual statements about the scaling velocity $c$ found in many references (See for example [180]).
But our simulations show that $E$ should depend on the direction of the shock wave, which is not possible for $K$. The problem is resolved by the observation that most of the authors are experimentalists and deal with data on isotropic polycrystals in the *overdriven* regime.
A more careful approach (like the one by Davison [35]) leads us in the case of isotropic materials already for weak shock waves to

$$c := c_l = \sqrt{(\lambda + 2\mu)/\rho}, \tag{1.27}$$

and for strong shock waves to

$$c := c_b = \sqrt{(\lambda + 2/3\mu)/\rho}. \tag{1.28}$$

For anisotropic materials $c_l$ becomes equal to $\sqrt{F/\rho}$, where in the case of a principal axes coordinate system $F = c_{11}$, and $c_b$ gets equal to $\sqrt{(c_{11} + 2c_{12})/3}$, which is a trace and therefore independent of the coordinate system. The elastic constants $c_{11}$ and $c_{12}$ are the components of the elastic tensor in Voigt notation.

The simulation results show that this is indeed the correct answer: If scaled with the direction-dependent $c_l$, all curves have the same $y$-axis intercept in the Hugoniot plot. If unscaled they fall on one curve if $u_p$ gets large (See also Fig. 1.6).

## 1.10 Dependency of the shock wave behavior on the dimensionality of the simulation

The behavior of shock waves in one dimension is completely different from other dimensions [102,204,97]. The reason is the lack of transverse directions. Plasticity is avoided since the atoms cannot exchange their positions. Dissipation and thermalization are also not possible.

We want to stress this point here since it has been a matter of long disturbances between different research groups. Observations related to the dimensional dependency show up in our simulations and have to be discussed critically.

In one dimension non-steady waves of growing non-equilibrium material are observed. There is no plastic flow, only damped non-linear elastic waves. Thus non-steady profiles are not shocks [217] in the proper sense.

In the simulation of Lennard-Jones crystals it has been observed [101] that no plasticity is present below $u_p/c_0 = 0.25$ for shock waves along the four-fold axis where $u_p/c_0$ is the piston velocity scaled with the velocity of sound. At this speed the shock strength is approximately equal to theoretical strength of perfect crystals and it is the shock strength required to generate partial dislocations. If extended defects are present, the threshold is reduced down to about $u_p/c_0 = 0.1$.

The differences between one-dimensional processes and real shocks are summarized in Tab. 1.1. The last row indicates that "one-dimensional" does not necessarily mean one spatial dimension. Shock waves in two- or three-dimensional samples can behave like one-dimensional if the piston velocity is too small, or the temperature is too low, or no equilibration is carried out. Then the transverse coupling is missing.

**Table 1.1:** Comparison of one-dimensional processes and more-than-one-dimensional shock waves [100, 217].

| | 1d behavior | 2d/3d behavior |
|---|---|---|
| shock waves | non-steady elastic | steady plastic |
| shock front thickness | linear growth | finite |
| soliton-like | yes | destroyed by collisions |
| thermalized | no | yes |
| conditions for 3d-LJ-fcc | $T = 0$ $u_p/c_0 \leq 0.25$ | $T > 0$ !! $u_p/c_0 > 0.25$ |

## 1.11 General literature about shock waves

I am not aware of a basic textbook about shock compression in solids. But there are a number of notable books and series which contain the foundations of the shock compression physics of solids.
A complete account of shock waves is given in the "Handbook of Shock Waves" by Ben-Dor et al., especially the first volume [18] published in 2001. It contains a history of shock waves, starting in 1759 and ending in 1945 [123] which is regrettable since the shock wave physics of solids started more or less in 1945. The history of molecular dynamics simulations of solids began even later with the paper by Tsai and Beckett [211] in 1966 according to a review by Germann [69].
A few important dates may be noted: In 1860 Riemann published his theory of waves of finite amplitudes (Über die Fortpflanzung ebener Luftwellen von endlicher Schwingungsweite). Rankine [150] set up the basic equations of shock waves in 1870, which together with Hugoniot's contributions in 1887 and 1889 [109, 110] are known today as the Rankine-Hugoniot equations. In 1906 Duhem proved that true shock waves exist only in perfect fluids with discontinuous fronts according to Riemann's and Hugoniot's theory. Grüneisen [80] proposed his famous equation of state $pv + G(v) = \Gamma(v)e$ ($v$ specific volume, $e$ specific internal energy, $\Gamma(v) \neq f(T)$ Grüneisen coefficient, $G(v)$ related to lattice potential) based on his own work [79] and contributions by Mie [136] in

1926. In 1942 Bethe [19] calculated the stability of shock waves for an arbitrary equation of state.
The scientific exchange of shock wave physics has long been hampered by the Iron Curtain, due to the strategic relevance of shock wave studies for nuclear weapons. Therefore many researchers are still working in the national labs in the US, and the same may be true for Russia.
A complete account of shock waves from a Russian point of view published originally in 1966 also exists [228].
One of the best sources about shock wave physics in solids currently available is the series "High-Pressure Shock Compression of Solids" from Springer Verlag, edited first by R. A. Graham and now by L. Davison and Y. Horie. It is part of the more extended series "High-Pressure Shock Compression of Condensed Matter" which includes for example explosives and heterogenous materials. Also notable is the book by J. N. Johnson and R. Cherét collecting a number of "Classical Papers in Shock Compression Science" which are difficult to obtain.
The latest development on the physics of shock waves can be found in the biannual proceedings of the "Conference of the American Physical Society Topical Group on Shock Compression of Condensed Matter" published in the AIP Conference Proceedings.

### 1.11.1 Special literature for the present thesis

- A number of lists of reviews of shock compression of solids have been published by Graham and Davison [76, 77, 38] with a list of references from 1920 to 1979. A chronological bibliography until 1993 has been given by Asay and Shahinpoor [9].

- The general basics of shock waves may be found in [77, 76, 75, 83, 25, 34],

- and shock waves in solids have been addressed especially in [156, 143, 75, 144].

- Mechanical properties, plasticity, dislocations and fragmentation are treated in [28, 113, 78, 15].

- An account on ceramic materials is found in [132, 133, 13],

- The Hugoniot elastic limit (HEL), which determines the dynamical yield stress, (HEL) and the different wave forms observed in shock compression are discussed in [76, 75, 1].
- The equation of state (EOS) is the topic of [1, 192, 34].
- Hugoniot data from many experiments are shown in [156, 133, 14, 189, 209].
- Duvall and Graham [48] and Batsanov [13] treat phase transitions caused by shock waves.
- Reviews of simulations of shock waves in solids exist from Holian and co-workers [94, 101, 99, 98, 70, 95] and from Wallace [217], and from their opponents, MacDonald and Tsai [127]. Robertson et al. [158] have addressed energetic solids.
- Shock waves in granular materials are reviewed by Nesterenko [145].

Chapter 2

# Simulation of Shock Waves in Solids

## 2.1 Shock wave simulations: State of the art

To review the history of shock waves in general would lead much too far. The interested reader can find a general presentation for the time up to 1945 in [123]. A history of later times does not exist, so one depends on the reviews mentioned in Sec. 1.11. We will present only certain aspects related to the main topics of this thesis: the simulation of defect structures and phase transitions in inert materials and the discussions related to steadiness or stationarity of shock waves. Several reviews have been written by Holian [94,99,95] on simulations. Thus we will not deal with shock waves in liquids, gases, plasmas, and energetic materials, although the latter belong to the solids.

In the "prehistory" of shock wave simulations only continuum mechanics and finite element computations have been applied. Therefore no statements about the creation of defects or plasticity on an atomic scale were possible. It was not even clear whether the fluid case, represented by the Navier-Stokes equation, could be simulated on an atomic level [104, 93] since microscopic dynamics is time-reversible and dissipative processes are lacking.

The first molecular dynamics simulations of shock waves where carried out by Tsai and Beckett [211] in 1966. They studied one-dimensional[1] samples and found no plasticity due to that restriction. Later they extended their work to two- [210,212] and three-dimensional simulations [213,214], but without new insight. The next important step were three-dimensional simulations by Paskin and Dienes [147] in 1972. For the first time they obtained the linear Hugoniot relation $u_s = c_0 + s u_p$. The

[1] The term one-dimensional is used for the dynamical behavior of the system which indicates that the motion of the atoms was restricted to one dimension. The spatial dimension of the crystals was three.

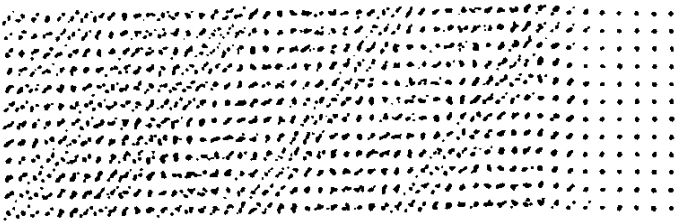

**Figure 2.1:** Simulation result from Holian [93]. The diagonal stripes are defect bands wrapped periodically around the simulation cell.

problem with these simulations was that the temperature was set to zero, therefore a one-dimensional behavior with non-steady waves was observed again. The claim now was that steady shock waves could not at all exist in solids.

The long-standing debate was finally resolved by Holian and Straub in a number of papers [102,103,204]. They could show that it is necessary to equilibrate the samples, and that a certain minimal piston velocity is required to induce plasticity and to generate steady shock waves.

The question on how dislocations are generated and how this leads to plasticity seemed to be solved when Holian [93] in 1988 carried out simulations of shock waves along the four-fold direction in an fcc crystal equipped with Lennard-Jones potentials. He found steady shock waves and a plasticity mode realized by stacking faults. The slipping of the material caused the relaxation of the uniaxial stress into a hydrodynamically compressed state. The problem with these simulations was the small size of the simulation cell which leads to a back-folding of the stacking faults and to a periodic array of defects (Fig. 2.1). Thus it still was not known what really happens for weak shock waves.

The next major step which confirmed the results from 1988 were the first multi-million atom simulations by Holian and Lomdahl [101] in 1998. Now the sample was large enough that the interaction of the stacking faults could be neglected. At stronger shock waves a whole network of independent partial dislocations and stacking faults was found (Fig. 2.2). Another important result was that the threshold of steady shock waves could be lowered considerably by extended defects.

This paper kicked off a wave of new shock wave simulation studies. The

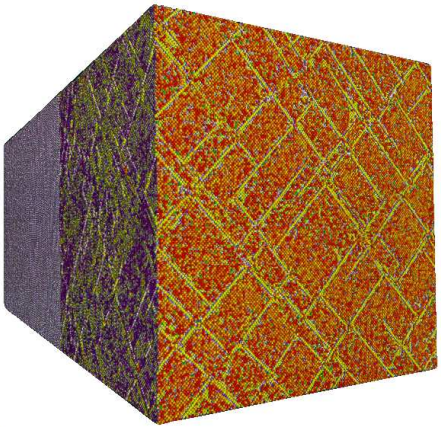

**Figure 2.2:** First multi-million atom simulation of shock waves by Holian and Lomdahl [101].

question of plasticity appeared to be solved now even for weak shock waves and the mechanisms probably rather simple. Thus the very complicated results found by Germann et al. [72] came as a surprise: They studied for the first time shock waves in fcc crystals along two- and three-fold directions and obtained non-steady shock waves, oscillatory behavior, solitary waves, martensitic transformations, and delayed plasticity, i.e. $u_{\text{plastic}} \neq u_{\text{elastic}}$ (Fig. 2.3). A number of detailed studies followed about the defect structures in fcc crystals, for example by Hirth et al. [89], Maillet et al. [129], Tanguy et al. [206], and Germann et al. [73]. The last two papers could for the first time demonstrate how dislocation loops are created and stacking faults are formed. Up to then there had been several models for plasticity, especially mechanisms for dislocation generation (See for example [198, 135, 219, 141], and more recently [134, 74]), some models even requiring super-sonic dislocations. These models had never been tested, but now they can be compared to simulations. Beyond shock waves, high-speed generation of dislocations in fcc materials has been studied by Schiøtz et al. [187, 188].
For completeness we mention a Russian group [7, 230, 231, 232, 233, 234, 235]. which also contributed important results to the study of fcc crystals with Lennard-Jones potentials, especially to the shock-melting pro-

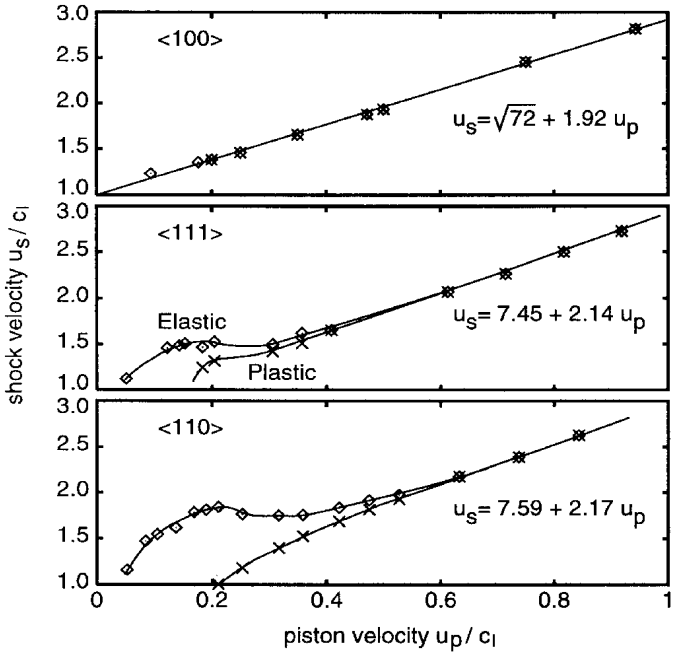


**Figure 2.3:** Hugoniot plot of fcc-crystals with Lennard-Jones interactions. From Germann et al. [72].

cess. Ravelo et al. [152] used the constant-stress Hugoniostat to determine the shock melting location in the phase diagram of the Lennard-Jones potential more precisely.

Further developments include the simulation of other structures, for example by Kadau et al. [115, 116, 117] who studied bcc with EAM-potentials for iron, Elert, and Zybin et al. [56, 237] who worked on diamond structures, and the results presented in this thesis. It is no longer possible to keep track of all new developments [26, 16, 17, 46]. The latest account of the present state has been given by Holian [96].

All these studies were concerned with monocrystalline samples where nanosecond time-scales are sufficient. Simulations of polycrystalline samples, which are much closer to application, have also been attempted. But they still represent a major challenge. The results obtained even

for the largest samples with up to 24 million atoms have not yielded a steady state [70, 95] since time-scales of microseconds are required.

### 2.1.1 The Hugoniostat

One important new development deserves to be mentioned here, although it has not been applied in the present thesis. The simulations of shock waves is a dynamical process, i.e. non-equilibrium molecular dynamics (NEMD) simulations are required. The time a simulation lasts is dictated by the size of the sample and the propagation time of the fastest shock front. Sometimes it would be desirable to simulate smaller samples but for longer times in order to observe for example relaxation processes of defects or phase transitions.
This suggestion can be realized with a new ensemble, the so-called Hugoniostat which has been developed by several people [200, 201, 128, 129]. Closely related to this development is another approach by Reed et al. [153, 154].
The idea of the Hugoniostat is to equilibrate the sample first and then to apply modified equations of motions in such a way that the system moves on a Hugoniot curve $E - E_0 = \frac{1}{2}(P + P_0)(V_0 - V)$. Thus one has an equilibrium (EMD) simulation and the simulation time and size of the sample are decoupled. The method can be combined with other constant observables, like volume or pressure and energy or temperature. Versions for Gaussian [200, 201] and Nosé-Hoover-type [128, 129] ensembles have been presented. The method of Reed et al. even permits to simulate several phases and metastable states.
Since the Hugoniostat methods are very new they still have to be tested thoroughly. Up to now the methods have been applied in a detailed study of the piston velocity dependency of the defect structures generated by a shock wave: A fcc crystal supplied with Lennard-Jones potentials has been shocked along the four-fold axis [128]. It is not clear whether the defect structures obtained in this way are the same as for dynamical simulations [95]. The best implementation of the Hugoniostat and a comparison of different versions can be found in [152].
With the Hugoniostat it will be possible to solve some of the problems caused by long-time relaxation especially in the diatomic simulations (Chap. 4) but maybe also to anneal the transformed crystals in the monatomic simulations (Chap. 5). The problem could be a modification

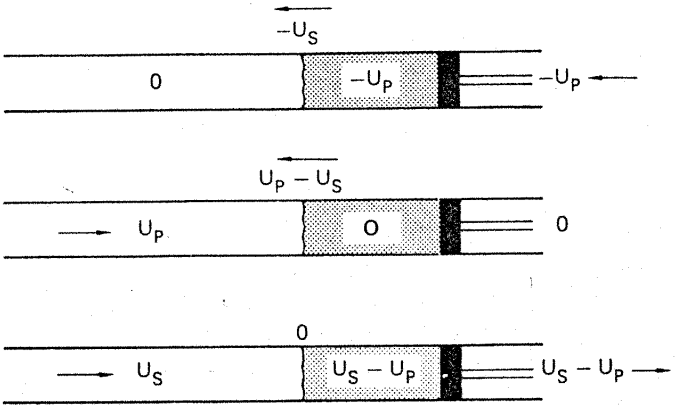


**Figure 2.4:** Different choices of the coordinate system (From [100]). The piston velocity is $u_p$, the velocity of the shock front $u_s$.

of the plasticity or transformation modes. No such difficulty is present for amorphous materials, and therefore they supply the best example to test the Hugoniostat.

## 2.2 Shock wave generation

Shock waves in computer simulations can be observed from different viewpoints. First of all there are different choices of the coordinate systems. In the first case the unshocked material is fixed (Fig. 2.4, top). In the second case the shocked material is at rest (Fig. 2.4, center) which permits to time-average the shocked material. In the third case the shock front is at rest which allows to average the properties of the shock front, but it requires the a priori knowledge of the shock front velocity. The averaging, however, is not possible if there are several wave fronts with different velocities.

### 2.2.1 Impact simulations

The simplest method to create shock waves is the impact method (Fig. 2.5). The setup is similar to the experiment where a flyer plate is

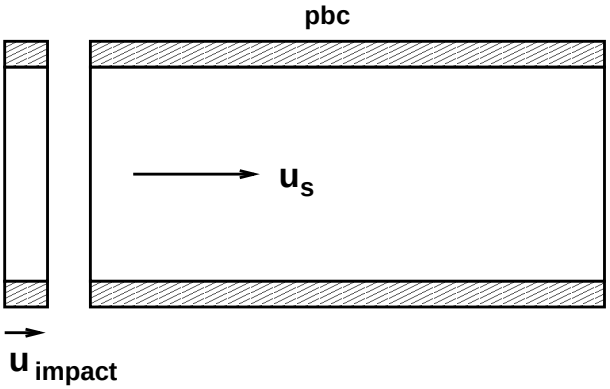


**Figure 2.5:** Impact simulations. "pbc" means periodic boundary conditions. The velocity of the flyer plate is $u_{\text{impact}}$, the speed of the shock wave $u_s$.

shot onto a sample. The flyer plate has a fixed kinetic energy, and is stopped after collision. Therefore it will always lead to a time-dependent behavior of weakening shock waves. Since the shock front propagates into the material, will lead to position dependent damage. The method works well for meteorite impact or laser pulses but is not suitable to study defects caused by stationary shock waves. Simulations of binary quasicrystals carried out with the symmetric impact method have been reported in Refs. [168, 166, 164, 167].
If the flyer plate is kept moving at constant speed, then the setup is equivalent to a piston compressing a sample at rest at speed $u_p = u_{\text{impact}}$, thereby creating a shock wave at speed $u_s$.

### 2.2.2 Symmetric impact simulations

Instead of shooting a thin plate onto a massive sample one can use two blocks of equal size. But there is still the problem of non-stationarity: If a fixed amount of kinetic energy is attributed to each moving block they will slow down as the energy is transformed into heat, and the piston velocity will change. Therefore it is better to keep the mobile block moving at constant speed after collision, or – in a symmetric way – to move both blocks at constant speed (Fig. 2.6). In the simulation the two parts are moved towards each other at constant velocities $\pm u_p$. Two

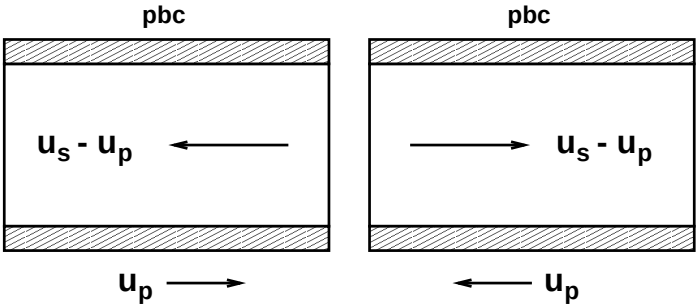


**Figure 2.6:** Symmetric impact simulation: colliding blocks. Notations are as in Fig. 2.5.

shock waves are created at the central plane where the blocks collide and propagate through the compound sample at velocities $\pm(u_s - u_p)$, where $u_s$ is the required shock velocity. The advantage of this method is that we can generate stationary states. A drawback is the moving shock front, therefore an averaging with respect to the shock front is not possible. Furthermore, we are always simulating two shock waves at a time which can be helpful sometimes since we can compare the results of both shock waves, and in the case of non-crystalline material they need not be identical.

### 2.2.3 Momentum mirror

The last disadvantage of the former method can be avoided if one of the blocks is replaced by a momentum mirror (Fig. 2.7). When the atoms reach the mirror, their velocity component parallel to the shock direction is inverted. Instead of keeping the mirror fixed it is possible also to move it at any desired speed, for example such that the shock front is stationary. One shortcoming of the mirror method is that it introduces a perfectly rigid boundary which may cause side effects. Such effects are clearly visible in the layering of the atoms near the mirror (See Chap. 5) and in the orientation dependency of the solitary waves (See Chap. 6). In general, and far from the mirror, it has been shown that the symmetric impact method and the momentum mirror yield equivalent results. The shock wave velocities, for example, and the

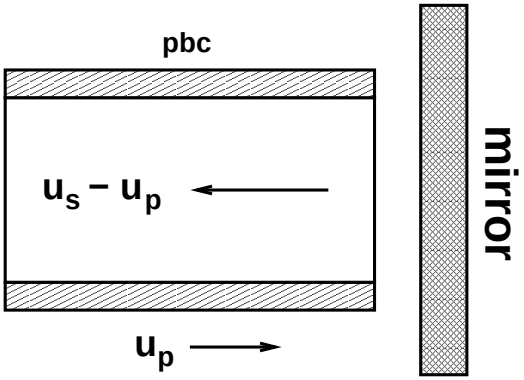


**Figure 2.7:** Momentum mirror. Notations are as in Fig. 2.5.

defect structures are identical.

### 2.2.4 Other methods

In our simulations we have employed the collision and the momentum mirror method. For completeness we will also mention other methods which have been applied frequently. In the methods presented up to now there is always at least one open boundary. This can be avoided in the shrinking-boundary-method, where the periodicity parallel to the shock front is reduced continuously during simulation such that the material in between is compressed uniaxially [95].

The last method is the so-called "ramjet" method [238] which works like a conveyer belt: at the one end of the simulation box new material is generated and equilibrated. It moves continuously into the central region, where it is shocked. At the other end of the simulation box the shocked material is discarded. Usually the coordinate system is set up such that the shock front is stationary. Then the velocities are given in Fig. 2.4, bottom. This method has first been applied by Klimenko and Dremin [226]. The advantage is that in the case of steady waves it is possible to average the observables over a long time, and one can get good statistics even for rather small systems.

## 2.3 Boundary conditions

Closely related to the shock wave generation methods are the boundary conditions. Since the shock compression leads to increasing pressure, one has to keep the borders of the simulation box fixed or to apply periodic boundary conditions. Free boundaries are not possible. In the unshocked part of the box open boundaries are also possible, but in the shocked part they would lead to non-steady waves as has been observed by chance when the simulation box was not chosen properly, or even to an exploding simulation box.
For ordered aperiodic materials it is not possible to apply periodic boundary conditions directly. In the case of quasicrystals the solution is well-known: there is an irrational quotient of the two sets of linearly independent reciprocal lattice vectors which is replaced by a rational number (Sec. 3.1). The quasicrystal is transformed into a rational approximant which is an ordinary crystal with a large unit cell. Thus it is possible again to identify the parallel boundaries of the unit cell and to apply ordinary boundary conditions.

## 2.4 Molecular dynamics simulations

All the simulations have been carried out with IMD, the **I**TAP **M**olecular **D**ynamics Simulation Package [202, 173]. IMD is a simulation program that supports a large number of serial and parallel computers. Parallelization is implemented geometrically by subdividing the simulation box into cells and distributing them on different computing nodes. The administration is carried out by the linked-cell-method. Therefore IMD is especially suitable for simulations with short-range interactions, like pair or EAM potentials, three-body potentials and covalent bonding. Long-range interactions are only supported in the serial version. Depending on the computer available, IMD can be run with MPI and/or OpenMP.
A number of thermodynamical ensembles, like NVE, different kinds of NVT, isotropic and anisotropic NPT are available. Special features include modules which support for example crack, shock or heat transport simulations.
Details about the implementation, parallelization, and further develop-

ment of IMD can be found in [202, 173, 81, 168, 20, 184, 67, 179]. The latest developments are published on
www.itap.physik.uni-stuttgart.de/~imd.
For the shock simulations a NVE ensemble was used. Equilibrations were performed with the NVT-Nose-Hoover and NPT-Andersen ensemble, depending on the volume or pressure to be fixed. At low temperature and low pressure the differences between NVT and NPT equilibration are marginal.
Beyond molecular dynamics it is also possible to use IMD to optimize the potential energy of a structure. For the quenching of the shocked samples IMD provides the microconvergence (mic) and the global convergence (gloc) method. In the first case an atom is moved if its velocity vector points in the direction of a minimum, otherwise its position is kept fixed and the velocity is set to zero. In the second case the global force in configuration space is used to figure out whether all atoms are moved or not. If a sample is close to equilibrium, the gloc method works much better than mic, especially if one tries to remove the kinetic energy. For the shocked structures, however, it was necessary to reduce the energy with the mic method first and then to minimize it with the gloc method.
The simulations presented in this thesis have been run on different computers lasting from single and double CPU PCs up to massively parallel supercomputers like the Cray T3E.

Chapter 3

# Structures and Potentials

## 3.1 Quasicrystals

This section is devoted to people who are not familiar with quasicrystals. Only the major differences between crystals and quasicrystals are presented. For a deeper introduction to quasicrystals the textbook by Janot [112] and the collection of reviews from the winter school in Alpe d'Huez [88] are recommended. The latest research can be found in the report by Trebin about the German "Schwerpunktprogramm Quasikristalle" [207] and the Proceedings of the 8th International Conference on Quasicrystals [149].

Quasicrystals have been discovered by Shechtman in 1982, but it took until 1984 that the first publication was accepted [190]. The first samples where only micrometer-sized, and so many people doubted the existence of equilibrium quasicrystals. Today, however, it is possible to grow centimeter-sized perfect single quasicrystals!

What is so special about quasicrystals? The starting point is their peculiar diffraction patterns (Fig. 3.1). It has sharp Bragg peaks which clearly indicates that quasicrystals possess long-range order. But the symmetry in the present example is decagonal and it is well-known that symmetries other than two-, three-, four-, and six-fold are forbidden in crystals since they are not compatible with periodicity. Thus quasicrystals cannot be periodic. Together with the incommensurate crystals they form the group of aperiodic structures. In ordinary crystals there is a set of symmetry related shortest distance vectors between the Bragg peaks and all other vectors are sums of it. In quasicrystals there are at least two such sets of vectors with an irrational quotient of their lengths. As a consequence there should be Bragg peaks everywhere in the diffraction diagram. The discrete diffraction pattern is caused by an envelope function which reduces the high-index spots to below visibility. But if the intensity of the diffraction beam is increased, more maxima will become visible.

Up to now quasicrystals have been found with icosahedral (i), decagonal

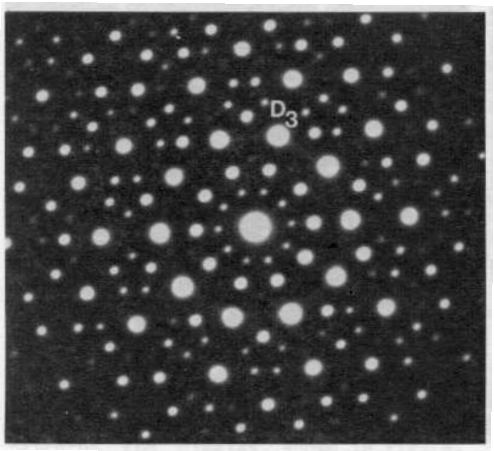


**Figure 3.1:** Diffraction patten of a decagonal quasicrystal. From Urban et al. [215].

(d), dodecagonal (t) and octagonal (o) symmetry. Many quasicrystals are aluminum alloys. Some alloys may occur with several symmetries. A few well-known examples are i,d-AlPdMn, i-AlCuFe, i-AlCuLi, d-AlCuCo, d-AlNiCo, d-AlNiFe, t-TaTe, o-VNiCr.
Icosahedral quasicrystals have morphologies of icosahedrally symmetrical polyhedra (Fig. 3.2) whereas decagonal quasicrystals occur in long decagonal needles.

### 3.1.1 Tiling models

How can we describe the internal structure of quasicrystals? An ordinary crystal possesses a single unit cell which is decorated with atoms. The crystal consists of one repeating unit cell. To build quasicrystals at least two different cells are required (Fig. 3.3). The cells or tiles must be placed face to face without gaps and overlaps. There are several methods to produce an infinite quasicrystal:

- the grid method, where the intersection points of symmetrically placed sets of regular grids are dualized to get the cells,

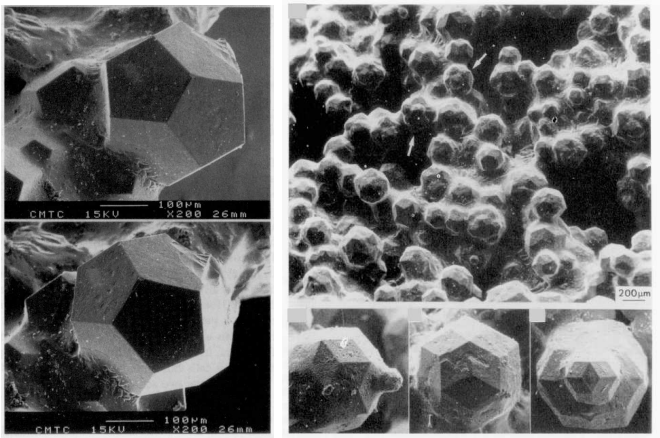


**Figure 3.2:** Quasicrystal morphologies. Left: AlCuFe dodecahedra, from Audier and Guyot [10], right: AlCuLi triacontahedra, from Dubost et al. [45].

- the inflation method, where for each tile a subdivision is defined into smaller copies of the same prototiles, and rules are defined to repeat the subdivision infinitely, and
- the projection method, where the tiling is produced through a cut of a higher-dimensional periodic crystal. Each lattice point is decorated with a polytope, and the intersection with the physical space produces the vertices. The tiles are the intersection of the cell boundaries of the higher-dimensional periodic lattice.

The dimension of the higher-dimensional crystal is given by the number of rationally independent indexing vectors of the diffraction pattern. In the case of icosahedral quasicrystals for example a six-dimensional space is required. A two-dimensional pentagonal tiling like the one in Fig. 3.3 can be produced from a five-dimensional hypercubic lattice[1]. For dodecagonal quasicrystals a five-dimensional space is needed, consisting of a four-dimensional space into which the two-dimensional aperiodic

[1] Actually, a four-dimensional lattice would be sufficient since all basis vectors sum up to zero, but then the lattice would not be hyper-cubic but the analog of the two-dimensional hexagonal lattice

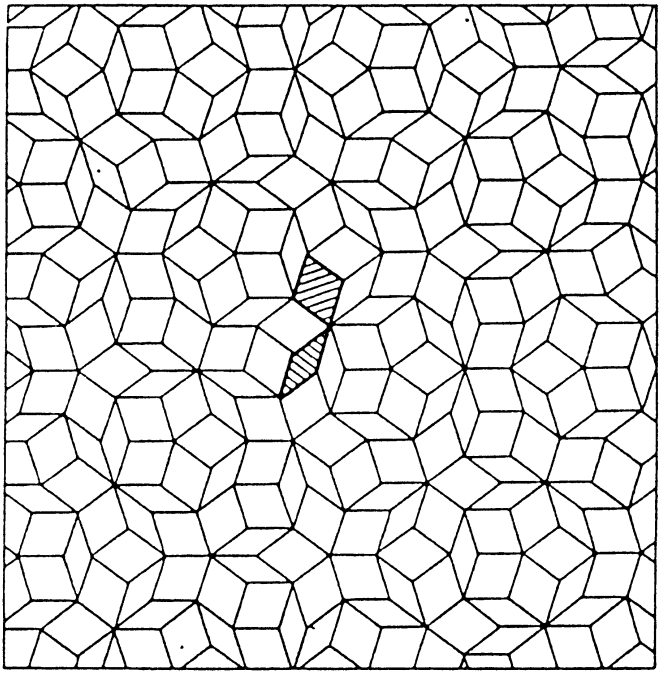

**Figure 3.3:** Pentagonal Penrose rhomb tiling. A fat and a skinny rhombus are marked.

plane is lifted plus a one-dimensional space along which the aperiodic planes are stacked.
The higher-dimensional embedding is very helpful since it permits to translate many concepts like dislocations or Burgers vectors from ordinary crystals directly to quasicrystals.

### 3.1.2 Defects in quasicrystals

If a crystal or quasicrystal is deformed plastically parts of the lattice are shifted with respect to one another, typically along a plane (See Fig. 3.4 for a two-dimensional example). If a crystal is sheared by a Burgers vec-

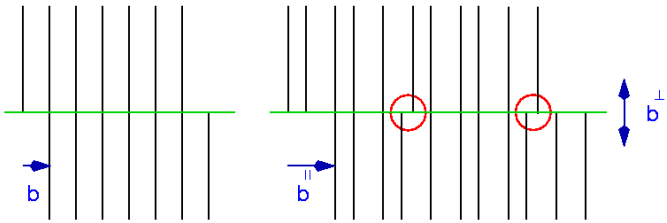


**Figure 3.4:** Shearing in a crystal and in a quasicrystal. Left: in a crystal the structure is unchanged if a part of the crystal is shifted by a Burgers vector. Right: in a quasicrystal it is not possible to bring all lattice plains into coincidence if a part is shifted by the real-space component $b^{\parallel}$ of a Burgers vector. A perp-space component $b^{\perp}$ will be left over.

tor, the resulting structure is equivalent to the original crystal. Therefore the material is not weakened. In quasicrystal Burgers vectors exist also, but they are lattice vectors of the higher-dimensional embedding space. The components in real and perpendicular space taken separately do not lead to proper lattice translations. Therefore only some lattice planes will coincide as shown in Fig. 3.4, but defects (red circles) will be left over. The defects cause a weakening of the quasicrystal and may change the properties from ductile to brittle behavior.

### 3.1.3 New defect types

In a quasicrystal new types of defects exist in addition to ordinary ones like vacancies, interstitials, dislocations and stacking faults, due to the aperiodicity of the structure. The most important are the following:

- Jags (red circles in Fig. 3.4): these are the sites where lattice lines or planes are broken by a shift of a part of the sample by a Burgers vector.

- Phason walls are formed by the jags. They are similar to stacking faults in ordinary crystals. Due to the aperiodicity a dislocation has to be connected to a phason wall much like a partial dislocation is connected to a stacking fault.

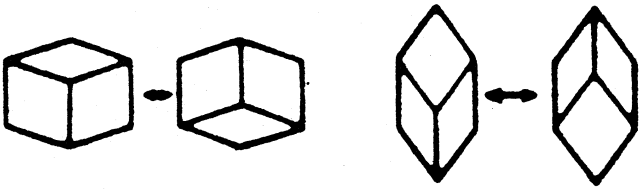

**Figure 3.5:** Simple flip in a tiling model where tiles exchange their places. In a real structure the tiles are decorated with atoms and the motion of the atoms characterizes the flip.

- Flips: The jags can move transversal to the phason wall such that the walls get broadened. Jumps of the atoms lead to the exchange of tiles. (Fig. 3.5). Flips are similar to diffusion processes in ordinary crystals.

- Phason clouds: if there are many defects and elevated temperatures then the phason walls are completely smeared out. Not only the shear planes but also the dislocations are accompanied by jags and flips leading to a polaron-like behavior.

## 3.2 Quasicrystal models

After the definition of the cells these must be decorated with atoms. Since we are dealing with three-dimensional simulations we will present two simple, but realistic three-dimensional models in detail. These are the models which will be used in the shock wave simulations in Chaps. 4 and 5.

Two-dimensional models are also available [124,221] which have successfully been applied in many computer simulations like the motion of dislocations [208,139], fracture in perfect quasicrystals [138,202,140,137], and fracture in random tilings [178,177].

### 3.2.1 Tetrahedrally close-packed phases

Quasicrystals are subdivided into two major classes [85]: the AlMn-class, which is rather loosely packed and typically contains tetrahedral and octahedral atom arrangements, and the Frank-Kasper-type quasicrystals where all atoms are arranged in non-regular, topological tetrahedra.

The Delaunay decomposition is a cell division of an arbitrary set of points which is obtained if the well-known Voronoi decomposition (equivalent to the Wigner-Seitz cell construction in reciprocal space) is dualized. The edges of the Delaunay cells are the vectors which are perpendicular to the faces of the Voronoi cells [162]. Structures consisting of tetrahedral Delaunay cells are called tetrahedrally close-packed (tcp) phases. The Frank-Kasper-type quasicrystals belong to this class, along with bcc since the dual of the truncated octahedra Voronoi cells are indeed distorted tetrahedra.

The last example leads us to tcp-phases in a narrower sense, namely the Frank-Kasper phases [191]. For these it is not only required that the cells are tetrahedra, but that along a common edge only five or six tetrahedra meet. Edges with six tetrahedra are called disclinations, edges with four tetrahedra anti-disclinations. Bcc crystals have no regular edges. The edges in the four-fold direction are anti-disclinations and the edges in three-fold direction disclinations. Therefore, bcc does not belong to the Frank-Kasper phases. The first neighbor shells of the Frank-Kasper phases form four polyhedra: an icosahedron, or 14-, 15-, or 16-vertex polyhedra, all with triangular faces only. It is easy to show that these are the only convex polyhedra with this property.

A subgroup of the Frank-Kasper phases are the Laves phases which consist of icosahedra, 14- and 16-vertex cells only, and can be generalized to the binary quasicrystals treated in the next section. Laves phases can have cubic (C15) and hexagonal (C14, C36)[2] symmetry, equivalent to the fcc-, hcp- and dhcp-structures. Other members of the Frank-Kasper phases are the square-triangle-phases which consist of icosahedra, 14- and 15-vertex cells, and may be generalized to the monatomic quasicrystals treated in Sec. 3.2.4. A few important members will also be

[2] C14, C15, and C36 are the names of the Laves phases in the Structure Reports / Strukturbericht See for example http://cst-www.nrl.navy.mil/lattice/struk/index.html.

described in this section.

### 3.2.2 The cubic Laves phase and diatomic icosahedral models

The first step of the construction of the quasicrystal structure is the cubic Laves phase. It is a periodic arrangement of prolate rhombohedra (Fig. 3.6, right). The rhombohedra are decorated with small atoms at the corners and the mid-edge centers and with two large atoms along the body diagonal dividing it in the ratio 3:2:3. Vertex and edge atoms possess an icosahedral neighbor shell and the large atoms are 16-fold coordinated. The large atoms of the Laves phase generate a diamond structure, the small atoms form a corner-connected network of regular tetrahedra. The edges of the rhombohedra are two-fold [110]-axes, the long body diagonal is a three-fold [111]-axis. The short body diagonals form the [100]-direction which are no true four-fold axes since the crystal symmetry is Fd3m.
The next step is the TI-model[3]. It is a quasiperiodic arrangement of the prolate and oblate rhombohedra (Fig. 3.6) on the standard three-dimensional icosahedral tiling [122]. To obey the different symmetry the prolate rhombohedra are slightly distorted with respect to the ones in the Laves crystal. They are decorated as before, but the large atoms now subdivide the body diagonal in the ratio $\tau$:1:$\tau$, with $\tau$ the golden mean $(1+\sqrt{5})/2$. The oblate rhombohedron contains only small atoms at the corners and mid-edge centers [174].
In the quasicrystal models the edges point along five-fold axes, the face diagonals of the cells are two-fold axes, and the long body diagonal is a three-fold axis. Strictly speaking, the TI-model is not a perfect Frank-Kasper phase since there are a few anti-disclinations in the center of the oblate rhombohedra [87, 162].
The third step is the BI-model[4]. It has been created since the TI-model has two drawbacks: the oblate rhombohedra form under-dense

[3] TI stands for truncated icosahedra, also known as Bergman clusters, a prominent structural feature of the model. A Bergman cluster is a polyhedron which looks like a soccer ball. The polyhedron contains successive shells of an atom, an icosahedron, a dodecahedron, a second icosahedron and a soccer-ball polyhedron. Bergman clusters occur at the places where 20 prolate rhombohedra meet at a common vertex.

[4] BI denotes binary icosahedral (model), also known as Henley-Elser model. Bergman clusters are found at nearly all the tips of the prolate rhombohedra and

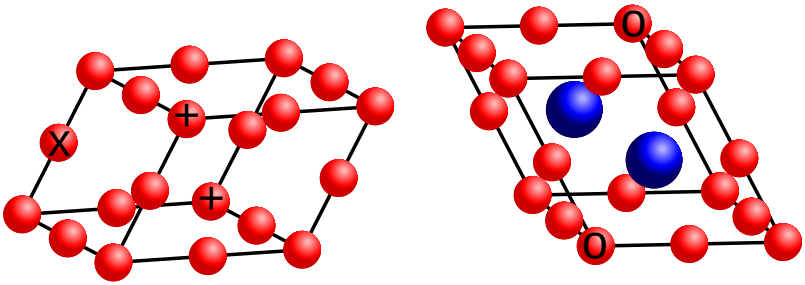


**Figure 3.6:** Oblate and prolate rhombohedron. Left: the x marks the atom around which 10 oblate rhombohedra fit together. The atoms marked with the + form a puckered decagon, around which the ring processes occur. Right: the atoms marked with o denote the intersection points of the [100]-direction.

and therefore unstable regions (due to the anti-disclinations), the stoichiometry is wrong if real quasicrystals are to be described, and crystalline approximants have different structural properties. Henley and Elser [87] modified the TI-model by replacing compounds of two oblate and two prolate rhombohedra wherever possible by a rhombic dodecahedron (Fig.3.7). The outer hull of the compound and the dodecahedron are identical, but in the interior four large and five small atoms are usually replaced by eight large atoms which are placed at the corners of a hexagonal bipyramid. Depending on the quasicrystal modeled ((AlCu)Li or (AlZn)Mg) the apex atoms (green in Fig. 3.7) are large or small atoms. In the case considered in this thesis they are large atoms. The BI model is still not a prefect Frank-Kasper phase since there are a few single oblate rhombohedra left. The oblate rhombohedra can never be eliminated completely, but their number may be minimized as in the canonical cell model [86].
We have produced a fourth model which does not belong to the Frank-Kasper structure class but should be mentioned here since it was formed from a Laves crystal in the process of melting, equilibrating, quenching,

the rhombic dodecahedra (Figs. 3.6 and 3.7). They form a network with connections along two- and three-fold symmetry axes.

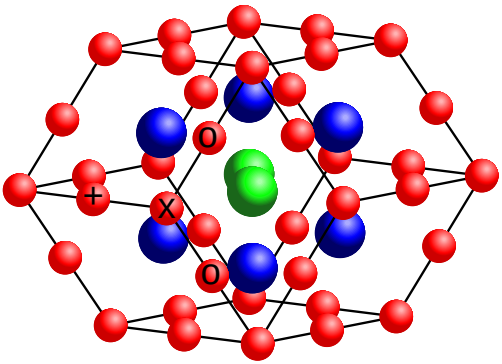


**Figure 3.7:** The rhombic dodecahedron. The atom marked with an x and its symmetry-equivalent copies are the primary sites of flips. The large green atoms are also very mobile. The atoms marked with + and o are secondary sites for diffusion.

and decompression to ambient pressure. It will be used for the simulations of a diatomic amorphous phase and is simply referred to as the diatomic amorphous model. The four structures have a rather similar composition: The crystal and the amorphous solid carry the structure formula $A_2B$, the composition of the TI quasicrystal is $A_{0.764}B_{0.236}$, and the composition of the BI quasicrystal is $A_{0.629}B_{0.371}$.

The Henley-Elser model has been derived from the crystal structure of $(AlZn)_{49}Mg_{32}$, and works rather well for this type of quasicrystals. An even better model would require a modification of the decoration. Equivalent sites are no longer decorated by the same atoms but that there is a certain probability for an occupation with different types of atoms. A slight shearing of the rhombohedra parallel to the five-fold axes and a reorganization of the cells as rhombic prisms leads to a class of decagonal models [169] which indicates the close relationship between the icosahedral and the decagonal symmetry.

**Local atomic rearrangements**

Atom jumps occur in the TI model in equilibrium simulations already [173]. They also play a major role in the shock wave simulations. Starting point are the oblate rhombohedra. If ten copies of these cells are put together at the edge marked with an x in Fig. 3.6, then the atoms marked with the + form a puckered decagon centered around an edge. The analysis of the local potential shows that the atoms can move almost freely around the decagon. This motion will be called a ring process. It is possible to replace pairs of oblate rhombohedra by one prolate rhombohedron. The rings are broken into parts and we speak of chains. The free motion of the atoms along a chain is strongly reduced but it is not completely impossible. If the TI structure is transformed into the BI structure, all rings and most of the chains are replaced by dodecahedra and the ring processes are suppressed entirely. There are, however, a few single oblate rhombohedra, and the atoms marked with the x in Fig. 3.6 can still exchange their places. Consequently flip processes still exist in the BI-model. Other jumps can occur around the dodecahedra. The atoms marked with the x in Fig. 3.7 are the remainder of the oblate rhombohedra, furthermore, the atoms marked green have a lot of free space around them. Thus exchange processes of the green atoms and the atoms marked with the x occur. A few jumps to the atoms marked with o and + have also been observed.

### 3.2.3 Other applications

The TI-model and the BI-model have been used in various computer experiments on quasicrystals, for example cooling simulations to generate quasicrystals [175], diffusion studies [165, 92], simulations of the generation and mobility of dislocations [40, 186, 184], and fracture simulations [179, 159, 160].

### 3.2.4 Square-triangle-phases and monatomic dodecagonal models

The $\sigma$-phase is an ordinary Frank-Kasper phase with squares and triangles as basic motives. Together with other related phases and the dodecagonal quasicrystals they have been described in detail by Roth [170].

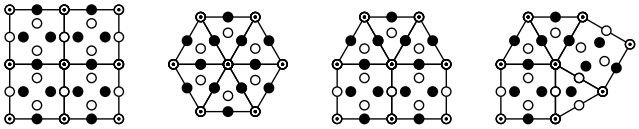

**Figure 3.8:** Possible vertex configurations in square-triangle tcp-phases. From left to right: A-phase, Z-phase, H-phase, and $\sigma$-phase.

The unit cell of the $\sigma$-phase can be subdivided into cells which look like equilateral triangles and squares if projected onto the basis plane perpendicular to the four-fold direction (Fig. 3.8). Two squares and three triangles meet at each vertex in such a way that the squares have no common edge. The arrangement of the atoms can be read off from Fig. 3.8: the vertices of the squares and triangles are decorated with atoms at $z = 0$ and $z = 1/2$ (dotted circles). These are the basic $A$ layers. The edge centers of the squares are alternatively decorated at $z = 1/4$ and $z = 3/4$ (filled and empty circles). The interior of the squares contains four additional atoms. Atoms nearest to each other in projection are placed in different layers. The atoms at the edge centers of the triangles are all either at $z = 1/4$ or at $z = 3/4$, the interior atom is again in the layer not occupied by the edge atoms. The atoms at $z = 1/4$ and $z = 3/4$ form the $B$- and $\bar{B}$-layers, respectively, which are locally equivalent up to translations and rotations. The atoms at the vertices of the tiles are 14-fold coordinated, while the atom in the center of the triangles is 15-fold coordinated. The remaining atoms on the edges and in the interior of the square are 12-fold coordinated non-regular icosahedra. Since all coordination shells have a triangular surface, all atoms are tetrahedrally close packed.

Other combinations of squares and triangles are also possible. There are three additional phases in which all vertices are of the same type (Fig. 3.8) [172]. These phases are less stable than the $\sigma$-phase, so they will not be considered further. If more than one vertex type is allowed the number of possible phases grows very rapidly, even for crystalline structures [39].

The quasicrystal is built of the same square and triangle tiles. In this

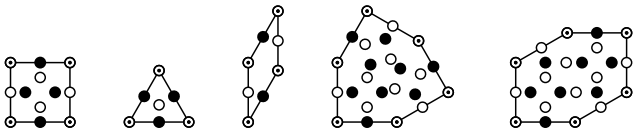

**Figure 3.9:** Original and additional tiles observed in the square-triangle tcp-phases.

thesis random tilings have been studied only although it is possible to construct perfect quasicrystals with the help of matching rules or by inflation [203]. In the quasicrystal model the tiles of the primary layer are arranged in such a way that the structure has dodecagonal symmetry on average. The $B$- and $\bar{B}$-layers have hexagonal symmetry only. They are mapped onto one another by the twelve-fold symmetry.

### Generalization

It is possible to introduce additional tiles, for example the hexagons (Fig. 3.9), and to construct more general quasicrystalline structures, but they will not be considered here in detail since these configurations are not as stable as the $\sigma$-phase and the pure square-triangle tilings. A more elaborate treatment may be found in [172]. Additional tiles are observed in crystalline samples already (Fig. 3.9). Especially rhombi may occur as localized defects or represent grain boundaries. The rhombi are not stable if they form pairs or larger aggregates. The two hexagons have not been observed in crystals. They may be viewed as transition states which can split into the other tiles.

Figure 3.10 represents a special approximant of a quasicrystal which has been chosen as a representative picture since most of the tiles and vertex configurations are present.

True Frank-Kasper phases contain squares and triangles only, since the rhombi and the hexagons do not formed the 12-, 14-, 15-, and 16-fold coordinated polyhedra only.

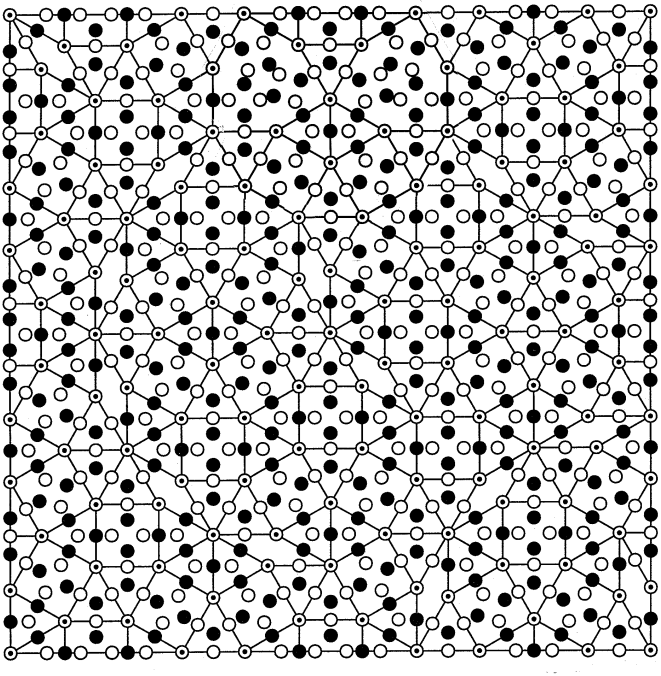

**Figure 3.10:** Part of a dodecagonal quasicrystal. The atoms in the basic $A$ layers $z = 0$ and $z = 1/2$ are dotted. The black atoms are in the $B$ layer at $z = 1/4$, the white atoms are in the $\bar{B}$ layer at $z = 3/4$. The edge length is usually of the order of $2a$, where $a$ is the nearest neighbor distance, but depends on the interaction between the atoms.

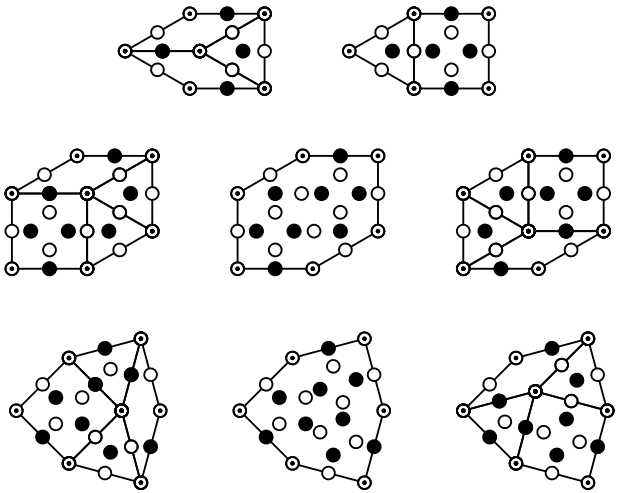

**Figure 3.11:** The most important flips in the generalized square-triangle tilings. Top line: two rhombi + triangle ↔ triangle + square. Central line: flip of a square, a rhombi and two triangles. Bottom line: rotational flip inside a hexagon. Other flips can be found in [172].

### Local rearrangements

Local rearrangements of tiles in generalized square-triangle quasicrystals in equilibrium have been studied by Roth and Gähler [172]. The number of flips is increased by the shock wave similar to the case of the diatomic quasicrystals.

In one type of flips a triangle and a square transform into two rhombi and a triangle (Fig. 3.11). In another instance a rhombus, two triangles and a square form a three-fold symmetric hexagon. Even the situation where a symmetric hexagon is transformed into a starlike interior and three rhombi has been seen in the shock wave simulations. In equilibrium this arrangement has not been stable. Other configurations are observed which necessitate more complex tiles but they will not be discussed in detail.

## 3.3 Shock wave experiments on quasicrystals and Laves crystals

No shock wave experiments of quasicrystals have been reported up to now. The only publications we are aware of are high-pressure studies of icosahedral AlMn (first quasicrystal class), where no transitions have been observed, and pressure induced amorphization and subsequent crystallization of AlCuLi (Frank-Kasper-type quasicrystal) [3, 4, 142]. There are also a number of more recent high-pressure studies which demonstrate the high strength of quasicrystals [120]. But the high-pressure studies do not lead to the high temperatures typical for shock waves.

Decagonal T-phase[5] quasicrystals and approximants have been generated by quenching under high pressure. The materials investigated include AlCoMn [157], AlMnYb [220], and AlCoNiTb [205].

## 3.4 The Dzugutov potential

Dzugutov has invented his potential [53,49] to study the glass transition of monatomic liquids. It turned out that this potential has a number of interesting properties, especially that it stabilizes monatomic dodecagonal quasicrystals.

Although Dzugutov [50] has obtained a quasicrystal by cooling a melt, the quasicrystal is not a ground state for this interaction at zero temperature. Another crystal structure, namely the $\sigma$-phase, which may be regarded as a low-order quasicrystal approximant, is more stable than the quasicrystal. But it has been shown that the ground state at zero temperature is a bcc crystal, and the stable structures at low temperature and high pressure are even close-packed fcc- or hcp-phases! Upon heating at low pressure bcc, the $\sigma$-phase and the quasicrystal phases are stable up to rather similar melting temperatures. This is the reason why shock-wave simulations have been carried out with these structure models and the Dzugutov potential.

[5] Like the dodecagonal models treated in this thesis they are quasiperiodic in a plane and periodic in the third direction.

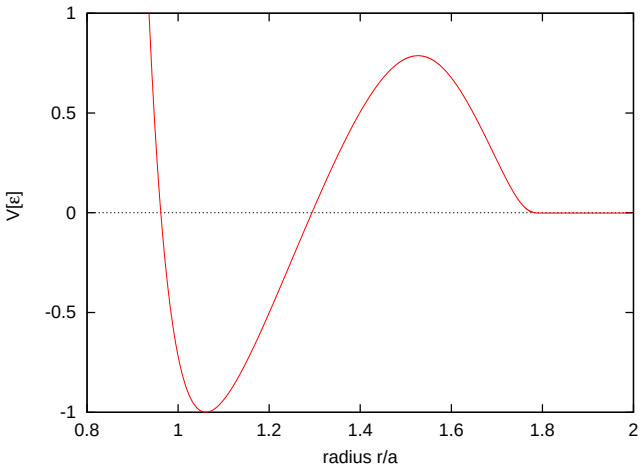


**Figure 3.12:** The Dzugutov potential as applied in the shock wave simulations.

### 3.4.1 Description of the potential

The Dzugutov pair potential [49], plotted in Fig. 3.12, was originally defined by

$$\Phi(r) = \Phi_1(r) + \Phi_2(r), \tag{3.1}$$

where

$$\Phi_1(r) = \begin{cases} A(r^{-m} - B)\exp\left(\frac{c}{r-a}\right), & r < a \\ 0, & r \geq a, \end{cases} \tag{3.2}$$

and

$$\Phi_2(r) = \begin{cases} B\exp\left(\frac{d}{r-b}\right), & r < b \\ 0, & r \geq b, \end{cases} \tag{3.3}$$

with the parameters:

| m | A | c | a | B | d | b |
|---|---|---|---|---|---|---|
| 16 | 5.82 | 1.1 | 1.87 | 1.28 | 0.27 | 1.94 |

The potential is characterized by a minimum at $r = 1.13a$ of depth $-0.581\epsilon$, having the same form as that of the Lennard-Jones potential, followed by a maximum at $r = 1.63a$ of height $0.460\epsilon$, designed

to prevent the system from crystallizing into simple crystal structures. Beyond the maximum the potential tends to zero continuously and is cut off at a range of $r_c = 1.94a$ which ensures that CPU times remain within reasonable limits.
In the present study we use a rescaled version of the potential with the minimum at $r = 1.061a$ and depth $-1\epsilon$. The minimum is followed by a maximum at $r = 1.5282a$ and $V = 0.7906\epsilon$. The cutoff radius now lies at $r_c = 1.805a$.
A potential similar in shape and with a related idea in mind has been devised by Silberstein and Clapp [194] to describe the behavior of martensites. Both potentials are nearly identical up to the point of inflection, the only difference is that the maximum in Silberstein and Clapp's potential is considerably larger than in Dzugutov's version. The maximum lies at $r = 1.619$ at height $1\epsilon$, and the cutoff radius $r_c$ is $2.135a$. The phase diagram for Silberstein and Clapp's potential has not been determined, but they claim that both fcc and bcc are stable, with bcc favored at low and fcc at high densities.

### 3.4.2 Other applications

Dzugutov et al. have used their potential on various occasions to study supercooled liquids and amorphous materials [49, 50, 51, 52, 53, 54] and to compare them to crystals [195, 196].
Roth and Gähler studied diffusion and flip diffusion in dodecagonal quasicrystals [171, 172].
Modifications of the Dzugutov potentials, which favor other alloys like $\gamma$-brass for example, have also been introduced [229].
Most recently the original potential and modifications of it have been applied in the study of polytetrahedral atomic clusters by Doye et al. [42, 43].

### 3.4.3 The phase diagram of the Dzugutov potential

Stable structures for the Dzugutov potential have been obtained by Roth with molecular dynamics simulations and by Denton with density functional methods [170]. The high-temperature structure of the phase diagram of Dzugutov potentials with reduced maxima has been obtained

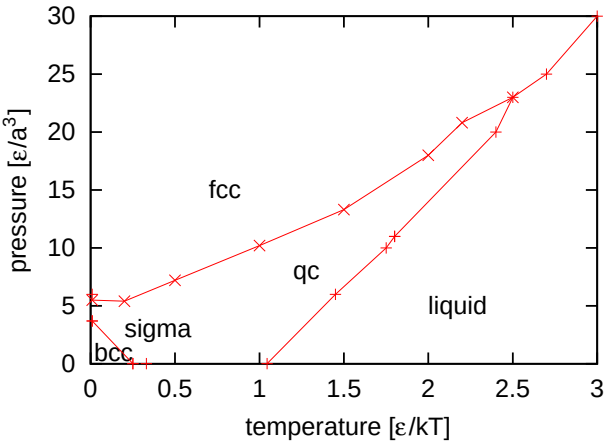


**Figure 3.13:** Temperature-pressure phase diagram for the Dzugutov potential.

by Roth [163]. Meanwhile the low-temperature phase diagram has been improved with the help of direct free enthalpy calculations [161].

At low temperatures and pressures the bcc-phase is stable in a very small triangular pocket between $kT = 0/P = 0$, $kT = 0.4\epsilon/P = 0$, and $kT = 0/P = 5.5P_0$ (Fig. 3.13).

Close-packed phases with different stacking sequences are largely degenerate due to the short range of the potential which interacts only up to the third neighbor shell. These phases are stable above about $P = 6P_0$. The phase boundary moves slowly to higher pressures with increasing temperature and reaches $P = 10P_0$ at $kT = 1\epsilon$ ($kT = 1.02\epsilon$ is the melting temperature of the $\sigma$- and the bcc-phase at $P = 0$).

The $\sigma$-phase appears to be the stable phase below $P = 6P_0$ and above the domain of the bcc-phase. Care must be taken here, however, since with increasing temperature other tcp-phases and especially the quasicrystal phase may become more stable than the $\sigma$-phase due to the additional entropy caused by the freedom to (re-)arrange the tiles. The location in the phase diagram where the quasicrystal phase has been discovered is indeed included in the stability domain of the $\sigma$-phase [50].

For shock wave simulations carried out at low temperatures the phase

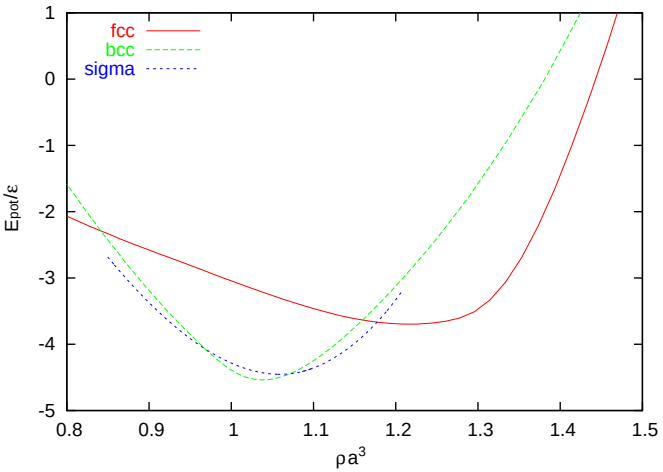


**Figure 3.14:** Phase diagram of the Dzugutov potential at $T = 0$. Three stable phases at different densities: bcc, the $\sigma$-phase, and fcc.

behavior at $T \approx 0$ is interesting (Fig. 3.14). From the curves we can determine the pressures at which the phase transition should occur in equilibrium.

### 3.4.4 Iron phase diagram

Topologically, the phase diagram of iron [6, 44, 21, 48] and the Dzugutov materials are similar with respect to low temperatures (Fig. 3.15). In both cases the low pressure structure is bcc ($\alpha$-iron) and the high pressure phase a close-packed structure. But there is no $\sigma$-phase in iron, and the phase boundary between fcc and bcc ends at a triple point with fcc ($\gamma$-iron). On the other hand, the bcc-phase with the Dzugutov potential is metastable in the whole range of existence of the $\sigma$-phase. But there is another connection to the $\sigma$-phase since the prototype is the alloy $Fe_{54}Cr_{46}$.

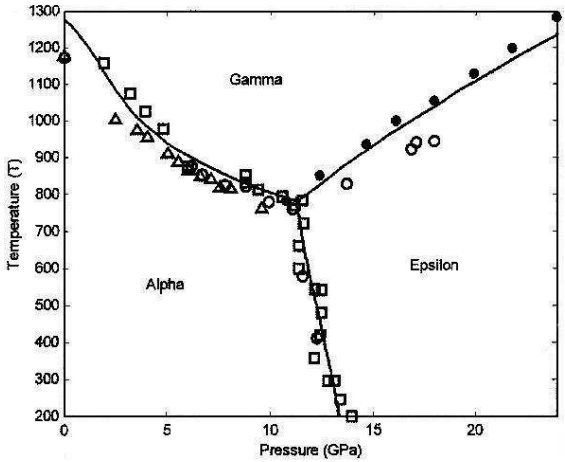


**Figure 3.15:** Phase diagram of iron. Alpha is the bcc-phase, Epsilon the hcp-, and Gamma the fcc-phase of iron. From [44].

## 3.5 The ω-phase

The high-temperature phase of the group-IV elements Ti, Zr, and Hf is bcc, usually called the $\beta$-phase. These elements, their alloys and the $\beta$-phase alloys of the noble metals exhibit a phase transition with correlated atomic displacements into an $\omega$-phase. The phase transition occurs both isothermally and athermally. It is reversible and cannot be suppressed by rapid quenching [218]. The $\omega$-phase forms small ellipsoidal inclusions ($\approx$ 1.5nm), aligned along the [111]-direction (See for example Fig. 32 in Ref. [218]). Cubical morphologies also occur [222].

It would be interesting to compare the ellipsoidal inclusions with the relics ("bullets") of the decaying solitary wave observed in our simulations (Chap. 6). But such a comparison requires much larger samples than the ones examined until now since only one bullet is created in these simulations.

The $\omega$-phase is a hexagonal two-layer structure which generated from the three-layer bcc through the collapse of two adjacent layers. If the three layers of bcc are called $A$, $B$ and $C$, then the perfect $\omega$-phase is

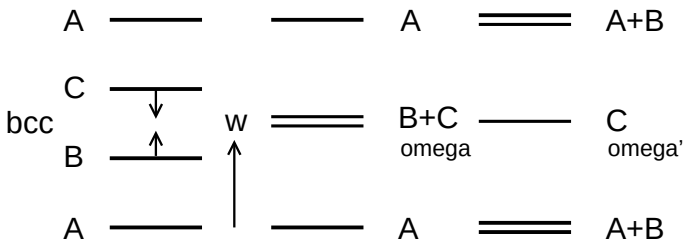


**Figure 3.16:** Transformation from bcc into the $\omega$-phase. Two variants are shown: the collapse of $B$+$C$ and the collapse of $A$+$B$.

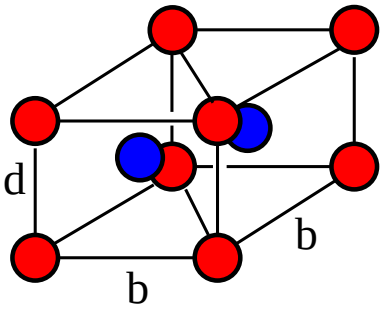


**Figure 3.17:** A unit cell of the $\omega$-phase. The colors indicate different layers, not different kinds of atoms.

generated if the $B$ and $C$ layers are shifted to the same $w$-coordinate (Fig. 3.16) where they form a hexagonal network.

Fig. 3.17 represents a unit cell of the ideal hexagonal $\omega$-phase. The red atoms form triangular layers, the blue atoms hexagonal layers at half height. If the blue atoms are not at the center we obtain the trigonal or crumpled $\omega$-phase. In alloys the different kinds of atoms usually occupy the red and blue sites at random even if they have the right stoichiometry for an ordered alloy.

The formation of the $\omega$-phase has also been observed in shock wave experiments of Ta and TaW alloys [106]. In this case the transformation is caused by inhomogeneous shear together with deformation twinning. Furthermore, a shock-induced phase transition has been reported in Zr from hcp to $\omega$ [199]. It is believed that the transition occurs by shearing

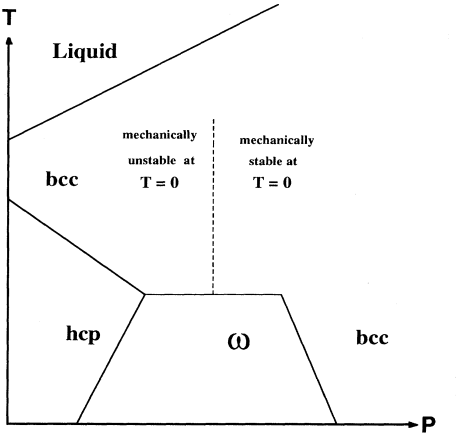


**Figure 3.18:** Schematic phase diagram of the chemical elements Ti, Zr, and Hf. From Ref. [2].

via hcp → $\beta$ → $\omega$. For a review of shock wave studies of Ti, Zr, and Hf (and other metals) involving hcp, bcc, and the $\omega$-phase see Ref. [192].

The $\omega$-phase is usually considered to be metastable, but it occurs as a stable high-pressure phase in the phase diagram of Ti, Zr and Hf (Fig. 3.18). For these materials, the low pressure $\alpha$-phase has hcp structure and the high temperature phase is the $\beta$-phase (bcc) [148]. Ahuja et al. [2] have studied the stable crystal structures of Ti, Zr, and Hf. The phase diagram obtained is in agreement with the experimental results except that they find that bcc becomes stable again at the highest pressures. First principle calculations of 4d-transition metals [68] show that energy of the $\omega$-phase should be close to bcc for Y, have a transition for Zr and should be unstable for Nb.

The basic source about the occurrence of the $\omega$-phase in materials[6], its formation by cooling or compression, and its properties is still the review by Sikka et al. [193].

[6]The only case where the $\omega$-phase has been found in the iron-chromium system is mentioned in a study of anomalous x-ray scattering by Reinhard et al. [155].

## 3.6 The bcc-lattice anomaly

Falter et al. [59, 60, 58] have shown that the dip of the longitudinal phonon modes in bcc crystals at $\frac{2}{3}[111]2\pi/a$ is due to an intrinsic geometric effect caused by the cancellation of certain Fourier components in reciprocal space. This effect can be reduced or enhanced by electronic effects. Ho et al. have studied the vibrational frequencies of bcc transition metals [90, 91]. They could show that the softening of the longitudinal phonon modes at $\frac{2}{3}[111]$ depends on the interatomic forces. It is decreased for Mo, normal for Nb, but strongly enhanced for Zr. Their results agree very well with experiment. For Zr they find a clear instability of bcc due to the longitudinal phonon mode.
The bcc anomaly can help to explain that the solitary waves and perhaps also the $\omega$-phase show up for simple pair potentials and for specific EAM potentials since it shows that the interactions may play a lesser role.
Noda et al. [146] and Zhorovkov and Kulagina [236] have presented an elaborate study of all kinds of phonon softening in bcc. There are various cases which lead from bcc to the $\omega$-phase and by martensitic transitions to fcc or hcp. All these instabilities are induced by transverse modes and do not play a role in our simulations. The only exception is the longitudinal mode with ideal wave vector $\frac{2}{3}[111]2\pi/a$ which leads to the $\omega$-phase. This is the mode observed in the shock wave simulations.

# Part II

# Simulations of Complex Structures

Chapter 4

# Shock Waves in the Cubic Laves Phase and in Binary Icosahedral Quasicrystals

## 4.1 Overview

Shock waves have been simulated in the cubic Laves phase C15, in related Frank-Kasper-type (AlCu)Li quasicrystals, and in an amorphous solid of the same composition and potential parameters. The goal of this study was to generate shock waves in periodic and aperiodic structures and to compare their behavior. The expectation was that new types of defects would show up in aperiodic materials. Binary models were studied first since all naturally occurring quasicrystals are at least binary and we wanted to treat a realistic quasicrystal.

Three regimes are observed in the Laves phase: At low shock wave intensity the system reacts elastically, at high intensities it turns disordered. In the intermediate region the velocity of the elastic wave saturates and an additional plastic wave appears. Extended defects are created which form a network of walls of finite width. The crystallites in between are rotated by the shock wave. If the samples are quenched a polycrystalline phase is obtained. The size of the grains decreases with increasing shock wave intensity until complete fragmentation occurs in the third regime.

The behavior of the quasicrystal models is similar, except that there is a continuous transition from a quasi-elastic behavior to the plastic regime. Ring processes are observed which break up into open paths when the shock wave energy grows. The transition to a complete destruction of the structure is continuous. In the amorphous solid a linear $u_s$-$u_p$-relation is found over the whole range of piston velocities. Two regimes are present, with unsteady plastic waves at weak shock strengths and steady waves in the range coinciding with the upper regime in the ordered structures.

## 4.2 Introduction

Shock wave experiments and simulations are valuable tools to expose a solid to strong uniaxial stress and to introduce defects without explicitly constructing them. Defects generated by shock waves have been studied in monatomic crystals to some depth [72,128,117,206]. The shock stress relaxes to an energetically more favorable hydrodynamically compressed state for example by slippage or phase transformations. Often stacking faults are created which permit a direct detection of the slippage.

For an ordinary crystal structure it is rather easy to construct slip planes and stacking faults and to analyze them. This is not the case for quasicrystals. If geometric constructions are used, complicated and rather arbitrary procedures have to be carried out to create for example dislocations and associated extended defects. These problems may be avoided if shock waves are studied: Now the structure itself selects the defect planes and the Burgers vectors. A drawback may be that most often high-energy defect structures are created, which may not be representative for slow deformations and low-energy plasticity.

The first goal of the present study was to find out whether quasicrystals behave different than other materials if they are traversed by shock waves. Many real metals and alloys as well as fcc model crystals with Lennard-Jones interactions, if shocked along the [100] direction [72], show a rather universal behavior with respect to the shock front velocity. This is true for quasicrystals, binary crystals and binary amorphous solids in the case of strong shock waves. For weak shock waves a deviation is observed due to elastic precursor effects. A similar deviation has been found recently for fcc crystals [72] along the [110] and the [111] directions.

The second goal was to find out if new kinds of defects occur in the quasicrystal. Often stacking faults are observed which are the trace of the slippage. Twinning and martensitic deformations are also very common. In quasicrystals all these defects are allowed but additional types of defects are possible: flips, where a few atoms change to alternative sites, phason walls, where after slippage the aperiodic sequence of lattice planes does not fit anymore, or transformations to crystals and approximants. It turns out that in the models studied here the defects which show up in the quasicrystals are indeed different from those expected for monatomic crystals but that they are similar to those in the closely

related binary Laves crystal. Weak shock waves merely cause elastic distortion whereas strong shock waves destroy the structure completely. Therefore they both will not be studied in detail. We will concentrate on the defect structures generated in the intermediate range.
The relation between the shock wave velocity $u_s$ and the piston velocity $u_p$ is studied in detail for shock waves along all major symmetry directions. The question of steadiness of the wave profiles will be discussed. The defects accompanying the transition from elastic to plastic behavior will be described for the four-fold crystalline[1] and the two-fold icosahedral direction. Further results have already been published elsewhere [164, 166, 167].
The influence of the ordered structure on the effect of shock waves is addressed in the last section where shock waves in an amorphous material with the same composition have been simulated. In contrast to the crystal and the quasicrystal the Hugoniot curve is almost perfectly linear, but there are also steady and unsteady waves.

## 4.3 Models, interactions, simulation details

### 4.3.1 The structure models

The structure models investigated in this chapter have been described already in detail in Sec. 3.2.2, except for the amorphous sample. Four models are used: the C15 Laves phase, the TI-model, the BI-model and an amorphous sample which has been generated from a crystalline sample by melting, quenching, equilibrating, and decompressing.

### 4.3.2 The interaction

The interactions were modeled by Lennard-Jones potentials for two reasons: first of all, there are currently no specific potentials available for quasicrystals of the Frank-Kasper-type. Secondly, we are not interested in the first place in the behavior of a specific material but in the general damage caused by shock waves. It may be argued that the Lennard-Jones potential is not well suited for alloys, but we will comment on

[1] The [100]-direction will be called four-fold axis for short although the space group of the C15 Laves crystal, $Fd\bar{3}m$, contains no four-fold rotation axis but only four-fold screw and roto-inversion axes.

this objection later in the discussion (Sec. 4.5). The radii of the potential minima have been adjusted to the average of the shortest $AA$, $AB$ and $BB$ distances. Such distances will be called bonds. The potential parameters are $r_{AA} = 1.0542a$, $r_{AB} = 1.23034a$, and $r_{BB} = 1.20395a$, where $a$ is half the edge length of the tiles. The cut-off radius for the potential was $r_C = 3.07476a = 2.5r_{AB}$. The depth of the potentials interacting between atoms of the same type is $-\epsilon$, and $-2\epsilon$ for atoms of different types. Since the potential parameters have been optimized for the TI-model, the coordinates of the Laves phase had to be rescale by 1.027 and of the BI-model by 1.0064 to obtain uncompressed initial states. With these potentials, the binding energy is $11.478\epsilon$ for the TI quasicrystal, $12.478\epsilon$ for the BI quasicrystal, $12.974\epsilon$ for the Laves crystal, and $10.564\epsilon$ for the amorphous solid.

### 4.3.3 Preparation of the samples and simulation details

The shock simulations were carried out in a NVE ensemble. Equilibrations were performed with the NVT-Nose-Hoover and NPT-Andersen ensemble, depending on the the volume or pressure to be fixed. The shocked samples were quenched first with the microconvergence (mic) method and then with the global convergence (gloc) method subsequently. The two-stage quenching process was necessary due to the large energy input during shocking.

The sample sizes ranged from 20,000 up to more than a million atoms for both crystals and quasicrystals. The samples are long rods with cross-sections between $14\times14$ to $61\times61a^2$ and lengths between 100 and $260a$. For the amorphous solid we used samples with 80,000 atoms and size $160 \times 14 \times 14a^3$. To permit periodic boundary conditions the perfect icosahedral quasicrystals is replaced by an orthorhombic approximant. After the samples were generated they are equilibrated for a time interval of usually $\Delta t = 10t_0$ (small samples sometimes up to $\Delta t = 30t_0$) at $kT = 0.001\epsilon$ and pressure $P = 0.01P_0$. A typical simulation lasts $\Delta t = 60t_0$. When the shock waves have passed through the samples they are quenched to $T = 0$ to remove the random displacements of the atoms caused by the heating and deformation. Of the order of 10,000 steps are typically required for the quenching.

Most runs were carried out with the symmetric impact method, except

for a few test runs with the momentum mirror method. No significant differences have been observed.

## 4.4 Results

Only a representative description of the results for the Laves crystal and the different quasicrystal models will be given in this section. Most of the results can be represented best by a series of pictures. Since we think that it would be too disruptive to display the pictures here, we have postponed them to a separate section where they can be studied side by side. A few single pictures will be repeated here to explain the results obtained from them.

### 4.4.1 Elasticity and anisotropy of the sound waves

In linear elasticity icosahedral quasicrystals behave elastically isotropic whereas the cubic Laves crystals are anisotropic. We have computed the elastic constants for a number of directions by quasi-static uniaxial deformation of the samples. The (quasi)-longitudinal velocity of sound is then given by $c_l = \sqrt{F/\rho}$ where $F$ is the elastic constant for uniaxial deformation and $\rho$ is the density. For the Laves crystal indeed a strong anisotropy is found (The indices are the lattice directions): $c_{l[100]]} = 14.29v_0$, $c_{l[111]} = 12.81v_0$, $c_{l[110]} = 13.20v_0$. The relation $4c_{l[110]} - 3c_{l[111]} = c_{l[100]}$ for cubic crystals is fulfilled. For the TI quasicrystal the velocities of sound along the major symmetry directions are $c_{l2} = 12.22v_0$, $c_{l3} = 12.29v_0$, $c_{l5} = 12.21v_0$. For the BI quasicrystal they are $c_{l2} = 9.88v_0$, $c_{l3} = 10.00v_0$, $c_{l5} = 9.95v_0$. The velocity of sound of the amorphous solid is $c_0 \approx 10v_0$. If all directions are taken into account an anisotropy of about 2% is found for the Laves crystal while only 0.2% are calculated for the TI quasicrystal and 0.8% for the BI quasicrystal. An explanation for the larger anisotropy of the BI samples may be that their icosahedral "quality" is worse since the modification of the structure is more severe.
In the elastic shock wave regime the relation $u_s = au_p + b$ holds between the velocity of the shock wave $u_s$ and the piston velocity $u_p$. If the strength of the shock wave goes to zero, the velocity $u_s$ should be the velocity of an elastic sound wave. The constants $b$ derived accordingly

are indeed close to the velocities of sound $c_l$ obtained from the quasi-static computations for all directions that have been studied in the simulations.

### 4.4.2 Pressure profiles and steadiness of the profiles

**Nature of the wave fronts**

The behavior of the samples with increasing shock strength can be subdivided into three regimes with respect to the observed wave fronts. The criterion is the steadiness of the wave profiles.

Here we will shortly sketch the three different regimes occurring in the simulations. Details about the pressure profiles and the $u_s$-$u_p$-relation follow in the next sections.

In the simulations presented here, a single steady elastic wave front is observed below $u_s/c_l \leq 0.3$. Between $u_s/c_l = 0.3$ and 0.6, a two wave structure is found. More precisely, the previous elastic front is turned into an elastic precursor which reaches a steady state during simulation, followed by a continuously spreading plastic precursor. A steady plastic front is not present. Above $u_s/c_l = 0.6$, steady waves are occurring. A steady elastic wave front is immediately followed by a steady plastic front moving at the same speed. With increasing shock strength, the elastic precursor in the second regime develops continuously into the steady plastic front in the third regime by steepening of the profile.

Although the plastic profiles in the second regime are non-steady, the structure itself reaches a steady state at the center where the shock waves started. This indicates that the uniaxial pressure and the shear stress converge to a finite value and the structure relaxes.

**Pressure profiles**

During simulation, the distributions of the instantaneous pressures averaged over the cross section of the samples are computed as a function of the propagation direction $x$ and time. From the uniaxial components $P_{xx}$, $P_{yy}$, and $P_{zz}$ the hydrostatic pressure $P = (P_{xx} + P_{yy} + P_{zz})/3$ and the shear pressure $S = P_{xx} - (P_{yy} + P_{zz})/2$ can be derived. In the following we will concentrate on the uniaxial pressure $P_{xx}$ and the shear pressure $S$. The shape of the pressure profiles as a function of the piston velocity $u_p$ fits exactly into the three regime picture set up in Sec. 4.4.2. The results are as a rule identical for all samples and all

directions, therefore they will be presented summarily. Differences will be pointed out where appropriate.
In the first elastic regime $P_{xx}$ and $S$ rise sharply at the shock front and stay constant along the sample (Fig. 4.1 and 4.2, Laves crystal). The samples are compressed uniaxially, and no plasticity is observed. In the Laves crystals up to four oscillations with an amplitude of half the plateau value and a wavelength of about $7a$ are found. They are not present in the quasicrystal and are similar to the locked-in solitary waves described for example by Germann et al. [72].
In the second regime where defects are created, the wave profile as a whole *does not* become steady during simulation (Fig. 4.1 and 4.2, TI quasicrystal at $u_p/c_l = 0.37$). The shear pressure $S$ rises sharply, but then it decays continuously the whole way down to the center of the sample. The uniaxial and the shear pressure at the center of the sample drop during simulation, indicating a relaxation of the structure. But if $u_s/c_l$ is larger than about 0.25 for the TI model and 0.4 for the Laves crystal, a constant value is reached after some time, indicating that the structure has reached a relaxed state. There is a remarkable difference between the quasicrystal models and the Laves crystal: In the quasicrystal $S$ falls of directly behind the shock front whereas in the Laves crystal a plateau exists which proves that the elastically compressed sample breaks and plasticity sets in with delay. The uniaxial pressure $P_{xx}$ behaves somewhat complementary: Instead of the sharp rise and slow decay it grows slowly until it reaches a plateau at the location where $S$ has dropped to about the half of its peak value. If $u_p$ is larger than 0.45 in the case of the Laves crystal, the convergence of $P_{xx}$ and $S$ to a constant plateau can already be anticipated. In the Laves crystal the oscillations of the profile in the elastically compressed part of the sample as described in the first regime are still observable.
In the third regime the curve of the shear pressure $S$ resembles the shape in the second regime at a first glance, but now the profile is clearly steady (Fig. 4.1 and 4.2, TI quasicrystal at $u_p/c_l = 0.62$). The shear pressure first rises sharply at the shock front, but then it drops within a fixed interval of 10 to $15a$ to its final plateau value. The uniaxial pressure $P_{xx}$ grows slowly within the same range. Hence the plastic destruction sets in after only a very short elastic reaction.
In a liquid the shear pressure $S$ should drop to zero after shock compression since there is no shear elasticity and the liquid can flow freely.

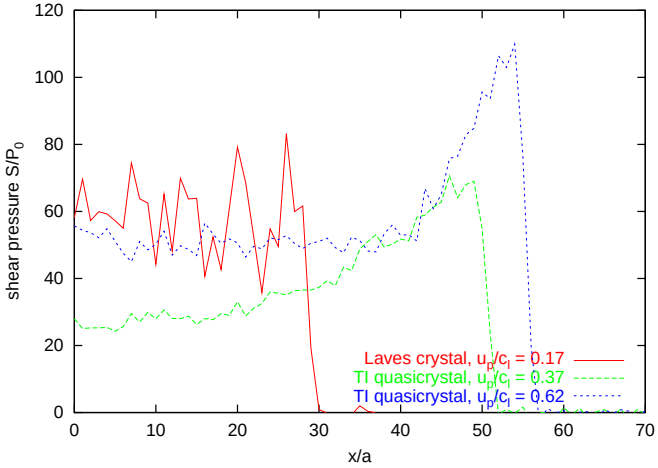


**Figure 4.1:** Shear pressure $S$ of three samples representative for the three regimes.

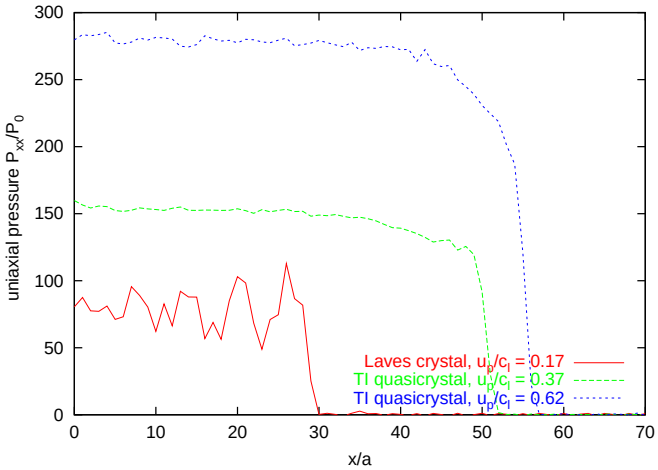


**Figure 4.2:** Uniaxial pressure $P_{xx}$ of three samples typical for the three regimes.

Such a behavior is certainly not found in our simulations, neither in the second, nor in the third regime. The shear pressure is a monotonously rising function of the piston velocity $u_p$ with changing slopes in the three regimes. It is expected that $S$ will drop due to relaxation processes. But they are too slow to be observed on the simulation time scale.

### 4.4.3 The Hugoniot relation $u_s$-$u_p$ in general

The velocities $u_s$ of the wave fronts were determined in two ways: either from the slope of the wave fronts in time-distance contour plots, or directly from histograms of the uniaxial or shear pressure with time as a parameter. Two factors limit the accuracy: Often there are large fluctuations of the pressures, and sometimes slow relaxation phenomena occur leading to decreasing wave velocities and changing pressures. The fluctuations are caused by the discrete nature of the sample which leads to a strong variation of the number of particles in the histogram bins. This problem is even more severe in the case of the aperiodic, but well ordered quasicrystals. The fluctuations can be avoided to some degree by averaging in a comoving frame, but only if the wave profile is steady. The relaxation phenomena themselves can only be avoided by much longer simulation times which also require much larger samples lying beyond our current computing capacities. It must be stressed, however, that larger simulations are not expected to lead to qualitatively new results since relaxed states can be obtained at the center of the samples if the shock strength is not too small.
In Fig. 4.3 we present the typical form of a $u_s$-$u_p$-Hugoniot plot for shock waves in the Laves crystals along the four-fold direction and in the TI quasicrystals along the two-fold direction, respectively. The BI quasicrystals show similar behavior. The curves are characteristic for a material which reacts elastically below a certain threshold. Then delayed plastic deformation sets in until at high shock intensities the structure is destroyed directly behind the shock front.
At low piston velocities elastic shock waves and a material-dependent gradient are observed. The slopes $(u_s - c_l)/u_p$ are 3.1 for the crystal and about 2.6 for the quasicrystals. The values are independent of the starting temperature of the sample.
The crossover from delayed to immediate plastic behavior takes place

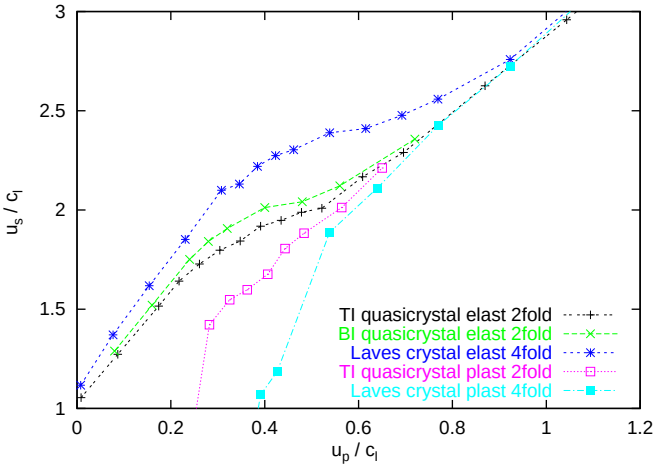


**Figure 4.3:** Shock *vs.* piston velocity. At low piston velocity (quasi-) elastic behavior is observed. Between $u_p/c_l = 0.3$ and 0.6 approximately a crossover to the plastic shock wave and finally the change of slope to a material-independent value is found. The velocities $u_p$ and $u_s$ are scaled by the velocity of sound $c_l$ valid for the different directions.

between 0.3 and 0.6 $u_p/c_l$. The elastic front from the first regime is turned into an elastic precursor wave. Its height first decays slowly but it becomes steady during simulation. The elastic front is followed by a non-steady plastic precursor. The velocity given in Fig. 4.3 is not a shock front velocity, but the velocity of half height between the peak value of the shear pressure and its value at the center of the sample. This velocity is not half of the speed of the elastic wave, since the relaxation of the shear pressure is nonlinear across the sample. The half-height velocity is presented since it demonstrates how the sample switches from non-steady to steady behavior across the second regime. At high piston velocities above about $u_p/c_l = 0.6$, the material-independent plastic behavior occurs and *steady* shock waves are found. The elastic wave front is followed immediately by the plastic wave. In this regime the finite yield strength of the solids does not play a role any more.

In the whole range from $u_p/c_l = 0.2$ up to $u_p/c_l = 1.0$ at least, an additional *elastic* wave front is observed at the beginning of the simulation, moving with a velocity that has a constant slope $(u_s - c_l)/u_p = 3.1$ for the crystal and 2.6 for the quasicrystal respectively, the same velocities as in the elastic regime (This wave is not shown in Fig. 4.3). It represents an elastic "one-dimensional" precursor wave. After a simulation time of $t = 0.05t_0$ the precursor wave vanishes and the ordinary elastic and plastic wave fronts take over. Obviously it takes a certain time interval until the coupling between the shock wave direction and the transversal directions becomes effective.
The Hugoniot curves obtained in the simulations do not depend on the sample cross-section and on the length of the rod as long as the shock wave has not penetrated the whole sample during simulation time and no interference with reflected waves has taken place.
In the crystal the crossover from elastic to plastic behavior occurs at shock wave intensities higher than in the quasicrystal. One reason may be that the local environment of a *single* atom is more symmetrical, while the opposite holds for the *averaged* environment. The transition to plastic behavior has to break the local symmetry to couple the normal and the transverse directions. The trigger are the random fluctuations induced by temperature, and the mechanism works better for lower site symmetry. A further reason will be presented in Sec. 4.4.8.
Usually there are sharp kinks in the Hugoniot plot between the different regimes if a phase transition occurs, with a flat gradient in the central part. The reason for the rather weak change of the slope in our case at about $u_p/c_l = 0.6$ may be on the one hand the difficulty to determine $u_s$ accurately. But on the other hand there is no clear distinction between the second and third regime since we do not have an ordinary phase transition but a fragmentation of the sample with decreasing grains. The third regime is reached when the fragment size is of the order of a few interatomic distances. The reason why there is no kink between the first and second regime for the quasicrystals will be discussed in the Sec. 4.4.8.

### 4.4.4 Orientation dependency of the $u_s$-$u_p$-relation

Fig. 4.4 shows the Hugoniot plot for various propagation directions. In the TI-quasicrystals the curves along six different directions are all

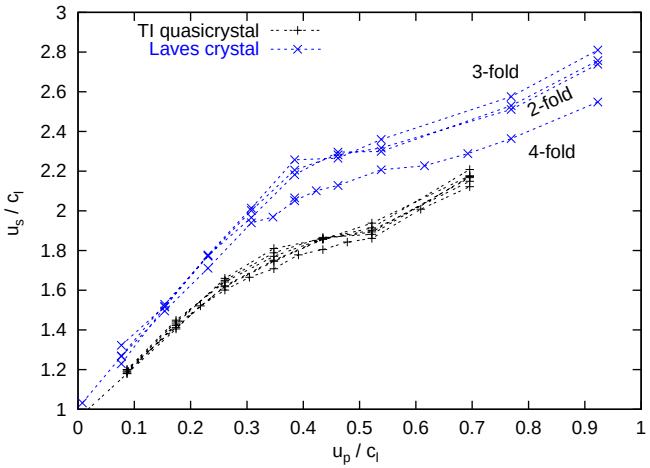


**Figure 4.4:** Orientation dependency of the shock vs. piston velocities. The quasicrystal curves are identical if errors are taken into account. Therefore they are not marked individually. For the Laves crystal, the velocities along the four-fold direction differ from the other orientations which on their part are again quite similar. The velocities $u_p$ and $u_s$ are scaled by the velocity of sound $c_l$ valid for the different directions.

identical within the error bars if scaled with the velocity of sound for these directions. The result is a first hint that the plasticity modes are the same for all directions in the quasicrystal.
For the Laves crystal, the curves for shock waves propagating along the the three-fold and two-fold axes and in the direction perpendicular to a mirror plane are rather similar whereas a significant deviation exists for shock waves along the four-fold direction. The difference between the curves in the second and third regime vanishes, however, if the velocities of the shock waves are scaled with the individual sound velocities. As in the case of quasicrystals, we conclude that there is no basic difference in the plasticity modes for the different shock propagation directions.

### 4.4.5 Dependency of pressure and stress on the shock strength

Complementary to the $u_s$-$u_p$-Hugoniot diagram is the representation of pressure and stress with respect to the piston velocity $u_p$. We have plotted three observables: the hydrodynamic pressure $P$ and the maximal shear stress $S_e$ at the center of the sample. Since we have applied the symmetric impact method, this gives us the stress at the position where the system had the longest time to relax. As described in Sec. 4.4.2, no steady behavior could be achieved in the elastic-plastic regime. The third value is the maximal peak value $S_p$ of the maximal shear stress at the elastic front. It occurs before the material yields. The end of the elastic or quasi-elastic regime are clearly visible around $u_p/c_l = 0.43$ for the Laves crystal (Fig. 4.5) and $u_p/c_l = 0.25$ in the case of the quasicrystal (Fig. 4.6). The distinction between the elastic-plastic and the overdriven regime is not so sharply determined in agreement with the $u_s$-$u_p$ Hugoniot data.
The curves for the Laves crystal and the quasicrystal models are plotted for several directions in the same graph. It is obvious that the scatter of the data is in the same range as the direction dependency. The data for the quasicrystal models also show that $P$ and $S$ are independent of the specific model. The main difference between the Laves phase and the quasicrystal models exists in the (quasi-)elastic regime, where the ring processes (See Sec. 4.4.8) lead to a reduction of the stress already.
The increasing maximal shear stress $S$ beyond $u_p/c_l = 0.5$ for the quasicrystal models and $u_p/c_l = 0.6$ for the Laves crystal indicates that the

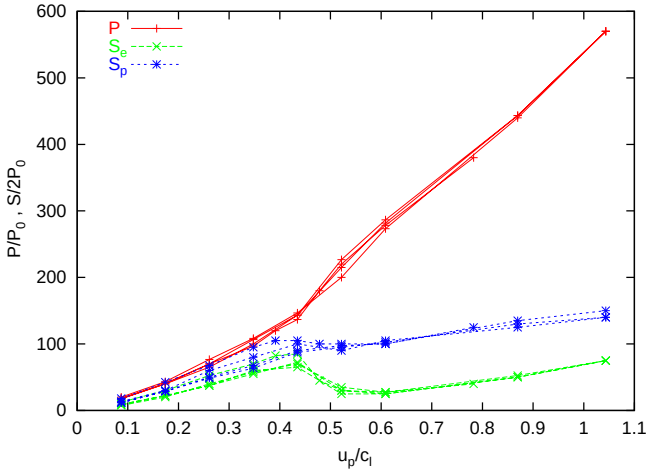


**Figure 4.5:** Hydrostatic pressure $P$ and shear stress $S$ as a function of $u_p$ for a Laves crystal. $S_e$ and $P$ are measured at the center of the sample, $S_p$ is the peak value of $S$ before the material yields. The different curves of the same color indicate different shock wave directions.

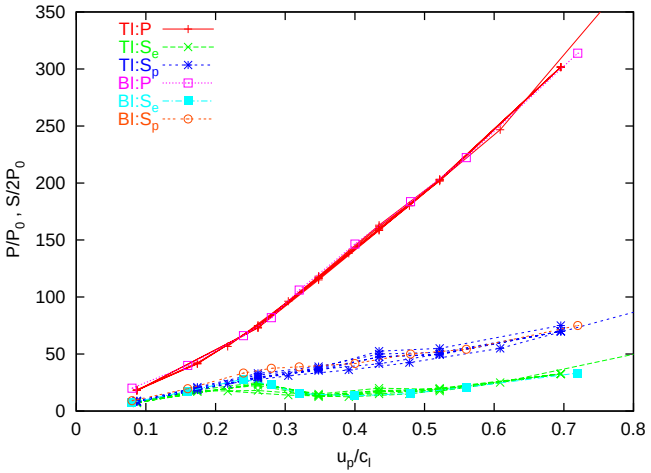


**Figure 4.6:** Hydrostatic pressure $P$ and shear stress $S$ as a function of $u_p$ for a TI quasicrystal shock along different directions and a BI quasicrystal shock along the two-fold direction. $S_e$ and $P$ are measured at the center of the sample, $S_p$ is the peak value of $S$ before the material yields. The different curves of the same color indicate different shock wave directions.

simulation time is too short or the samples are too short, respectively, for the system to relax completely.

### 4.4.6 Analysis of defects

Defects in quasicrystals are much harder to analyze than in ordinary crystals. In a crystal there is usually only a small number of different atom sites and a small number of neighborhoods. After a modification of the crystal it is easy to compare the status of an atom, for example its potential energy and the number of neighbors, to the allowed values in an ideal structure and to figure out which atoms belong to a defect. Such a procedure is not possible in a quasicrystal. Certainly, the environments of the atoms can be classified if only near neighbors are taken into account. In each class the atoms have another binding energy. But even in simple models like the ones considered here there exist of the order of 40 ideal environments which often differ very little from one another. Thus it is challenging to find out whether a change in the binding energy is due to a defective environment. To solve the problem we have tabulated the binding energy of each atom at the beginning of the simulation and compared the instantaneous binding energy to the stored value. Since the atoms vibrate around their equilibrium position and exchange kinetic and potential energy one has to introduce a temperature dependent tolerance interval for the binding energies. There are, however, still two possibilities if a change has occurred: the atom has jumped into another allowed neighborhood class, or it has become a defect atom.

Since shock waves generate large changes in energy, these classification methods do not work well for quasicrystals and also not for crystals. There is a second reason for the failure: the defects are not localized, but extended. We tried out several other indicators, but none worked well. The best we could find was a rescaling of the sample after the shock wave has passed, in such a way that the distances between the initial and final position of the atoms were minimized. The minimization can easily be carried out qualitatively by trial and error if the displacement vectors are plotted as in Fig. 4.7. Then the scaling is varied until the vector lengths become as small as possible. A good overview of the defects is obtained if the shortest displacement vectors (or the longest) are removed and the remaining are plotted. The procedure permits

us to extract vortices and thereby to map out the local rotation axis. A three-dimensional impression can be obtained by cutting slices and comparing them (Fig. 4.7).
A second method which will work for any structure is to produce a list of nearest neighbor atoms in the initial structure. If a pair of atoms is in the list we say that the atoms are bound. By computing similar lists of atoms in the final states one can determine which bonds have been broken and if new bonds have been created.
A third procedure which turned out to be very helpful was to quench the sample after the shock. We discovered that it removes not only the kinetic energy and puts the atoms back into their local force-free state, but eliminates most of the local rotation of the sample (Fig. 4.8).

### 4.4.7 Laves crystal

Due to periodicity the results for Laves crystals are much simpler to analyze than those for quasicrystals. Therefore they will be treated first.
The crystal structure remains perfect up to $u_p/c_l \approx 0.37$ which tells us that only elastic distortions occur in the first regime. Close to the shock front large displacements may be found, but these are transient phenomena.
Within a short interval of about $u_p/c_l = 0.1$ the behavior changes abruptly. Extended defects appear which separate perfectly crystalline domains. The defects start to fill up the bulk with increasing strength of the shock wave. Beyond $u_p/c_l \approx 0.57$ the initial structure seems to be destroyed completely by the shock wave. The size of the fragments into which the single crystal breaks become so small that the structure can no longer be distinguished visually from a disordered material. The radial distribution function, however, still contains a few discrete maxima since some small ordered regions are left over.

#### Defect bands in situ

A slice through the atomic displacement field represented in Fig. 4.7 illustrates the structure of the extended defects. Bands are visible with a width of up to 10 interatomic distances $a$ and a separation of the order of $35a$. The bands are shear grain boundaries which separate different

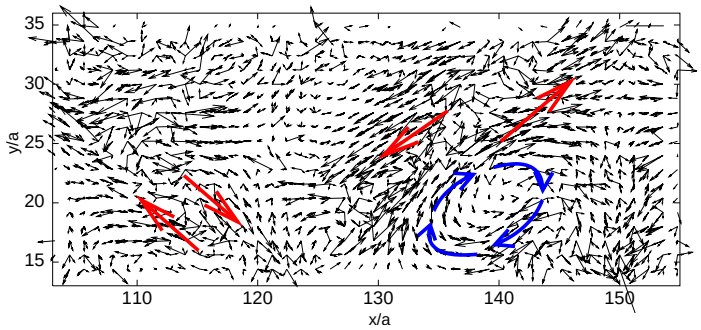


**Figure 4.7:** In situ displacement field of the Laves crystal at $u_p/c_l = 0.45$. The large antiparallel red arrows indicate slip planes. The ring of large blue arrows marks a rotation axis. Pictures of the quasicrystals look similar. The numbers at the figure represent the size in nearest neighbor distances $a$.

crystallites. It could be speculated that the bands are still molten, but such an assumption could not be confirmed by local temperature maps.

Within the crystallites rotation axes are observed. The edges and corners of the crystallites are given by hyperbolic points (not visible in the figure). These are locations, where displacement vectors point towards one another along one direction while they point in opposite directions along a directions offset by 90 degrees. Thus the original single crystal is broken into crystallites which are deformed and rotated with respect to their initial orientation. If slices parallel to the coordinate directions are cut through the displacement field and compared we find that neither the grain boundaries nor the local rotation axis are perpendicular to the cutting direction. The local rotation axes turn out to be parallel to the face diagonals of the simulation box. Since the cuts through the grain boundaries are also parallel to the face diagonals we can conclude that the grain boundaries are perpendicular to the three-fold axes.

To our knowledge the rotation of crystallites in shock wave simulations on an atomic scale has not been reported before. Similar structures are well known from mesoscopic shock wave simulations by Yano and Horie [223, 224] and by Makarov and co-workers [11, 227, 131, 130] and discussed for example by Lee [125]. In the mesoscopic simulations the

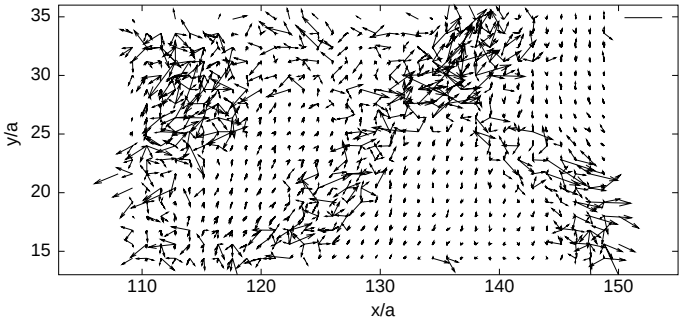


**Figure 4.8:** Displacement field of the Laves crystal at $u_p/c_l = 0.45$ after quenching. Shown is nearly the same part of the sample as in Fig. 4.7. Pictures of the quasicrystals look similar. The numbers at the figure represent the size in nearest neighbor distances $a$.

initial structure is already polycrystalline and phase boundaries exist, whereas in the simulations presented here we start with a single crystal which is broken into grains during simulation.

A sequence of pictures of the displacement fields for different shock strength is given in Sec. 4.6, Fig. 4.20.

### Defect bands after quenching

Fig. 4.8 shows the displacement field of the sample after quenching. The rotational part of the displacement field has disappeared, only the relative shift of the crystallites remains. The fragments can also be identified in a slice through the crystal (Fig. 4.9). If the broken bonds are visualized we find that they mark the edges of the grains which look like more or less irregular polyhedral blocks. The final state of the quenched sample has been presented by Davison [37] as one of the states that occur if the deformation of the sample is not uniform.

Sequences of pictures of the displacement fields (Fig. 4.21), the textures of the crystallites (Figs. 4.13 and 4.14), and the broken bonds (Fig. 4.18) for different shock strength are given in Sec. 4.6.

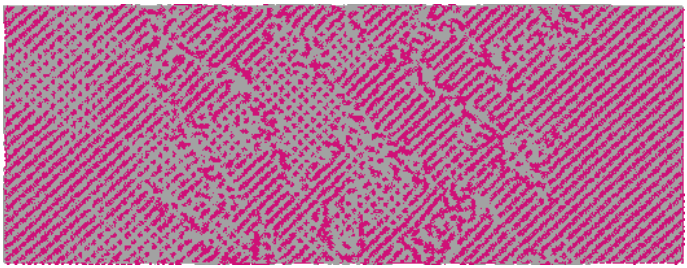

**Figure 4.9:** Slice through the whole Laves crystal at $u_p = 5.5v_0$ after quenching ($260 \times 61a^2$). The various textures (dotted and striped) are generated by displacements of parts of the sample with respect to each other and represent the newly created grains.

**Summary of the defects in Laves crystals**

The Laves single crystals are broken into grains by the shock wave in the second regime. The boundaries between the grains are broad disordered bands. The grains still contain the original Laves crystal structure, no phase transitions or twinning has been observed. The spacing between the bands depends on the cross section of the sample since the bands are replicated by the periodic boundary conditions. In the case of small cross sections the boundary conditions may even pretend a disordered state in the second regime. Stacking faults have not been observed and dislocations could not be detected.

If the shock wave intensity is increased, the general behavior of the Laves crystal does not change. The grains get smaller and smaller and the defect bands closer and closer until it is no longer possible to distinguish grains and bands. Then the third regime has been reached where the sample structure is destroyed completely.

### 4.4.8 Quasicrystal models

The Hugoniot curves for the quasicrystals look similar to those of the Laves crystal. A first glance at the samples shows that the quasicrystals stay intact up to a piston velocity of about $u_p/c_l = 0.25$. But there is no sharp boundary between the (quasi-)elastic and the plastic regime

(Fig. 4.3). The reason will be discussed in the next paragraphs.

**The TI-quasicrystals**

In the TI model the ring processes, which are well known from equilibrium simulations, are enhanced by the shock wave and are observed already at very low shock wave intensity $u_p/c_l = 0.09$ (Fig. 4.10). With increasing shock strength the rings break up and the atoms start to move around randomly (at $u_p/c_l = 0.17$). Well separated chains of atoms are now observed. At $u_p/c_l = 0.22$ it is no longer possible to speak of chains. We find clouds of atoms in motion. At $u_p/c_l = 0.26$ we finally have a situation similar to the Laves crystal: the sample is broken into crystallites which are shifted and rotated.

Thus we have two plasticity modes: the ring and chain processes which take place in the interior of the grains and the disruption of the single crystal into domains. This is the reason why there is no sharp boundary between the different shock wave regimes. In addition to the aperiodicity of the quasicrystal it is also the reason why it is so much harder to visualize the (quasi-)crystallites. The broken fragments are similar to those in the Laves crystals, but there shape is less polyhedral and the grains are smaller.

**Behavior of the BI-model**

In the BI model the ring processes are suppressed completely since the configurations of tiles responsible for the jumps have been removed. Only single atom flips are allowed. The displacement of the atoms at the shock front is large enough that some of them can jump to alternative sites where they remain after the shock wave has passed (Fig. 4.11). The jump locations can be considered as double-well potential sites. Since both positions are equivalent with respect to energy but separated by a barrier the atoms will not move back to their initial site.

Due to the point defects the transition from the elastic to the plastic regime is again much smoother in the BI-quasicrystals than in the Laves crystal. Since the number of jumps and the atoms involved are much less in the BI model than in the TI model the defects alone cannot be responsible for the weakness of the quasicrystals. Another reason has been pointed out in Sec. 4.4.3: Although the global symmetry of the icosahedral quasicrystals is higher than that of the cubic Laves crystals, locally many atoms in the quasicrystals have lower symmetry than the

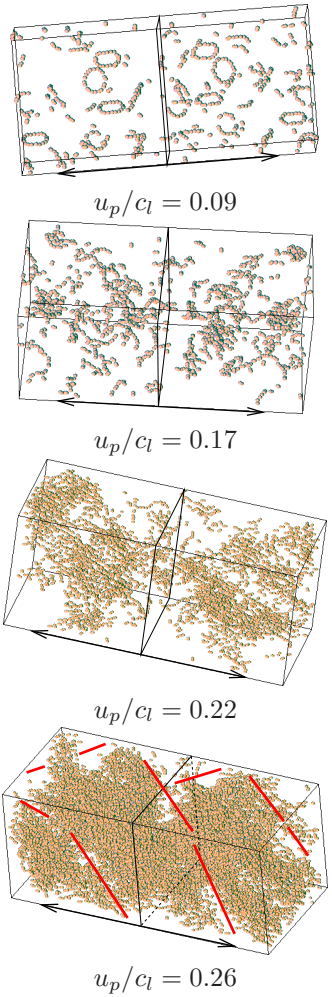


**Figure 4.10:** Sequence of shocked samples of the TI-model. The double arrows indicate the path of the shock fronts starting at the center of the box. The red lines represent the local rotation axis. In the first three pictures the spheres represent the jumping atoms directly, while in the last two pictures they are overshadowed by clouds of atoms with large displacements.

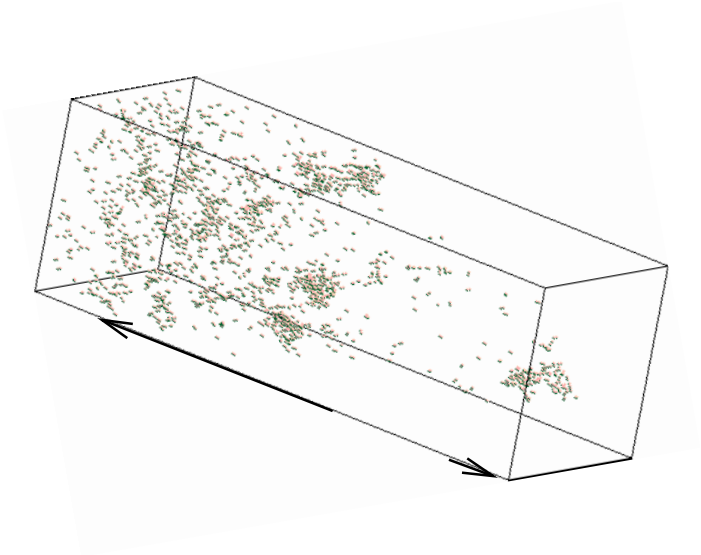

**Figure 4.11:** Shock wave in the BI-model. The shock waves started at the right half of the box, approximately in the middle between the end points of the arrows. In the instant represented in the picture the left-moving wave is at the left end of the box, whereas the right-moving wave has already left the box. The dots indicate atoms with large displacements. In the left part of the box the displacements are transient since they disappear some time after the shock front has passed as can be seen by comparison with the right half of the sample. At the place where the shock waves started only a few singular points are left which mark the sites where atoms have jumped to alternate positions.

atoms in the Laves crystal. We believe that this is the true reason why the threshold to generate defects is reduced considerably in the quasicrystal.
The pattern of defect bands and displacements is qualitatively similar to the Laves crystal. There is only one difference: in the quasicrystal models the crystallites are always smaller and the defect bands closer together if the results at equivalent shock strengths are compared (See Fig. 4.18 and Fig. 4.19 or Figs. 4.20 and 4.21 compared to Figs. 4.22 and 4.23).

**Summary of the quasicrystal results**
Between $u_p/c_l = 0.25$ and 0.5 extended defects can be observed in both quasicrystal models. A process similar to the one in the Laves crystals takes place: the grains get smaller and smaller and the defect bands move closer and closer together. At shock waves stronger than $u_p/c_l = 0.5$ the quasicrystals appear disordered since defect bands and grains can no longer be distinguished.
Again we find no stacking faults and no dislocations. Quasicrystal-specific defects like phason walls have also not been observed. Although we have seen atoms jump, we know [173] that these processes are *no* quasicrystal flips since they do not change the rhombohedron-dodecahedron tiling. Real flips are very complicated in the quasicrystal models presented here and involve at least 10 atoms.

### 4.4.9 Amorphous solid

In the case of the amorphous solid we find a universal behavior for all shock front velocities: The slope of the Hugoniot curve is $u_s/c_0 = 1.85 \cdot u_p/c_0 + 1.0$ up to $u_p/c_0 = 1.0$ (Fig. 4.12). This is no indication, however, that the amorphous structure behaves like a fluid. If we consider the pressure profiles, especially the shear pressure, we find that up to $u_p/c_l = 0.2$ the profiles are unsteady as a whole. There is a steady jump from the elastic compression wave followed by an slow decay which lasts the whole length of the sample. At $u_p/c_l = 0.3$ we find a transitional behavior, but at $u_p/c_l = 0.4$ we clearly observe steady waves. The shear pressure decays within a short interval to a finite constant value. If we compare this behavior to Fig. 4.3 we find that the transition to the steadiness of the plastic waves occurs at approximately the

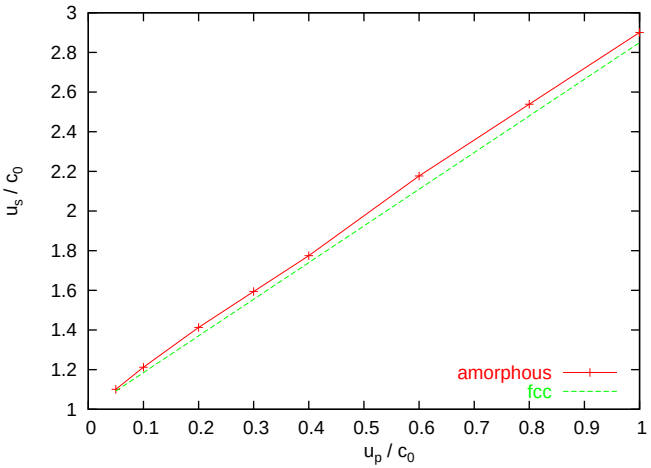


**Figure 4.12:** Shock vs. piston velocity for the amorphous solid. The fcc curve is from Holian and Lomdahl [99].

same shock strength as in the ordered samples. It also indicates that the amorphous solid possesses a finite yield strength since the shear pressure is not zero.
The amorphous solid stays disordered. No obvious change of the structure has been notified by inspection of the radial distribution function for example. In particular, crystallization has also not been observed.

## 4.5 Discussion

Our study has revealed another type of plasticity observable in atomistic simulations beyond simple dislocations and stacking faults [99] and phase transitions [72,117]. Here we find fragmentation of a single crystal into rotated crystallites separated by thick disordered walls.
The behavior of the crystal and the quasicrystal models used here in shock wave simulations is similar to the behavior of ionic materials: slippage is hindered by the creation of high-energy anti-phase boundaries. Dislocations are slow, rare and high energies are needed to generate

them [185]. The single-crystal ionic materials break into many crystallites and form broad defect bands [133]. In the models presented here it is not possible to exchange $A$ and $B$ atoms at random without destabilizing the structure. If an $AB$ bond is broken it will be replaced by an $AA$ or $BB$ bond which is only half as strong. Due to the nontrivial plane structure it may also happen that no new bond is formed. Furthermore the structure will be strained, since the different bonds are of different length. The average binding energy decreases. Thus processes allowed in monatomic structures turn out to be fatal. Recent crack simulations have shown that the Laves phase and the quasicrystal always behave brittle [160]. No dislocation emission could be observed.

On the other hand it is well known that stacking faults exist in Laves crystals and a synchroshear mechanism [82] has been proposed which should permit slippage. Since our models are stable in a large range of interaction strengths, it would be interesting to repeat the simulations with a parameter set where the repulsion is reduced. Calculations $\gamma$-surface[2] by C. Rudhart [176] for Lennard-Jones interactions limit the range of interesting variations. Although the heights of the energy minima and maxima vary, the overall topology of the surface stays largely the same. No shift vectors exist which would indicate low energy dislocation directions. The hope is now that the topology of the $\gamma$-surface changes if we replace the general potentials by effective pair potentials or EAM-potentials designed especially for quasicrystals and their relatives.

We have found that there is a material-independent Hugoniot relation governed by the interaction only in the case of strong shock waves. This is due to the complete destruction or amorphization of the structures, a phenomenon which is well known from high-pressure studies of C15 Laves phases.

We have tried to find crystal and quasicrystal structures which are as similar as possible. The best model would be monatomic, but no uniform simple monatomic quasicrystals exist. There are still differences in the average binding energies, the composition, and the local atomic environments in our models. Therefore we cannot rule out that part of the results (for example the different slopes in the Hugoniot plot) are

[2] The $\gamma$-surface represents the increase in energy with respect to a displacement vector if a sample is cut into two parts which are shifted laterally with respect to each other by this vector.

due to the structural differences.
Defect structures and plasticity modes have been presented for propagation directions of the shock waves along the four-fold direction in the Laves crystal which is oblique to the close-packed planes, and along the two-fold direction in the quasicrystal which is normal to the close-packed planes. Although these two directions are quite different with respect to the orientation of the prolate rhombohedra, the results are rather similar. Simulations in other symmetry directions have also been carried out, but they have not been discussed since no new phenomena have been observed. We consider this observation as a further indication that the phenomenology of the shock wave plasticity in the present study is governed mainly by the strength of the interaction and not by the type of structure.
Up to now no shock wave experiments have been carried out with quasicrystalline materials. High-pressure studies do not lead to the high temperatures typical for shock waves. It has been found that quasicrystals are often transformed into approximants under high pressure, but such a transition has not been observed in our simulations [4, 142].
The behavior of Laves crystals under high pressure is well-studied (See for example Lindbaum et al. [126] and Sec. 3.3). The crystals are preferably amorphized. Shock-wave experiments of Laves phases have not been found in the literature, especially no reports are known to us about the investigation of defect structures caused by shock waves.
In this chapter we have studied shock waves in diatomic icosahedral quasicrystal structures. We chose a model which is closely related to naturally existing quasicrystals and to familiar crystal structures. The interactions were modeled with generic Lennard-Jones potentials as specific interactions were lacking. The hope is that the results can be compared directly to experiments, but this has not yet happened.
Since it is our goal to study generic features especially and models as simple as possible we will now turn to monatomic quasicrystals which have not yet been observed in nature. A drawback in the monatomic case is that we have to use special interactions to stabilized the quasicrystal and that we must be satisfied with layered dodecagonal structures. In the end it turns out that the simulation of shock waves in Dzugutov materials is very exciting on its own since multiple phase transformations and solitary waves are found and that the behavior of a number of metastable phases can be compared.

## 4.6 Pictures of the diatomic simulations

This section contains additional pictures illustrating the results of the binary structure simulations in all three shock wave regimes. The pictures contain results from Laves crystals shocked along the fourfold direction and from TI- and BI-quasicrystals shocked along two-fold directions. We will give a few additional comments if necessary. Fig. 4.13 displays a part of the shocked Laves crystals. The different patterns correspond to different crystallites into which the single crystal is broken. The patterns can still be recognized in the pictures of the whole sample (Fig. 4.14). The same is not true for the quasicrystal (Fig. 4.15). It is easy to observe that the pattern changes, but the consequences are unclear.

The information from the transverse sections through the samples is similar (Fig. 4.16 and 4.17). The quasicrystal appears to be disordered already in the elastic-plastic regime, whereas regularities can still be found in the Laves crystal in the early plastic regime.

The pictures of the broken bonds (Fig. 4.18 and 4.19 are drawn for $AA$ bonds. The cases for newly created $AA$ bonds, broken $BB$ bonds and newly created $BB$ bonds look similar. The only difference is that there are far less $BB$ bonds. The data of the in-situ and the quenched samples are also similar.

The pictures of the bonds and the displacement fields (Fig. 4.22 and 4.23) help to solve the riddle of what happens in the quasicrystal: It is also broken into many crystallites. Please note that the displacement fields have been mapped to a regular grid!

A comparison of the pictures for the Laves crystal (Fig. 4.18, 4.20 and 4.21) and the quasicrystal (Fig. 4.19, 4.22 and 4.23) clearly show that the crystallites in the quasicrystal are smaller than in the Laves crystal.

The final pictures (Fig. 4.24 and 4.25) represent the parts of the displacement fields where the absolute value of the displacement vectors are smallest. Obviously, these parts form rods in diagonal directions as can be derived especially from Fig. 4.24, where the coloring indicates that the rods lie in plains are parallel to the coordinate axes.

We hope to have given an impression of the complicated three-dimensional processes going on in these shock wave simulations, but we feel that picture as a whole may not be satisfying yet.

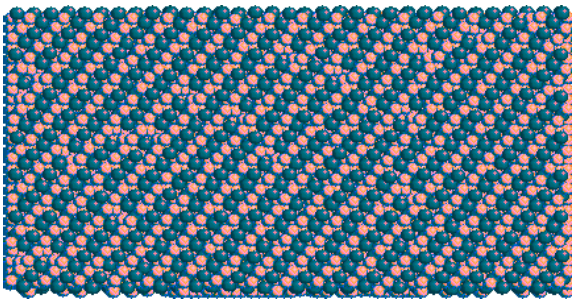

elastic: $u_p = 4.5v_0$

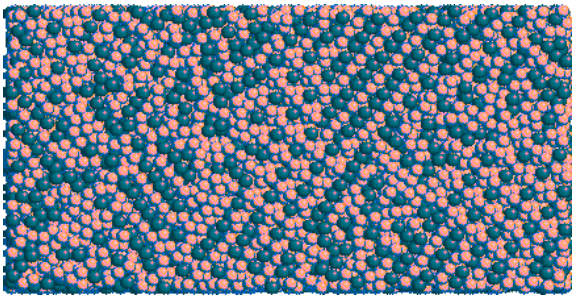

elastic-plastic: $u_p = 5.5v_0$

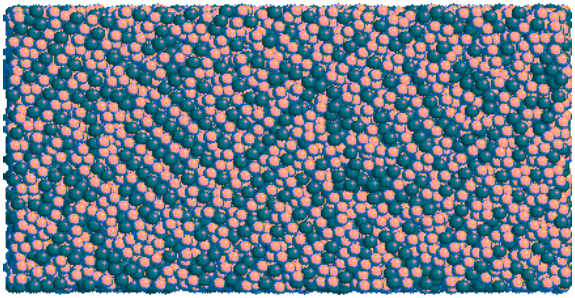

elastic-plastic: $u_p = 6.0v_0$

**Figure 4.13:** Longitudinal cuts through the central part of a Laves crystals after shocking at the given $u_p$.

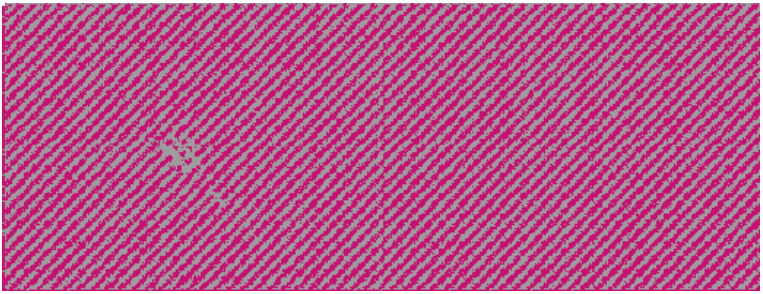

elastic: $u_p = 4.5v_0$

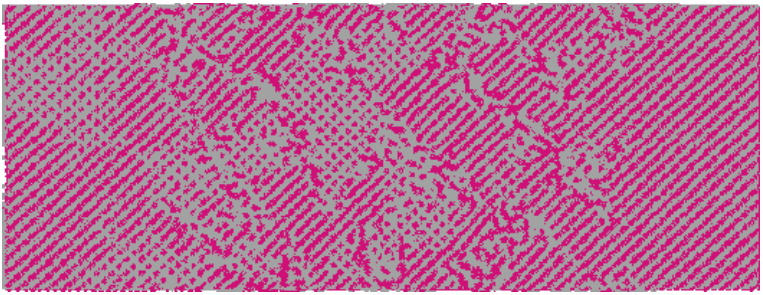

elastic-plastic: $u_p = 5.5v_0$

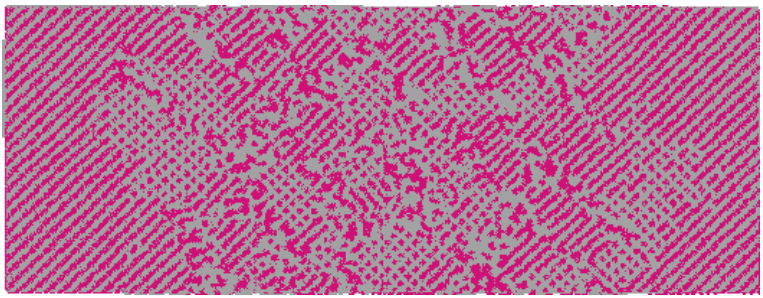

elastic-plastic: $u_p = 6.0v_0$

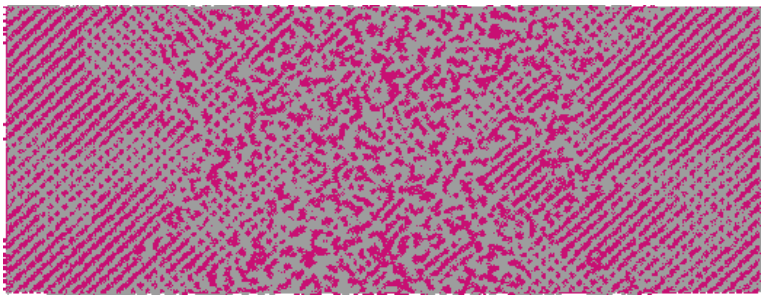

plastic: $u_p = 7.0v_0$

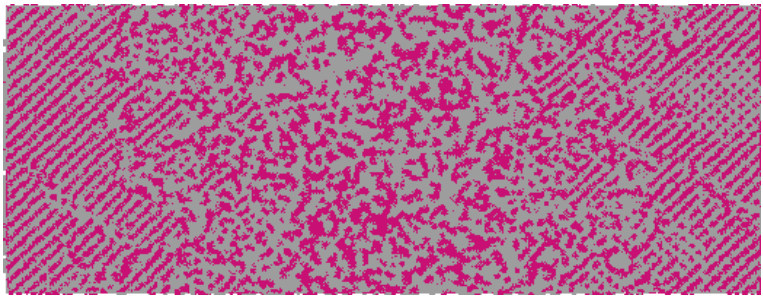

plastic: $u_p = 9.0v_0$

**Figure 4.14:** Longitudinal cuts through the whole quenched Laves crystals after shocking at the given $u_p$.

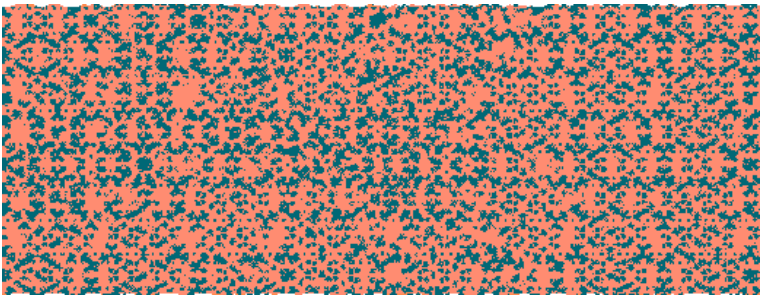

quasi-elastic: $u_p = 3.5v_0$

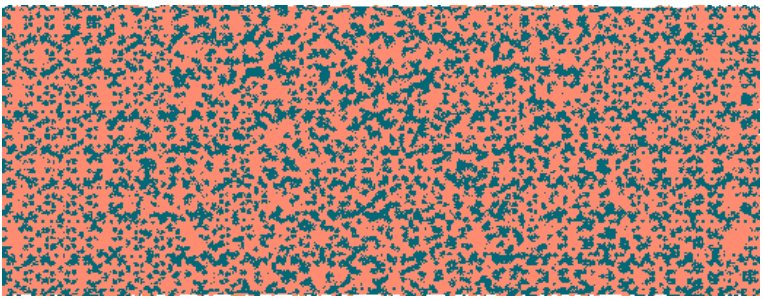

elastic-plastic: $u_p = 5.0v_0$

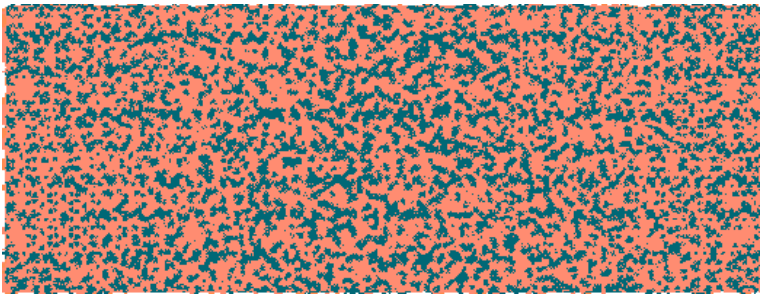

elastic-plastic: $u_p = 6.0v_0$

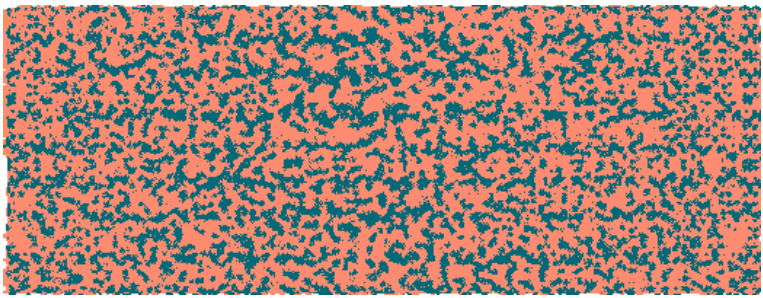

plastic: $u_p = 7.0v_0$

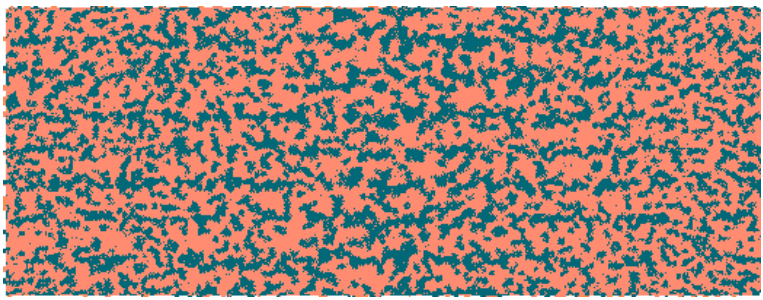

plastic: $u_p = 9.0v_0$

**Figure 4.15:** Longitudinal cuts through the quenched BI quasicrystals after shocking at the given $u_p$.

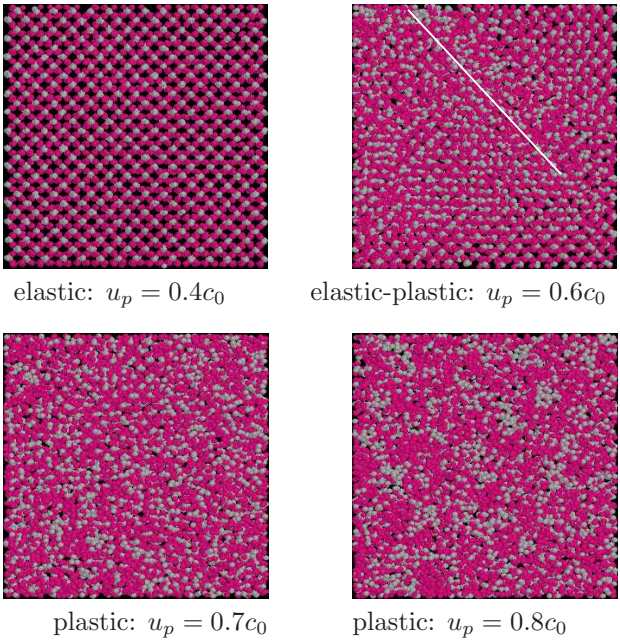


**Figure 4.16:** Transverse cut through the Laves crystals after shocking at the given $u_p$. The white line indicates one of the defect bands.

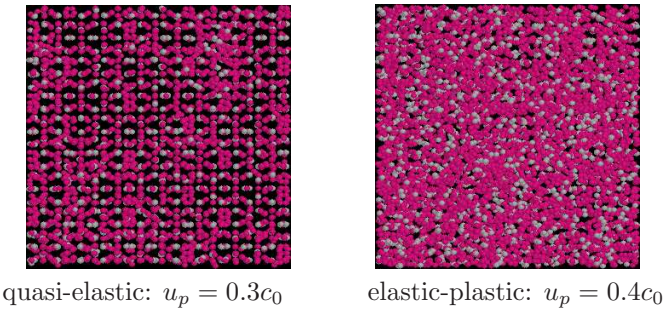


**Figure 4.17:** Transverse cut through the TI quasicrystals after shocking at the given $u_p$.

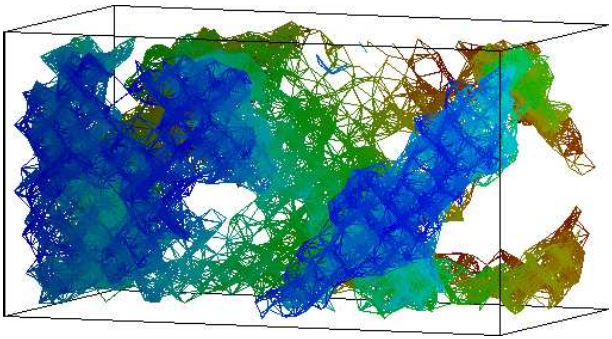

**Figure 4.18:** Broken $AA$ bonds in a Laves crystal after shocking at $u_p = 5.5v_0$. The colors code the depth. Broken $BB$ bonds and newly created bonds give similar pictures.

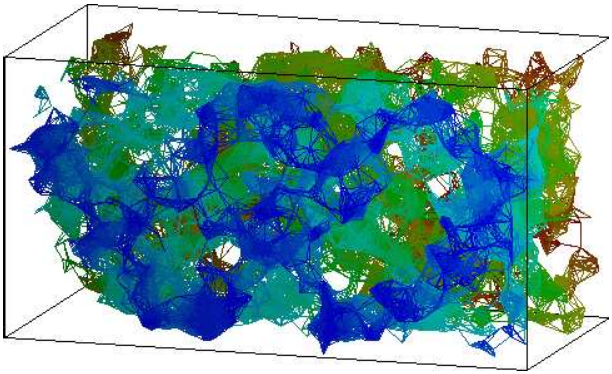

**Figure 4.19:** Broken $AA$ bonds in a TI quasicrystal after shocking at $u_p = 5.0v_0$. The colors code the depth. Broken $BB$ bonds and newly created bonds give similar pictures.

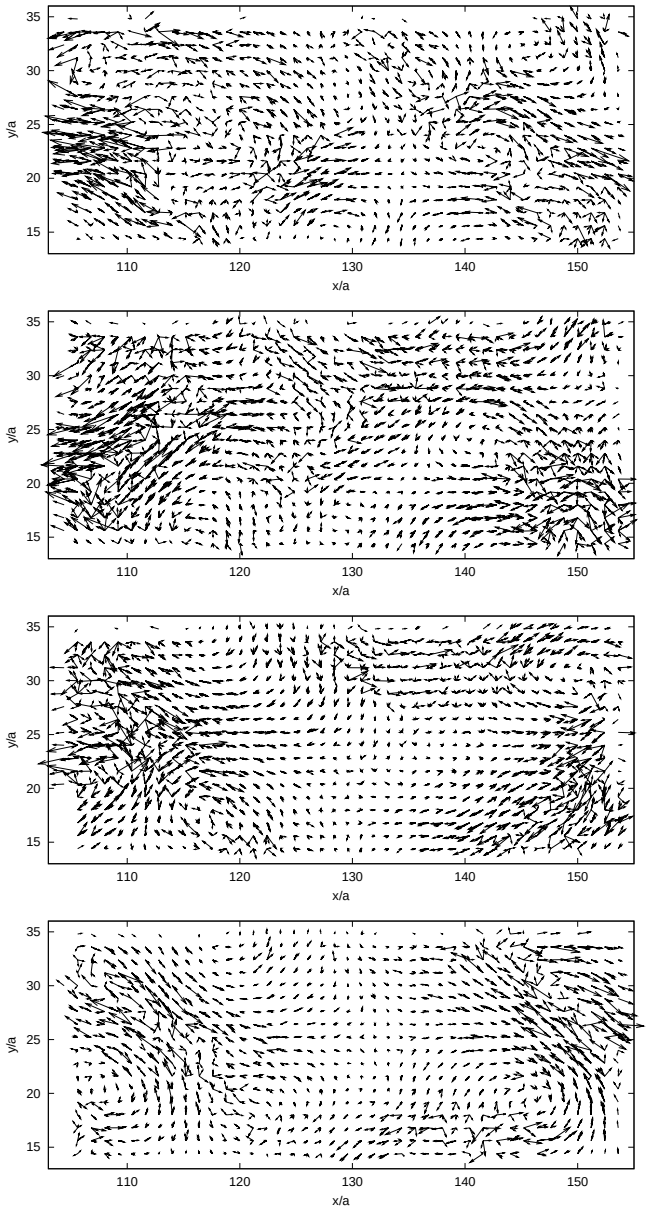


**Figure 4.20:** In-situ displacement field of a Laves crystal after shocking at $u_p = 5.5v_0$. Each slice has a thickness of $6a$.

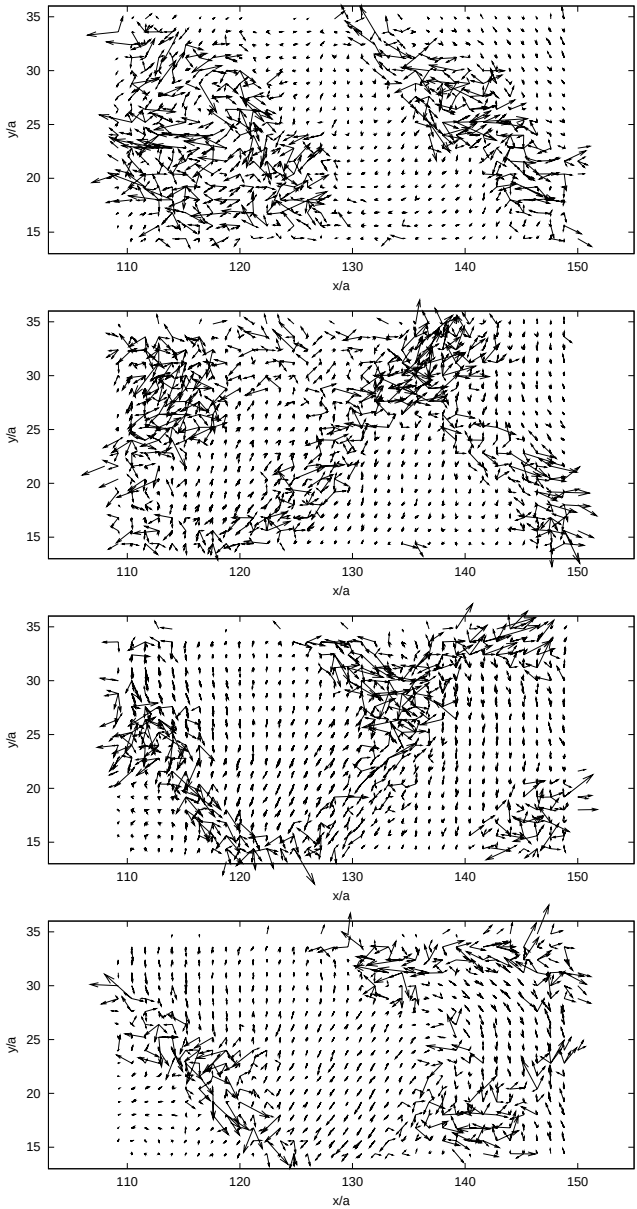


**Figure 4.21:** Displacement field of a quenched Laves crystal after shocking at $u_p = 5.5v_0$. Each slice has a thickness of $6a$.

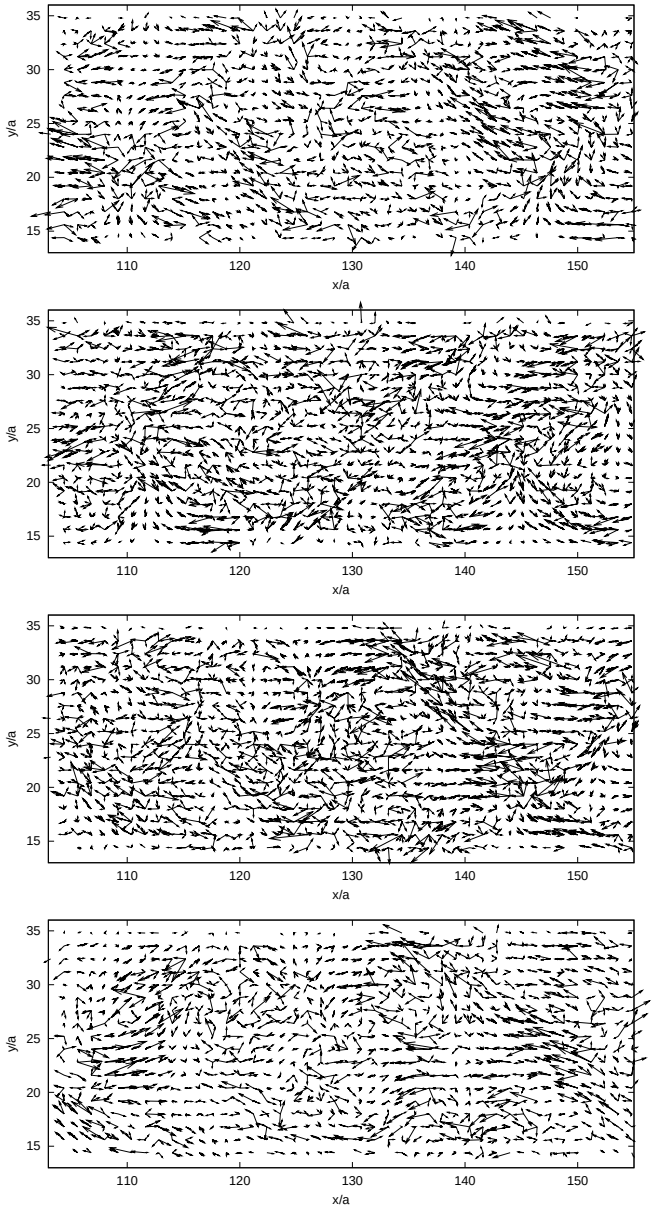


**Figure 4.22:** In-situ displacement field of a BI quasicrystal after shocking at $u_p = 5.0v_0$. Each slice has a thickness of $6a$.

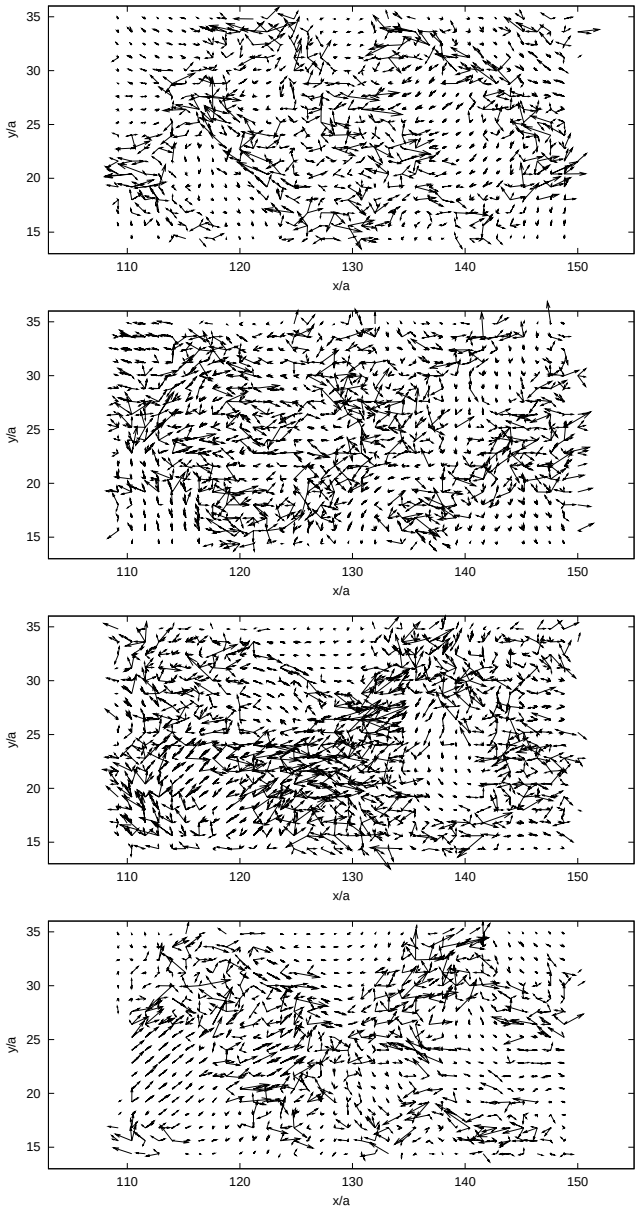


**Figure 4.23:** Displacement field of a quenched BI quasicrystal after shocking at $u_p = 5.0v_0$. Each slice has a thickness of $6a$.

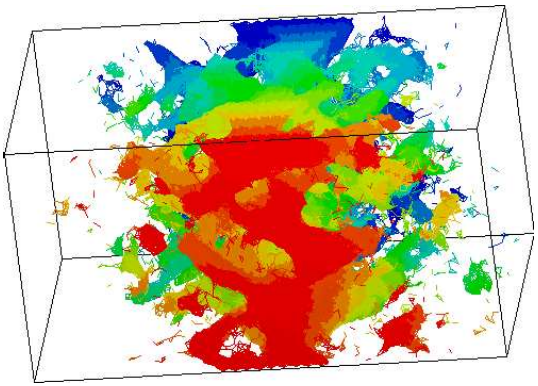

**Figure 4.24:** Locations of zero displacement. Laves crystal shocked at $u_p = 5.5v_0$. The colors code the depth.

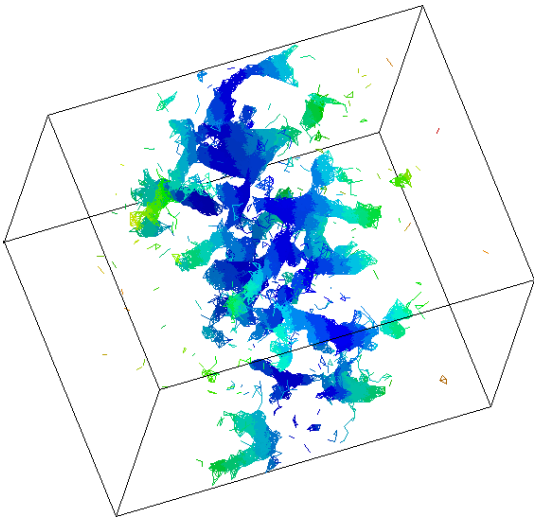

**Figure 4.25:** Locations of zero displacement. Laves crystal shocked at $u_p = 6.0v_0$. The colors code the distance to the initial collision plane.

Chapter 5

# Materials with Dzugutov Potential Interactions under Heavy Load: I. Shock Waves

## 5.1 Overview

The influence of shock waves on the bcc ground state, the metastable $\sigma$-phase, and quasicrystal structures of the Dzugutov potential [49] has been studied as a model of a monatomic three-dimensional quasicrystal. In general, a phase transition is observed to the well-known high-pressure fcc- or hcp-phases. The details of the phase transition and the perfection of the created phases depend on the orientation of the shock wave propagation direction with respect to the symmetry axes. The transition procedure will be described in detail.
Special phenomena occur for shock waves in the bcc-phase along the three-fold axis: An intermediate hexagonal $\omega$-phase and soliton-like excitations are observed. These results will be treated in Chap. 6.
The present chapter will end with the results obtained for an amorphous structure supplied with the Dzugutov potential. No crystallization takes place in this case.

## 5.2 Introduction

The action of shock waves has been explored in monatomic crystals to some depth [72, 238], and a first understanding of the basic processes has emerged [95]. The generation of partial dislocations and stacking fault type defects in fcc crystals could be clarified [206, 187]. Results for the plasticity of other structures, like bcc-iron for example, are also available now [117].
The purpose of this study was to find out whether monatomic quasicrystals behave different than crystalline materials if they are penetrated by shock waves.

Binary quasicrystals have been treated in the previous chapter. From a fundamental point of view it is more interesting, however, to study models as simple as possible, i. e. monatomic quasicrystals. But the number of such models is rather limited if generic interactions are favored. The crucial point is the packing density. There is the unit sphere packing model of Henley [84] with a density of 0.6288, still worse than the random close packing at 0.6366. Treated as a quasicrystal with Lennard-Jones interactions, the structure is metastable only up to 10% of the melting temperature of the ground-state fcc crystal [162, 40]. It is still the only promising monatomic icosahedral quasicrystal model known to us. Henley's twelve-fold site model [84] has a much lower packing density and so is even less stable. Other models are layered quasicrystalline which are periodic in one direction. The decagonal model of Cockayne and Mihalkovič [27] has a packing density of 0.6953, higher than the icosahedral model and larger even than bcc. But it also transforms into fcc upon heating if the atoms interact via Lennard-Jones potentials.
Finally there is a dodecagonal quasicrystal model with Dzugutov potential interactions. As described in Sec. 3.4.3 the Dzugutov potential has a bcc structure as its ground state, and the $\sigma$-phase and a quasicrystalline phase are metastable. At high pressure and low temperature a phase transition to close-packed fcc- or hcp-phases occurs. Upon heating at low pressure bcc, the $\sigma$-phase and the quasicrystal phases are stable up to rather similar melting temperatures. Thus we have a model with promising properties for shock wave simulations.
The simulations of monatomic models are being described in two parts: Here we present the results of shock wave simulations in different structures stable with Dzugutov interactions. In the next chapter we concentrate on the phenomenon of solitary waves observed especially in the bcc structure shocked along the three-fold axis and discuss in detail the hexagonal $\omega$-phase [218], a typical product of a bcc-lattice instability.

## 5.3 Generation of the shock waves and simulation setup

### 5.3.1 Orientation of the samples

For the simulation of shock waves it is necessary to apply periodic boundary conditions. Otherwise the pressure from the shock wave leads to a rapid transversal disintegration. The direction of the shock wave has to be parallel to one of the boundary axes, for example the $x$-axis. This limits the possible (quasi)-crystalline directions along which the shock wave can travel in the simulations. The quasicrystal, especially, has to be replaced by an orthorhombic approximant.

Shock waves have been studied in the bcc-phase along the four-, three-, and two-fold axes where they are straightforward to implement. Shock waves in the square-triangle quasicrystal have been studied along the periodic axis and in the quasiperiodic plane. Due to the high twelve-fold symmetry (space-group $12_6/mnm$) the quasicrystal is expected to be elastically isotropic in the plane, and the approximant should not deviate too much from isotropy. Shock waves along different in-plane directions should therefore give similar results. The $\sigma$-phase has space-group symmetry $4_2/mnm$, which indicates that for an ordinary, nearly cubic unit cell with 60 atoms the coordinate axes are parallel to the four-fold axis and to glide planes $n$, and the diagonals are parallel to mirror planes $m$. An in-plane diagonal tetragonal unit cell with 30 atoms is also possible with the four-fold axis and the $m$-planes parallel to the coordinate axis. The aspect ratio of these two unit cell lengths in the plane and along the $z$-direction is such that it is possible to construct out-of-plane diagonal cubic boxes with only minor distortions. The samples are rotated by 45 degrees towards the $z$-axis. In summary we have studied shock waves in the $\sigma$-phase along the four-fold axis, along the $n$- and $m$-directions, and along orientations at 45 degree between the four-fold direction and $n$ and $m$, respectively. The directions are denoted by 0, $n90$, $m90$, $n45$ and $m45$. The corresponding Miller indices are [100], [001] or [010], [011], [201] or [210], and [$\sqrt{8}$11].

### 5.3.2 Preparation of the samples and simulation details

The simulations were carried out as usual: for the shock simulations an NVE ensemble was used. Equilibrations were performed with the NVT-Nosé-Hoover and NPT-Andersen ensemble.
The sizes of the samples depend on the structures and orientations. Therefore they are not listed in detail. For most of the simulations the sample size was about $20 \times 20 \times 100a^3$. The samples contained 40,000 atoms approximately. To study the influence of the size of the samples and the propagation time of the shock wave on the results longer (200, 300 and $600a$ long with up to 250,000 atoms) and thicker samples ($40 \times 40 \times 300a^3$ with 500,000 atoms) have also been analyzed. To apply periodic boundary conditions the perfect dodecagonal quasicrystal is replaced by an orthorhombic approximant. The principial results are found to be independent of the sample sizes. There may be differences in the details, but there were no differences for example in the shock wave propagation velocities or in the phase transitions.
Before the simulation starts the samples are equilibrated for a time interval of $\Delta t = 10t_0$ at a temperature of $kT = 0.001\epsilon$ and a pressure of $P = 0.01P_0$. If the simulations are carried out at elevated temperatures, the samples are equilibrated again at the desired temperature.
To generate the shock waves we have applied the momentum mirror method. Tests have shown that the results are equivalent to the simulation with the symmetric impact method (except for the case of solitary waves in arbitrary directions treated in Sec. 6.4.5).

### 5.3.3 Analysis tools for the shocked structures

If the shocked state is monocrystalline as for bcc shocked along the four-fold direction at low piston velocities then the analysis can be carried out directly by visual inspection of the structures. The stacking sequence can be derived from a projection of the atoms perpendicular to the distinguished threefold axis: A zigzag pattern determines hcp, a diagonal sequence fcc. In general we find a mixture of both.
Usually the shocked crystals are very defective, the lattice rows and planes are warped and rotated, twins or several crystallites may exist. A direct distinction between fcc or hcp or more complicated stackings

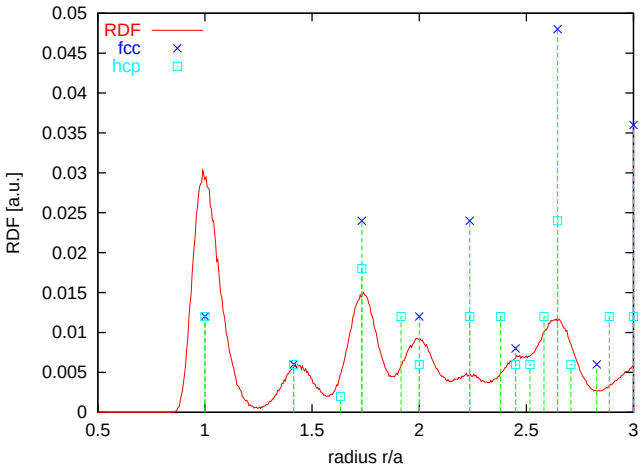


**Figure 5.1:** Typical radial distribution function. The spikes indicate the neighbor shells for ideal fcc (×) and hcp (□) crystals. Obviously, these cases cannot be distinguished in the simulation result.

is no longer possible. The radial distribution function (RDF) tells us only that a close-packed phase has been generated (Fig. 5.1).
But if the angular distribution function (ADF) is computed for nearest neighbor atoms, then it is possible to distinguish fcc and hcp (Fig. 5.2) since hcp permits an additional maximum between 140 and 160 degree (the angle between the apex atoms and a base atom of two face-connected tetrahedra). In most cases a mixture of fcc, hcp and other stacking sequences is found.

## 5.4 Results

We will start with the elastic properties of the materials since the elastic waves form the limiting case of very weak shock waves if the strength of the material prohibits the creation of defects. The next step is the discussion of a $u_s$-$u_p$-Hugoniot diagram which permits a classification and characterization of the different shock wave regimes. Following is a presentation of the phase transformation results grouped together with respect to similar phenomena.

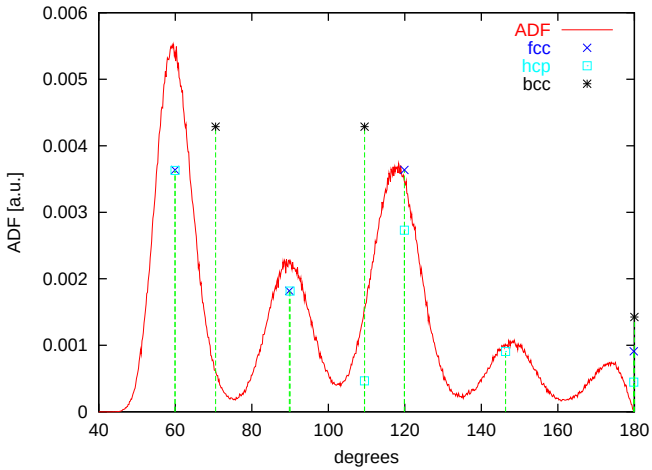


**Figure 5.2:** Typical angular distribution function. The spikes denote the angles in ideal fcc ($\times$), hcp ($\square$), and bcc ($*$) respectively. The simulation result does not fit to the bcc maxima, but to fcc or hcp. A distinction between the latter two is possible since the maximum between 140 and 160 degrees is only present in hcp. The conclusion is that the sample under consideration is preferably hcp stacked. Cases without a maximum between 140 and 160 degrees have also been observed.

**Table 5.1:** Elastic properties for the bcc-phase. The first column gives the Miller indices, the second the uniaxial elastic module and the third the velocity of the (quasi-)longitudinal wave. The bcc crystals are obviously anisotropic.

| direction | $F[P_0/m]$ | $c[v_0]$ |
|---|---|---|
| [100] | 287.0 | 16.6 |
| [110] | 387.0 | 19.3 |
| [112] | 389.4 | 19.4 |
| [111] | 424.8 | 20.2 |

### 5.4.1 Elastic properties and sound velocities

Dodecagonal quasicrystals behave elastically isotropic with respect to the quasicrystalline plane, but not with respect to the periodic axis, similar to hexagonal crystals. The $\sigma$-phase is anisotropic in the square-triangle-plane since it has only tetragonal symmetry. The bcc crystals have cubic symmetry. The elastic constants determined by quasistatic uniaxial deformations[1] are presented in Tabs. 5.1 and 5.2. If the piston wave velocity $u_p$ goes to zero, the shock wave velocity tends towards the velocity of an elastic sound wave.
It is important to note that the highest velocities of sound occur along directions perpendicular to the thinnest crystals planes equivalently to parallel to the densest atomic rows. This are the directions where the solitary waves (See Chap. 6) are most prominent.

### 5.4.2 The Hugoniot relation: $u_s$ *vs.* $u_p$

In the case of shock waves in two-atomic Laves crystals and quasicrystals three regimes of different behavior of the shocked materials have been observed. The same is true here, although at a first glance the Hugoniot diagram (Fig. 5.3) looks different: There seem to be only two ranges, separated at about $u_p = 4v_0$, where $v_0$ is the unit of velocity.

[1] The elastic compression wave is longitudinal only along special symmetry directions. The wave which becomes longitudinal in the long-range limit along other directions is called quasi-longitudinal.

**Table 5.2:** Elastic properties of the tcp-phases. The first column gives the Miller indices, the second and fourth the uniaxial elastic module and the third and fifth the velocity of the (quasi-)longitudinal wave for quasicrystals and the $\sigma$-phase, respectively. The first three rows contain the results for the perfect samples, the last two rows list the results for samples which have been distorted to permit periodic boundary conditions parallel to the 45 degree direction. A comparison of the second and third row and the fourth and fifth row respectively, shows that the quasicrystal is isotropic within the error margins whereas the $\sigma$-phase possesses a strong anisotropy of the order of 6%.

| | quasicrystal | | $\sigma$-phase | |
|---|---|---|---|---|
| direction | $F[P_0/m]$ | $c[v_0]$ | $F[P_0/m]$ | $c[v_0]$ |
| [100] | 298.4 | 16.8 | 299.2 | 16.8 |
| [010] or [001] | 179.2 | 13.0 | 180.4 | 13.1 |
| [011] | 177.0 | 13.0 | 203.0 | 13.9 |
| [201] or [210] | 216.8 | 14.3 | 248.0 | 15.4 |
| $[\sqrt{8}11]$ | 200.6 | 13.8 | 208.2 | 14.0 |

The reason is that the elastic first range is very small since the transition from bcc and $\sigma$-phase takes place at about $P = 5.5 - 6P_0$, and this pressure is reached at $u_p = 0.7v_0$ ($0.03 - 0.05c_x$, if $c_x$ is the uniaxial velocity of sound of structure $x$)[2] already. Furthermore no retardation effect is observed. The elastic wave velocity is hard to determine since no sharp wave front exists. Therefore it is not included in the diagram.
In the range between $u_p = 0.7v_0$ and $u_p = 3-4v_0$ ($\approx 0.2-0.25u_p/c_x$) we observe steady or unsteady shock waves, depending on the orientation of the samples and the character of the phase transition. In this range the shock speed of the uniaxial compression wave is more or less constant whereas the velocity of the slower transformation wave grows rapidly (Figs. 5.3 and 5.4).
Above $u_p = 3 - 4v_0$ ($\approx 0.2 - 0.25u_p/c_x$) the velocities of both waves approach each other. This range will be called the overdriven regime. If the transition is sharp, as in the case of bcc shocked along the four-fold direction, a distinction between both waves does not exist any longer. In the other cases, especially for bcc shocked in three-fold or two-fold direction two "transformation" wave fronts are plotted: A first one which indicates that the initial phase starts to be destroyed and a high-defect phase is formed, and a second one which indicates the transition to a low-defect close-packed phase. There is a difference between the two velocities since it takes a finite time to reorder the atoms and to complete the phase transition. It cannot be guaranteed that this process is finished during simulation even if the samples are an order of magnitude longer. Furthermore there are hints that the second transition may be an artefact of the momentum mirror which it forces the lattice planes to be parallel to it and thus enhances the possibility to form single crystals.
In the monatomic system a clear distinction exists between the overdriven range and the middle range, in contrast to what has been observed in the simulations of diatomic materials.
In the middle range a metastable phase is formed which is related to solitary waves observed in the overdriven range. These effects lead to additional wave fronts and wave velocities $u_s$ and may complicate the analysis of the results. For simplicity, in Fig. 5.4 the wave crests related to the metastable phase and the solitary wave trains are omitted.

[2]To simplify the comparison the piston velocities are given in reduced units $v_0$ and scaled by the velocity of sound of the structure under consideration if necessary.

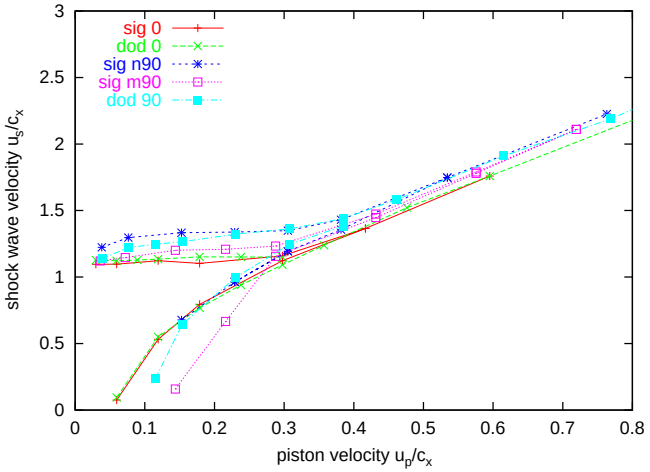


**Figure 5.3:** Hugoniot diagram for $\sigma$-phase and quasicrystal simulations. The axes are scaled with the velocities of sound.

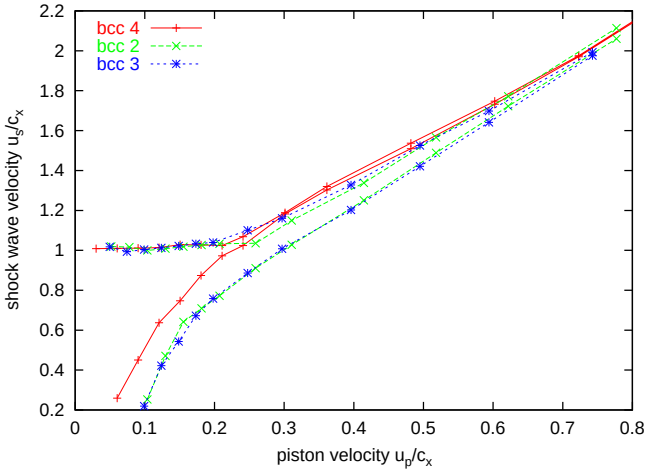


**Figure 5.4:** Hugoniot diagram for the simulations of the bcc crystal. The axes are scaled with the velocities of sound.

### 5.4.3 Description of the structural results

Since a lot of structures and orientations have been studied to get a general overview of the possible mechanisms, it is not possible to deal with all the cases in detail and to describe the results in dependency of the piston velocity $u_p$. Instead we will concentrate on a few representative cases, describe them in detail – especially the dependency on $u_p$ – and add remarks about other structures and orientations where appropriate. We will concentrate on the middle range, since in the elastic range no defects are created and in the overdriven range the energy stored in the structure is so high that no good crystals are created during simulation.
The first case are shock waves in bcc along the four-fold direction. This is the only case where an abrupt transition to a perfect close-packed crystal takes place.
The second case are all the other structures and orientations. The initial structure is broken, but it takes time to generate a close-packed crystal with a small number of defects.
The third case are shock waves in bcc along the three-fold direction. Two closely related special phenomena are observed: an intermediate phase and solitary waves. These phenomena will be presented in more detail in Chap. 6. Solitary waves occur also along other directions and in other structures but they are not stable there.
The last case is an amorphous structure which has been produced by cooling a molten bcc crystal. Since there is no liquid phase for the Dzugutov potential at ambient pressures [163], we had to prepare the liquid by heating at constant volume, cool it down to $kT = 0$, and expand it to $P = 0$.

### 5.4.4 The four-fold direction

The phase transition from bcc to close-packed phases for shock waves along the four-fold direction is very special. It is the only case where a perfect crystal may be found after the transition and an atomically flat interface between bcc and fcc or hcp is observed. Consequently the pressure profile is constant and steady and shows a sharp jump at the interface between bcc and the close-packed phase.
As an example we present the results for $u_p = 4v_0$ ($u_p/c_4 = 0.24$, middle range). Fig. 5.5 shows the flat interface. The orientation of the

close-packed layers is such that a three-fold axis is generated parallel to the shock direction. A two-fold axis is parallel to the face diagonal (Fig. 5.6, left). This orientation is none of the well-known martensitic bcc-fcc orientation relationships. The stacking sequence of the layers is more or less random (Fig. 5.7 and Fig. 5.8), but sometimes rather pure fcc or hcp sequences occur. In the right part of figure 5.6 we display a case of twinning which is a low-energy defect. Due to the periodic boundary conditions there have to be two interfaces: one at $y = 8a$ and one at $y = 18a$. We have found that the newly generated close-packed phase may change several times between twined and monocrystalline.
If the piston velocity enters the overdriven region then the transformed phase is no longer monocrystalline. Several crystallites are created, and at about $u_p = 8v_0$ the defect density has grown so large that the sample cannot be distinguished from a disordered or amorphous structure.

### 5.4.5 The other directions and structures

Shock waves along the two- and three-fold direction in bcc, and in the $\sigma$-phase and the quasicrystal along any direction never lead to a direct transition to the close-packed phase. Although the statistics and the details may differ, the overall pattern of the phase transition is similar. Therefore we will discuss these cases summarily.
The general scenery is the following: The initial structure is heavily distorted or destroyed at first, but finally the systems transforms into the close-packed phase. Therefore we can distinguish two wave fronts since their velocity is not the same at least at the time scale of the present simulations (Fig. 5.4).

#### Shock waves in bcc along the two-fold and three-fold direction

There are two alternating paths which may however be mixed up: transverse shift of the atomic layers (Fig. 5.7) or rotation of the atomic layers around an axis parallel to the shock direction (Fig. 5.8). It is remarkable that there are only kinks in the atomic chains parallel to the shock wave direction, but no disruption. There are also no point-like defects or local alterations of the structure. The whole motion of the atoms appears to be well correlated!

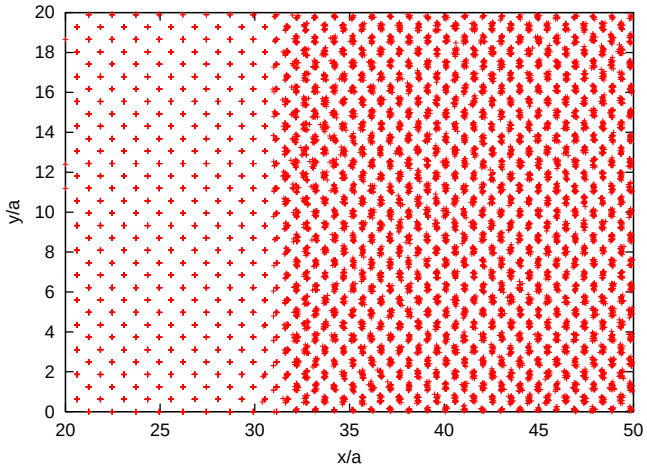


**Figure 5.5:** Longitudinal projection of a bcc crystal shocked along the four-fold direction ($u_p = 4v_0$). The shock wave moves to the left, the mirror is at the right side at $x = 100a$. The interface between initial bcc and final fcc is flat.

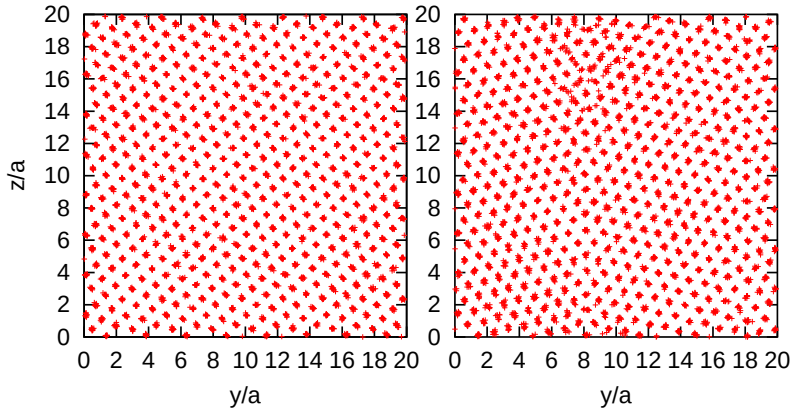


**Figure 5.6:** Transverse cuts through a bcc crystal shocked along the four-fold direction ($u_p = 4v_0$). The shock front is currently at $x = 31a$ and moves towards $x = 0$ (See Fig. 5.5). Left: slice between $x = 50a$ and $x = 60a$, right: slice between $x = 75a$ and $x = 85a$.

The shift type transformation usually starts with a sudden kink in the atomic chains parallel to the shock direction, preferably parallel to one of the transverse coordinate directions (Fig. 5.7). Other kinks may occur along the same or other directions. Between the kinks the atomic chains bend smoothly. At the end of the sample, close to the mirror, an almost perfect close-packed phase is generated. But now the interface with the distorted bcc-phase is not atomically flat as in the case of shock waves along the four-fold axis in bcc. A change of the stacking sequence and twinning is also visible.
The rotation type transformation is not so easy to represent in projection (Fig. 5.8). It usually is recognized by its Moiré pattern which indicates that the density of the points which represent the atoms changes back and forth between periodic and almost densely filled. In contrast to the previous case there are most often no sharp kinks but a continuous local variation of the rotation angle. At the end of the sample, close to the mirror, an almost perfect close-packed phase is generated as in the other case.
The effect of higher piston velocity $u_p$ is similar to the case of shock waves along the four-fold direction of bcc: In the overdriven region the generated crystals become polycrystalline and around 6 to $8v_0$ they can no longer be distinguished from an amorphous structure.

**Shock waves in the tcp-phases**

The final state of shock waves in the $\sigma$-phase and the quasicrystals for all orientations is a close-packed phase with clearly defined layers perpendicular to the shock direction, but with several crystallites in this plane. Compared to the bcc case, the close-packed crystal has no preferred direction with respect to the coordinate directions, and it contains many defects and extended disorder within the plane.
The details of the transition differ for the different phases and orientations:

1. $\sigma$-phase and quasicrystal, shock wave perpendicular to the basic layers (0-orientation): Instead of kinks or bending, a destruction of the structure and a periodic modulation along the shock wave direction is observed. A polycrystalline close-packed phase is generated with random orientations of the small crystallites. The sample finally evolves into the structure described above.

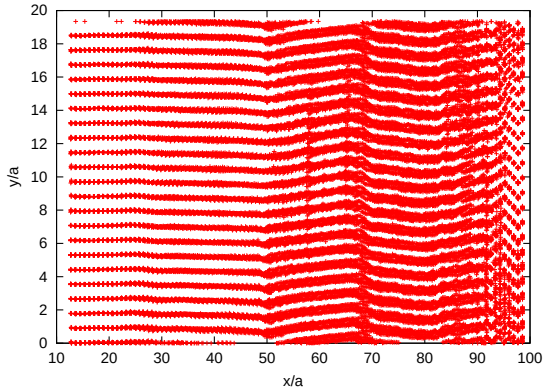


**Figure 5.7:** Longitudinal projection of a bcc crystal shocked along the two-fold direction ($u_p = 2v_0$). This is an example where the lattice planes are shifted perpendicular to the shock wave direction. The shock wave moves to the left, the mirror is at the right side. A beginning ABABC stacking sequence is visible around $x/a = 97$.

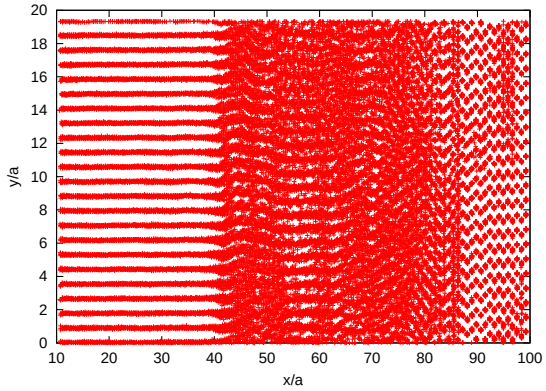


**Figure 5.8:** Longitudinal projection of a bcc crystal shocked along the three-fold direction ($u_p = 3v_0$). This is an example where the lattice planes are rotated perpendicular to the shock wave direction. The shock wave moves to the left, the mirror is at the right side. A beginning ABABABABABCBCAB stacking sequence is visible between $x/a = 87$ and $x/a = 100$.

2. $\sigma$-phase, $m45$- and $m90$-orientation, and quasicrystal (90-orientation), e.g. shock wave parallel to the basic layers: The transition is similar to the case before, but without the modulation parallel to the shock wave direction.

3. $\sigma$-phase, $n90$-orientation: The structure observed after the transition does not consist of randomly oriented crystallites but periodic bands are running diagonally through the sample at 45 degree with respect to the basic layers. The material is in a transitional state to a close-packed phase. At the end it evolves into the structure described above.

4. $\sigma$-phase, $n45$-orientation: The transition is similar to the case before, but a transient state is generated. First the initial phase is sheared homogeneously perpendicular to the shock wave direction, then after some time kinks and bands are generated as in the case before. The transient state is most prominent at low piston velocities, shrinks continuously and vanishes in the overdriven region. The interface with bcc is atomically flat.

**Flipped configurations in the tcp-phases**

A phenomenon which is called "phason flip" in quasicrystals occurs in the tcp structures shocked along a direction which lies in the basic layer. For simplicity the phason flips can be regarded as tile rearrangements and replacements which are possible in many non-trivial tilings.
Figure 5.9 shows an example of new rhombi and rearranged tiles in the $\sigma$-phase shocked in $m90$-orientation. The orientations are always the ones found in the figure. Others are not possible for geometric reasons. In samples shocked in the $n90$-orientation the rhombi are oriented with their long diagonal parallel to the coordinate axis. In the quasicrystal both orientations are observed. The three-fold symmetric hexagon has also been seen in some occasions, but the two-fold symmetric hexagon never shows up, because it is very unstable. The atomic rearrangements of a flip have been described in detail by Roth [172]. All the atoms along a row perpendicular to the shock direction change from a one-dimensional configuration where the atoms in the basic layer are represented by a dotted ring in Figs. 3.8 - 3.10 to a staggered configuration represented by a open and nearby close circle, or vice versa.

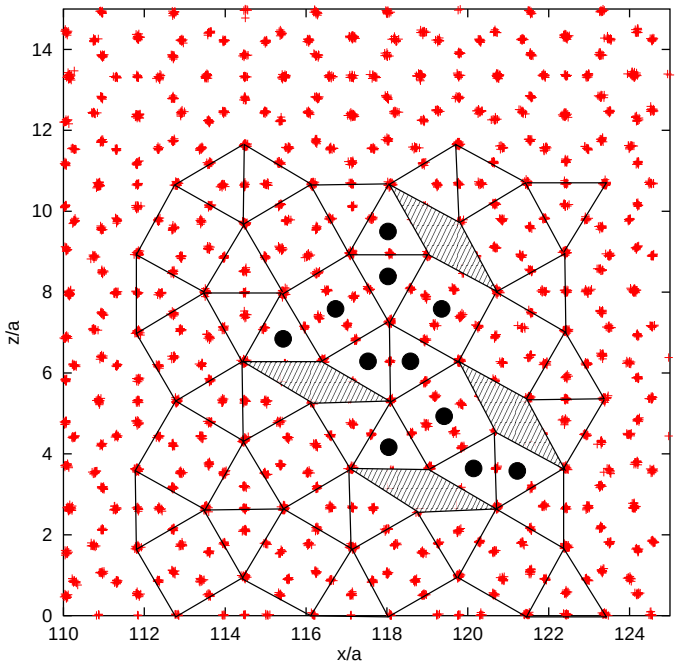


**Figure 5.9:** Part of a $\sigma$-phase sample shocked in $m90$-orientation, $u_p = 2v_0$. A part of the tiling has been redrawn. Shaded are the newly generated rhombi. The black dots mark the squares and triangles which have been flipped. The shock wave moved from the right to the left.

The tiles themselves are abstract objects which have no physical meaning. Therefore it is not surprising that flips from one-dimensional to staggered configurations are observed which lead to non-tilable regions.

### 5.4.6 Special phenomena for shock waves along the three-fold direction of bcc

If shock waves are studied in bcc along the three-fold direction a new intermediate phase and solitary waves are observed. The intermediate phase has been identified as the hexagonal two-layer $\omega$-phase [218]. It

is the crystal structure of the high-temperature superconductor $AlB_2$. Chapter 6 is devoted to the detailed description of the two closely related phenomena.

### 5.4.7 Results for an amorphous structure

The amorphous structure generated from the liquid has a RDF which differs from an ordinary monoatomic amorphous structure generated with Lennard-Jones potentials for example. The difference is caused by the maximum of the Dzugutov potential: The RDF shows the well-known behavior of a supercooled liquid with a first maximum for nearest neighbors and a double maximum for next-nearest neighbors, but the first of the two next-nearest neighbor peaks is extremely sharp if compared with what is usually observed. The third maximum seems to be enhanced also.

The Hugoniot curve (Fig. 5.10) shows that at low piston velocities the velocity of the wave front at half height ($amo_c$) is almost constant. The distance between the bottom and the place where the wave reaches a constant value grows and the difference is most prominent around $u_p/c_a < 0.1$. If the piston velocity is increased the ascent of the wave gets sharper and sharper until the difference between the velocities vanishes in the overdriven regime. The width of the transition region is of the order 5 to 10 atom distances $a$.

In the RDF we notice a rather sharp transition at the beginning of the overdriven regime at about $u_p/c_a < 0.4$ (Fig. 5.11). At low piston velocities the first maximum of the RDF lies around $1.05a$, then it moves to $0.85a$ and broadens slightly. The most significant change occurs to the sharp sub-peak of the second maximum: It stays at its place, but broadens from a width of $0.1a$ to $0.5a$. The other sub-peak vanishes completely and the third maximum moves by $0.3a$ and doubles its width. At the highest piston velocities the RDF looks like one of an ordinary monatomic liquid.

The ADF possesses two broad maxima at an angle of 60 degree and at 112 degree. In the shocked samples these maxima shift continuously to 57 and 110 degrees respectively, if the piston velocity is increased.

The sharp transition indicates that the behavior of the material changes from glass-like to liquid-like if the piston velocity increases from weak shocks to overdriven shocks. The kinetic energy of the atoms is high

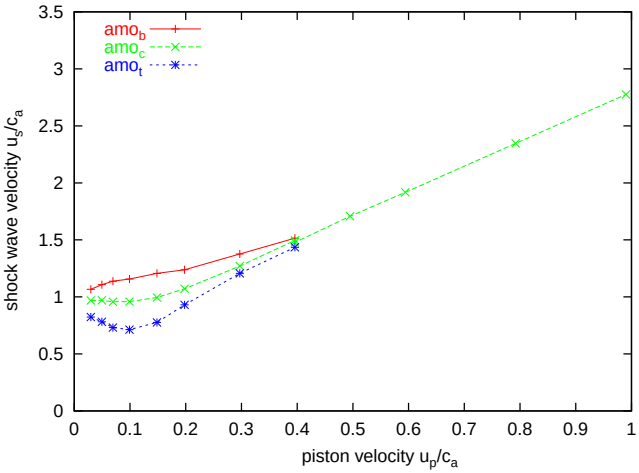


**Figure 5.10:** Hugoniot curve $u_s$ *vs.* $u_p$ for the amorphous structure. Plotted are the velocities at the bottom ($\text{amo}_b$), at half height ($\text{amo}_c$) and at the place where the hydrostatic pressure reaches a maximum ($\text{amo}_t$). In the overdriven region the distinction between these velocities vanishes, which means that we find sharp wave fronts.

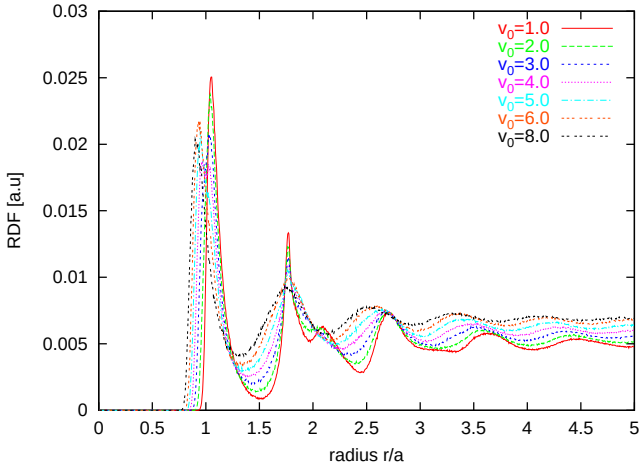


**Figure 5.11:** RDF of the amorphous sample for different $u_p$.

enough that the repulsive maximum of the Dzugutov potential no longer plays a role at the high piston velocities.
In contrast to all other samples studied in this chapter no transition to fcc is observed. This is already obvious from the RDF since no maximum or shoulder exists around the distances 1.25 and 1.55$a$. The ADF has no maxima at 90, 150, and 180 degrees. All together this proves that there are no square arrangements of atoms and no nuclei of a close-packed phase. A modulation of the density occurs only closely to the momentum mirror.
Compared to the shock waves in the ordered structures we find no crystallization. This indicates that it is easier to shift atomic layers collectively to generate a new structure than to crystallize an amorphous material.

## 5.5 Discussion

### 5.5.1 Comparison to shock wave simulations of iron

Kadau et al. have carried out molecular dynamics simulations of bcc iron single crystals [117,116,115,119]. Instead of a simple pair potential

they used EAM potentials especially adjusted to the properties of iron. Despite these differences their results and ours are in good qualitative agreement. There are several reasons for this observations: The phase diagrams of iron [21] and for the Dzugutov potential [162] are similar, i.e. both possess at low temperatures a low pressure bcc and a high pressure close-packed phase. Furthermore, if the elastic constants are computed for the Dzugutov potential and compared with the relative values $c_{11}/c_{44}$ and $c_{12}/c_{44}$ for iron [57] it is found that these values are closer in the diagrams (Fig. 2 of Every [57]) than to any other material. Due to the similarity of the phase diagram, the Hugoniot for iron (Kadau et al. [119], Fig. 4) and bcc with Dzugutov potentials (Fig. 5.4) is qualitatively similar. The results for the four-fold direction are also in good agreement, however we did not observe the compressed bcc inclusions (Kadau et al. [117], Fig. 1B). It is possible that they have been missed in our case since the $u_p$-interval of occurrence is rather small. Twinning is also prominent in our simulations (Fig. 5.6), and the growth of the crystallites with time (Kadau et al. [115]) has also been noticed. Another important coincidence are the solitary waves which occur for both interactions along the same three-fold direction.

There are also some notable differences: The pictures of structures generated by shock waves along the two- and three-fold axis [119] look similar at a first glance. Kadau et al. only remark that the grains in these situations are smaller than for the four-fold case. Furthermore a broad range of elastically compressed material is seen. The mechanism of phase transformation seems to be similar to the four-fold direction. But if one considers our Figs. 5.7 and 5.8 one finds a correlated transverse motion of lattice planes, i.e. a martensitic type of transformation[3]. The $\omega$-phase has not been reported for EAM-iron. At last we want to remark that there is a difference in the final structures: We do not find a Nishiyama-Wassermann relation between bcc and fcc or hcp,resp., but close-packed planes perpendicular to the shock direction if this is the

[3]In the interpretation of these results one has to be very careful if, for example, the coordination number is taken as an indication of the structure or defects since the material is compressed uniaxially and the ideal coordination numbers are no longer valid. If a radial criterion is used we find that a shift of the cutoff radius by less than a percent can change the picture completely since the atom shells of bcc and of the close-packed phase are rather broad and overlap partially which may pretend the presence of point defects (See Kadau et al. [119], Fig. 2).

four-fold axis. The EAM potential clearly favors a hcp-phase (Kadau et al. [119], Fig. 3), whereas we get a mixture of stackings of the close-packed layers. The reason for this difference is not obvious since the range of the EAM potential is similar to the range of the Dzugutov potential. We attribute the different behavior to the many-body part of EAM which is lacking for the pair potential. Therefore there is no difference in energy for ABA or ABC stacking for the Dzugutov potential whereas the EAM potential favors fcc-ABC.

### 5.5.2 Conclusions

We have presented detailed studies of shock waves in several structures that are stabilized by the Dzugutov potential. There are at least three major results: First, the Dzugutov potential which has been designed for a completely different purpose is suitable to study qualitative features of iron and probably of other bcc structures. It may even be possible to get to a semi-quantitative or quantitative agreement if the Dzugutov potential is modified by fitting it directly to the iron properties. A second major result is the generation of special defects in the tcp-phases which are equivalent to the phason flips in quasicrystals. This effect has been observed now on several occasions, here and in binary quasicrystals. Since the defects occur especially in the uniaxially compressed part of the sample it also represents evidence of the coupling between phononic and phasonic degrees of freedom [121] of a quasicrystal. Although we have not (yet) found evidence for extended defects like phason walls generated by shock waves we have observed the creation of point defects and phason-type flips. At last, we have presented simulations of a Dzugutov glass and found that no crystallization occurs which tells us that the pre-existing bcc- or tcp-order helps the structures in the phase transition and shows that the transition is a correlated phenomenon.

Chapter 6

# Materials with Dzugutov Potential Interactions under Heavy Load: II. The $\omega$-Phase and Solitary Waves

## 6.1 Overview

Molecular dynamics simulations show that shock waves in single crystals are frequently accompanied by solitary waves. In general the shock waves cause phase transformations to a close-packed phase. In addition, special phenomena occur if bcc is shocked along the three-fold direction: We have observed an intermediate phase which has been identified as the $\omega$-phase, and closely related non-steady solitary waves in the regime of overdriven shock waves.
The two phenomena are described in detail and compared to solitary waves in other materials. The conditions for solitary waves are discussed and we will try to provide a theoretical explanation.

## 6.2 Introduction

Since solitary waves have been observed very frequently and for different structures and interactions we decided to investigate this phenomenon in more detail [72, 119, 238].
Before we start we shortly argue why the exceptional wave features are referred to as solitary waves: they are not called solitons since the particle character of these waves has not been demonstrated. But they are denoted solitary waves since they occur as single maxima, moving through the undistorted or elastically compressed crystal. They show no dispersion, and their velocity depends on their height. Not everybody might agree with us since the solitary waves get damped, by virtue of

the small size, the discrete nature of the structure, temperature and other influences.

The first simulations of shock waves in fcc Lennard-Jones crystals where carried out along the four-fold direction [93, 101, 128] and yielded quite simple, steady profiles for all piston velocities. Thus it occurred as a surprise when complicated shock profiles, locked-in, and non-steady solitary wave trains where observed along the two-fold direction [72, 95]. Further examples of locked-in solitary wave observations include simulations by E. Bringa et al. [26] in fcc copper, by S. V. Zybin et al. [237,238] in a diamond structure and by V. V. Zhakhovskiĭ et al. [231, 233, 234, 235, 238] in fcc Lennard-Jones crystals. In all these cases an oscillatory behavior of the elastic wave preceding the plastic wave was observed.

Solitons are well-known from shock wave studies of one-dimensional models for a number of interactions [102]. They can be described as Korteweg-de-Vries or Toda solitons depending on the nonlinearity and strength of the interaction [97]. The one-dimensional solitons are caused by the lack of plasticity. The same happens in the three-dimensional simulations mentioned above if the shock strength is below the Hugoniot elastic limit. The solitary wave train is now locked into a steady oscillatory profile [95]. Actually, solitary wave peaks are still visible in the elastic-plastic regime and in the overdriven regime as the results by Germann et al. [72], Zybin [238] and Zhakhovskiĭ et al. [231, 233] show. In addition to the locked-in solitary waves there are non-steady waves [95, 71] visible in the *elastic-plastic* regime. The non-steady waves precede far ahead of the locked-in solitary waves. In Zybin [238] and Zhakhovskiĭ et al. [231,233]'s simulations they are not visible since these authors are averaging observables like stress and temperature in a frame moving with the steady wave profile.

The results presented here are about non-steady solitary waves in bcc along the three-fold axis in the *overdriven* regime. Such solitary waves have also been observed in bcc-iron along the three-fold direction by Kadau [119], and by the present author in a simple cubic structure along the four-fold direction.

We can demonstrate that the non-steady solitary waves are a supersonic continuation of a sub-sonic phase transformation which occurs in bcc only if shocked along the three-fold direction. The origin of the phase transformation is an instability with respect to uniaxial compres-

sion of the bcc structure interacting by the Dzugutov potential. The instability is related to the softening of a longitudinal phonon mode. If this mode has the ideal wave vector $\frac{2}{3}[111]$, every second and third plane in bcc collapses. The product is the two-layer hexagonal $\omega$-phase, the crystal structure of $AlB_2$ or $\omega$-CrTi [218]. If the wave vector of the phonon mode deviates from the ideal value, a modulated structure is observed. More precisely, a spatial sequence of bcc and the $\omega$-phase occurs which leads to oscillatory pressure profiles. The formation of the $\omega$-phase is not an artefact of the Dzugutov potential since it occurs frequently in bcc-elements and -alloys upon cooling, quenching or compression [193].

The difference between the formation of the modulated $\omega$-phase and the locked-in solitons is that the $\omega$-phase spreads out at subsonic speed whereas the locked-in solitons move at the speed of sound [72]. The non-steady solitary waves on the other hand are much faster than the plastic wave front, at least at high piston velocities in the overdriven range, and move far ahead of the plastic wave front through the undisturbed or elastically uniaxially compressed material.

## 6.3 Generation of the shock waves and orientation of the samples

Details about the generation of shock waves, the interaction, and the simulation setup have been presented in the previous chapter already.

Most of the runs we have been carried out with the momentum mirror method to generate the shock wave. When we noticed that the strength of the solitary wave was strongly depending on the orientation we have repeated the simulations with the symmetric impact method. To study the stability of the solitary waves and to answer the question if they may be a consequence of the infinitely large acceleration of the atoms at the beginning of the simulation we invented a new scheme where the samples do not collide at full speed at the beginning of the simulation but where the piston velocity (respectively the sample velocity) is increased linearly until the desired final velocity is reached.

For the simulation of shock waves it is necessary to apply periodic boundary conditions, otherwise the sample would explode. The direc-

tion of the shock wave is chosen parallel to one of the coordinate axes, for example the $x$-axis. This limits the possible crystalline directions along which the shock wave can travel to the rational directions indexed by the Miller indices. In addition to the main symmetry directions studied in the previous chapter we have carried out simulations along many other low-index directions to find out the dependency of the solitary wave amplitude on the orientation of the sample.

The size of the samples depends on the orientation. Therefore we will not list all the numbers. Most of the simulations have been performed with a small sample of about $20\times20\times100$ interatomic distances $a$ containing of the order of 40,000 atoms. To study the influence of the sample size on the solitary waves longer samples (of length 200, 300 and $600a$ with up to 250,000 atoms), thinner (with a cross section of $6\times6$ and $8\times8a^2$) and thicker samples ($40\times40\times300a^3$ with 500,000 atoms up to $120\times120\times600a^3$ with 4.5 million atoms) have been used.

The samples have been equilibrated in the usual way before the simulations started.

## 6.4 Results for shock waves along the three-fold directions

The Hugoniot diagram for shock waves in bcc along the three-fold direction is represented in Fig. 6.1. For the general description see Figs. 5.3 and 5.4.

Two additional wave fronts are drawn in Fig. 6.1: The velocity with which the three layer bcc-phase is transformed into the $\omega$-phase, and the velocity of the fastest solitary wave train. Both curves meet at about $u_p/c_3 = 0.185$ when they cross the velocity of sound. This is a clear indication that both phenomena are related. Between $u_p/c_3 \approx 0.2$ and $u_p/c_3 \approx 0.3$ up to about 3 to 4 additional solitary wave maxima which are slower than the first solitary wave but faster than the transition front can be distinguished. The velocities of the latter have not been drawn for clarity.

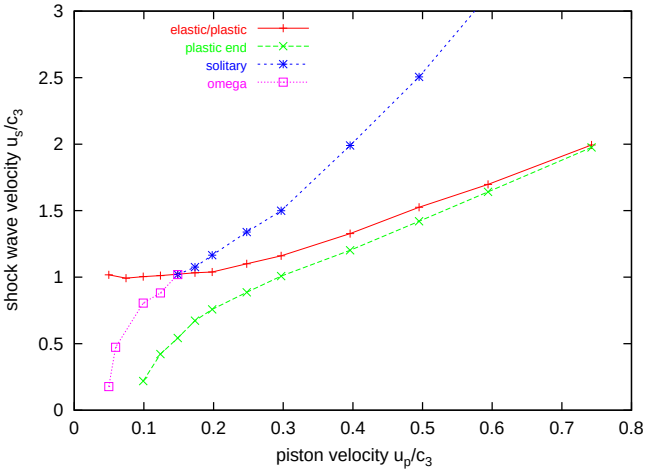


**Figure 6.1:** Hugoniot diagram for shock waves along the three-fold axis in the bcc crystal. The axes are scaled with the velocities of sound. The plus signs mark the velocity of the elastic and transition wave fronts, the crosses the speed with which the high-defect phase transforms into a low-defect structure. The stars and the squares mark the propagation velocity of the fastest solitary wave and the spreading of the $\omega$-phase respectively.

### 6.4.1 Evolution of the hydrostatic pressure profile with increasing piston velocity

The formation of the ω-phase and the evolution into the solitary waves can be described by means of the hydrostatic pressure as a function of increasing piston velocity $u_p$. Instead of the hydrostatic pressure the shear stress or the longitudinal temperature could be used equally well.

1. $u_p/c_3 = 0.005 - 0.035$: A non-steady elastic wave exists. The rising edge of the wave becomes flatter over time since the bottom of the wave moves faster than the top. At about $u_p/c_3 = 0.035$ the hydrostatic pressure reaches the transition pressure from bcc to the close-packed phase. A phase transition to a close-packed phase would be expected now, but it is delayed by the creation of the intermediate ω-phase.

2. $u_p/c_3 = 0.035 - 0.175$: The non-steady elastic wave is still present. It is followed by a plateau of the hydrostatic pressure which is lower than the maximum of the elastic wave between $u_p/c_3 = 0.05$ and 0.075 and higher between $u_p/c_3 = 0.075$ and 0.125. Between $u_p/c_3 = 0.135$ and 0.16 the hydrostatic pressure grows slightly.

   In the plateau region the ω-phase is present. It is most prominent around $u_p/c_3 = 0.1$, and is subsequently transformed into fcc by the transition wave.

3. $u_p/c_3 = 0.175$: The slope at the front of the ramp becomes steeper and grows higher than the following plateau. This is the precursor of the first solitary wave.

4. $u_p/c_3 = 0.185$: The first solitary wave peak becomes clearly visible, but is still connected to the ramp.

5. $u_p/c_3 = 0.2 - 0.3$: Now the first solitary wave is separated from the ramp. The plateau is no longer flat but modulated, indicating the nucleation of further solitary wave peaks. The pattern of oscillations remains the same during observation time. With increasing piston velocity the distance between the solitary waves gets larger and larger and the oscillation amplitude grows until

well-separated peaks are present. The distance between the individual solitary wave peaks and to the transition front also grows with simulation time.

6. $u_p/c_3 = 0.3 - 0.75$: The first solitary wave is still stable, but the other solitary waves decay. More precisely, they emerge from the transition front, move into the region between the first solitary wave and the transition front, and vanish. At $u_p/c_3 = 0.35$, for example, two solitary waves are still detectable, but at $u_p/c_3 = 0.4$ only one solitary peak is left over.

In summary we find a very complex scenario: After the bcc-phase has become unstable at $u_p/c_3 = 0.035$ it does not transform directly into a close-packed phase in the underdriven regime. An intermediate $\omega$-phase shows up between the shock front and the transition to the close-packed phase. At increasing shock strengths the pressure profile develops a spatial modulation. We notice a sequence of up to four bcc- and $\omega$-phase slabs. The pressure is high in the $\omega$-phase and low in the bcc slabs. The width of the $\omega$-phase slabs shrinks with increasing piston velocity as they develop into the solitary waves. The velocity of the wave front of the new phase grows but remains below the velocity of the uniaxial compression wave. In the overdriven region the modulation develops into a sequence of solitary wave peaks. At very high piston velocities only one solitary wave peak is left over.

**Velocities of the solitary waves**

The velocity of the solitary wave peaks is related to their height: The higher a peak is, the faster it moves. Since the trailing peaks are lower than the first one they also move slower. The velocities and heights of a specific solitary wave peak are not constant but decrease very slowly with time. This can bee seen if Fig. 6.2 is held at a glancing angle. The solitary waves which emerge from the transition front may be overtaken again by the transition front after some time. At low temperature the height of the first solitary wave is constant during simulation time and the width is about $4a$. The other solitary waves also have constant height, and their width is about 5-6$a$.

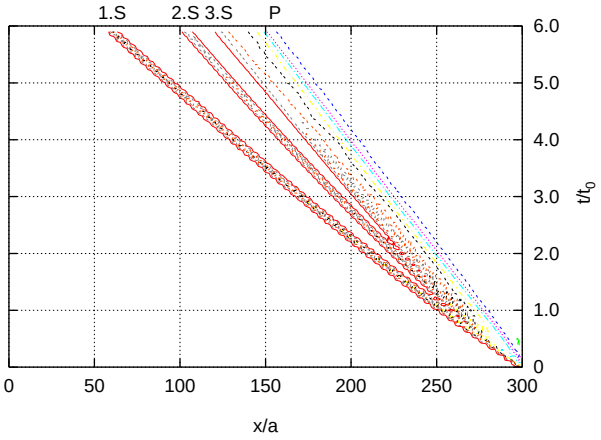


**Figure 6.2:** Hydrostatic pressure as a function of time and path at temperature $kT = 0.001$, the piston velocity is $u_p/c_3 = 0.25$. Three solitary wave peaks (1.S, 2.S and 3.S) are visible in front of the transition wave front (P).

### Temperature dependency

At low temperatures the solitary waves move through the whole sample up to at least $600a$ in the samples with cross section $20\times20a^2$. At finite temperatures they are damped. The damping increases with temperature: At $u_p/c_3 = 0.25$ it becomes visible between $kT/\epsilon = 0.03$ and $kT/\epsilon = 0.04$ for small samples (Fig. 6.3), at $u_p/c_3 = 0.4$ the damping starts already between $kT/\epsilon = 0.01$ and $kT/\epsilon = 0.02$. At higher temperatures solitary waves are no longer present.

## 6.4.2 Properties of the ω-phase

The ω-phase is observed for the first time at a piston velocity of about $u_p/c_3 = 0.05$. The velocity of the interface between bcc and the ω-phase grows much faster than the speed of the following interface with the close-packed phase up to $u_p/c_3 = 0.1$. At this velocity the intermediate phase is most prominent. If the piston velocity increases further, the transition front speeds up rapidly and at $u_p/c_3 = 0.185$ it catches up with the first interface. Now the phase transition goes directly from bcc

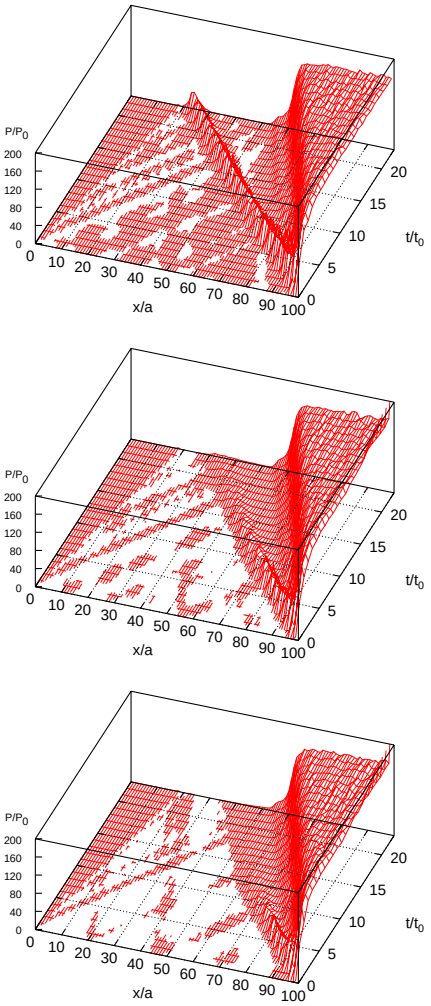


**Figure 6.3:** Damping of the solitary wave at different temperature. From top to bottom: $kT = 0.01$, 0.05, and 0.1 $\epsilon$. The piston velocity is $u_p/c_3 = 0.4$. The solitary waves are visible in front of the transition waves.

to the close-packed phase.
The bcc-phase is a three layer structure with respect to the three-fold axis. The new intermediate phase on the other hand is a two-layer structure which looks hexagonal in projection (See Fig. 6.4). The three-fold axis of $\omega$-phase and the parent bcc-phase are aligned. The periodicity perpendicular to the hexagonal layer is approximately $1a$, and the neighbor cells are either tetrahedra or rectangular pyramids. The atoms occupy their sites at random in one of the two layers. They may jump from one layer to the other. There are, however, certain rules for the positioning of the atoms. No clusters of three mutually neighboring atoms (triplets) are permitted. Fractally looking triangular pattern can be superimposed on the atoms (Fig. 6.4). More precisely, there are three variants of triangular patterns which form different domains. In Fig. 6.4 only one domain has been drawn for simplicity.
Both the RDF (Fig. 6.5) and the ADF (Fig. 6.6) clearly indicate that the $\omega$-phase is a new phase and cannot be confused with bcc or the close-packed phases. The same is true if the RDF is compared with those of the $\sigma$-phase and the quasicrystals studied in Chap. 5.
The $\omega$-phase exists up to temperatures of about $kT/\epsilon = 0.15$. The velocity of the transition wave increases with temperature and "eats" up the $\omega$-phase.
The new phase is created under uniaxial stress. If the stress is released it slowly transforms back into the bcc-phase. Only a few well separated point defects may stay over. This indicates that the transition is reversible.

### 6.4.3 Description of the internal structure of the solitary wave peak

With regard to the hydrostatic pressure the solitary wave peaks appears to have a width of $4 - 6a$. But if we look at the displacement of the atoms along a certain atomic chain we find that the width is 1 or at most 2 $a$ (See Fig. 6.7). The figure shows the shortening of the distance between the atoms on three arbitrarily chosen chains. At the peak of the solitary wave the distance between two atoms is compressed by 25 to 30%, whereas the preceding and following distances are shortened by 5 to 10%. The other distances are more or less unchanged. The reason for the difference between the width of the hydrostatic pressure and the

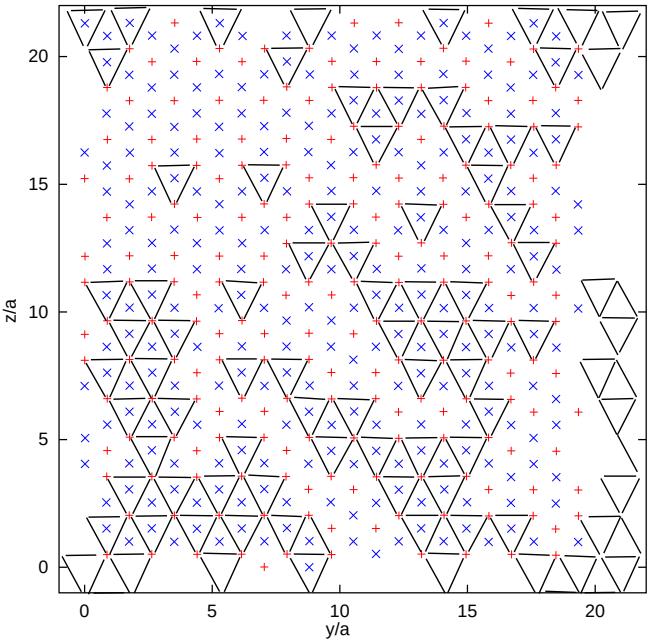


**Figure 6.4:** Cut through the intermediate $\omega$-phase. The crosses indicate one layer, the plus signs the other layer. The triangular lattice cells of one domain have been superimposed. The empty triangles are periodic images repeated on the opposite side.

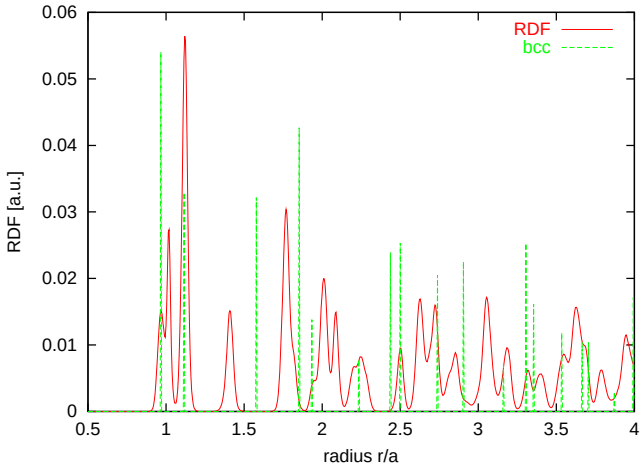


**Figure 6.5:** RDF of the intermediate phase. The most prominent disagreement is visible at around $r = 1.4a$. The split first peak clearly indicates that this is no close-packed structure.

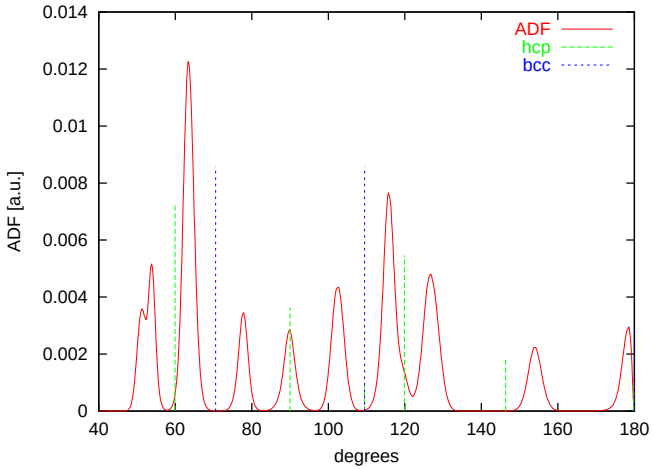


**Figure 6.6:** ADF of the intermediate phase. The vertical lines indicate the angles in bcc and fcc. The disagreement is obvious.

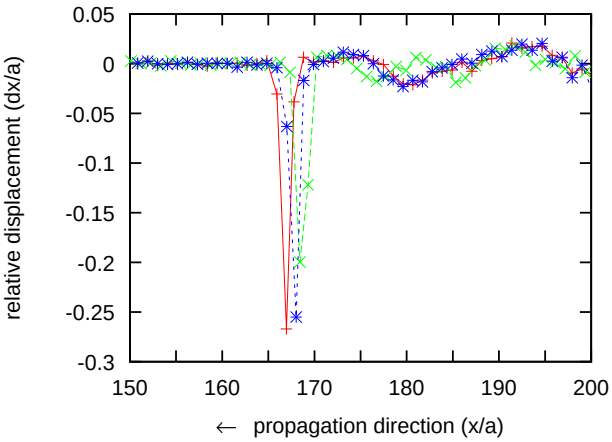


**Figure 6.7:** Displacement of the atoms at the position of a soliton peak. The three signs indicate three arbitrarily chosen chains.

displacement of the atoms can be seen in the picture: The displacements are not perfectly correlated. After the solitary wave has passed the atoms are back at their bcc positions. The modulation of the distances behind the solitary wave (Fig. 6.7) indicate that the longitudinal temperature has risen from $kT = 0.001\epsilon$ to about $kT = 0.01 - 0.02\epsilon$.

In Fig. 6.8 the shocked structure is projected onto a plane perpendicular to the three-fold axis. It can already be seen that the solitary waves are modulated in the transverse direction. It is also obvious that the sample returns to the original bcc structure after the solitary wave has passed.

Fig. 6.9 shows what happens within the solitary wave peak: The three-layer bcc structure is partially transformed into the $\omega$-phase. A perfect transition is impossible since the solitary wave is very thin and fluctuates. In a perfect bcc structure the three different layers should look like triangular patterns. These layers are partially modified like the ones represented in Fig. 6.4. The circles in Fig. 6.9 indicate where at this very moment of the simulation the atoms are in the two-layer configuration. Due to the dynamic nature of the solitary wave these locations will change permanently.

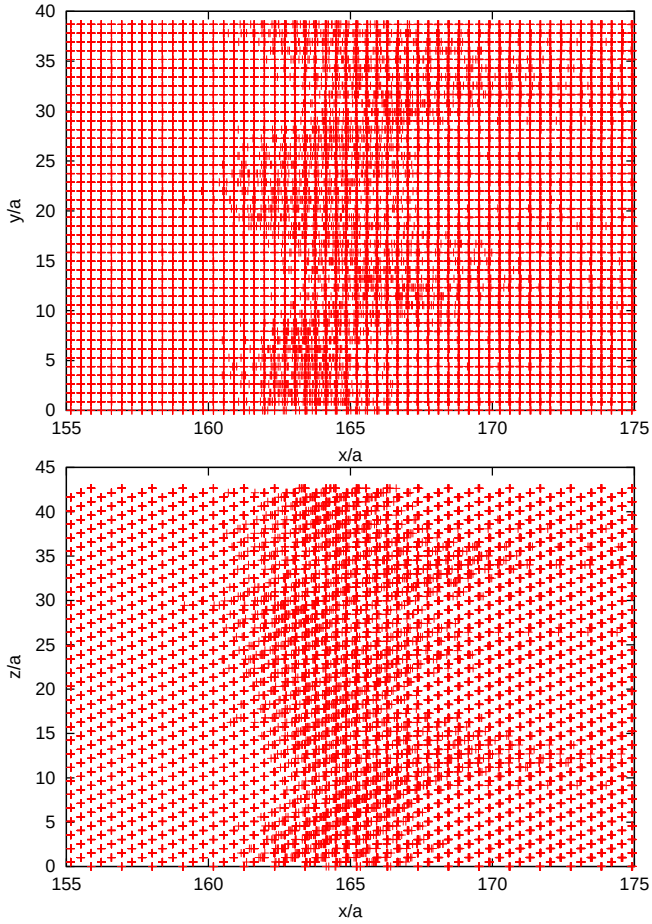


**Figure 6.8:** Projection of the structure with the solitary wave perpendicular to the three-fold axis. Upper part: $[2\bar{1}\bar{1}]$-direction, lower part $[01\bar{1}]$-direction. The shock wave moves to the left.

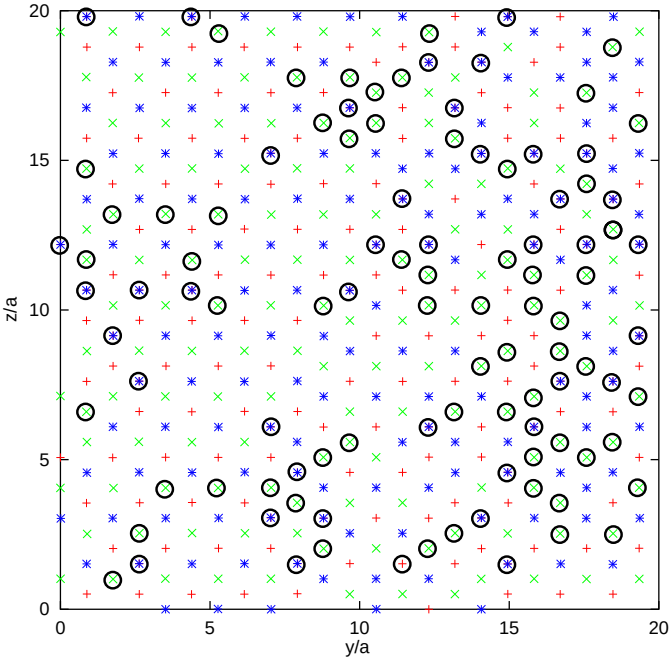


**Figure 6.9:** Cut through the structure at the maximum of a solitary wave peak. The crosses, plus signs and stars indicate three bcc layers. In a perfect bcc sample all layers would form a triangular lattice. The black circles indicate the positions where the sequence repeats after two layers, i.e. we find the $\omega$-phase. Compare this figure to Fig. 6.4!

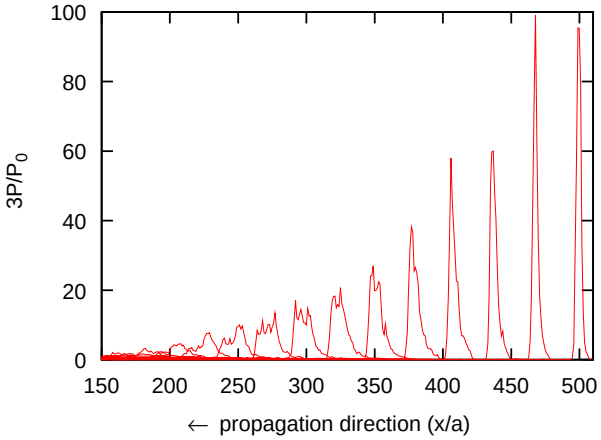


**Figure 6.10:** Decay and broadening of a soliton peak as a function of pressure. The peaks are plotted at equal time intervals.

### 6.4.4 Decay with width

In the broad samples (width $40\times40a^2$ and larger) the solitary waves seem to decay and broaden if only cross-section averaged histograms of the simulations are taken into account (See Fig. 6.10). The true reason for this behavior is not that the hydrostatic pressure or the shear strain decreases, but that the correlation between the solitary peaks on the different parallel atom chains vanishes.

This becomes obvious if the peak value of the hydrostatic pressure is monitored for example (Fig. 6.11, see also Fig. 6.8). At the beginning the surface formed by the peak values is completely flat. Then it starts to fluctuate randomly. After a while the lowest or the second lowest mode which is compatible with the boundary conditions starts to grow and enslave the other modes. At the end of the simulation it is no longer possible to represent the peak values by a simply connected surface. When the solitary wave reaches the end of a sample fountains of atoms are observed coming out of the material at the positions where the solitary wave first hits the surface.

The decay of the correlation with the width of the sample may render

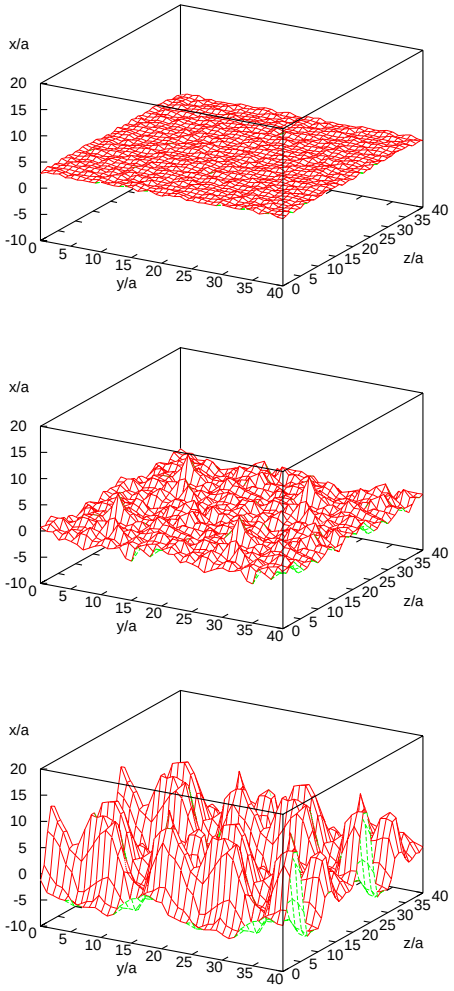


**Figure 6.11:** Maximum of the hydrostatic pressure in a comoving frame at times 0, 2.5, and 7.0 $t_0$. The piston velocity is $u_p/c_3 = 0.4$.

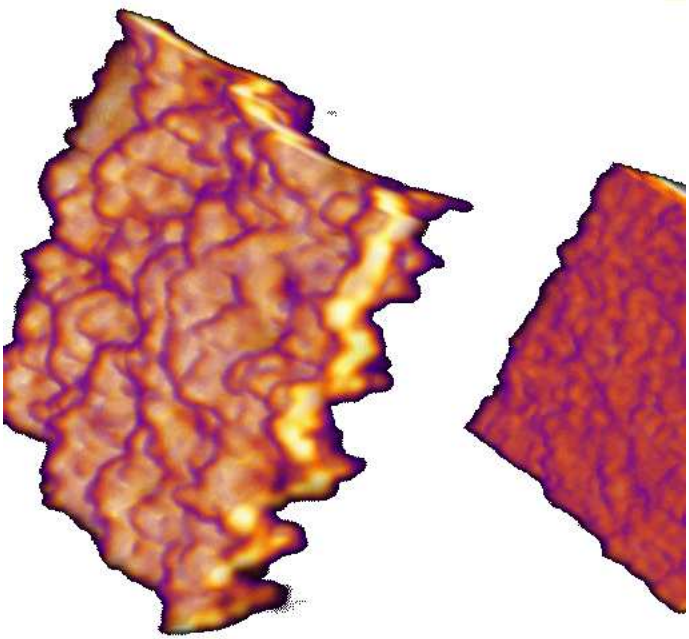

**Figure 6.12:** Three-dimensional structure of the solitary peak at $u_p/c_3 = 0.4$. The solitary wave is the warped plate at the left in the foreground, the transition front is visible at right in the background. The sample in between is distorted only elastically and is not made visible therefore. Yellow indicates the highest pressures, blue the lowest, red is in between.

an experimental detection of the solitary waves impossible, especially if the limit for large widths is zero. Up to now it has not been possible to determine this limit since our computational resources were too limited.

### 6.4.5 Solitary waves in other phases and along different directions

Short-time solitary waves also show up along the four-fold and two-fold direction in bcc, but they are always strongly damped and occur only at high piston velocities. In the metastable phases of the Dzugutov potential, the $\sigma$-phase and the quasicrystal, intermediate solitary waves are observed if the samples are shocked perpendicular to the basic square-triangle layer direction. No solitary waves are found if the shock wave direction encloses an angle of 45 or 90 degree with respect to the basic layers.

## 6.5 Shock waves and solitary waves along arbitrary directions

In addition to the main symmetry directions we have looked for solitary waves along a large number of other directions. The size of these samples ranged from 1.2 to 3.5 million atoms. The investigation has been carried out for two reasons: First to determine the allowed deviation of the solitary waves from the main symmetry directions (low angle case), then to determine the feasibility of a description of the solitary waves which varies smoothly with direction (large angle case). The amplitude of the hydrostatic pressure at a fixed time $t = 4t_0$ has been chosen as a measure of the strength of the solitary waves. This may be a rather crude measure, but it permits us to get a gross overview. For some directions we have repeated the simulations with different sample sizes and found an average variation of the intensities of about 7%.
The behavior of solitary waves along arbitrary directions strongly depends on the boundary conditions, i.e. if the momentum mirror method is applied or if two blocks of equal size are brought into collision. In both cases, no solitary waves are observed around the four-fold and two-fold axes and in the directions between them, i.e. in the planes perpendicular to the four-fold axis (Figs. 6.13 and 6.14).

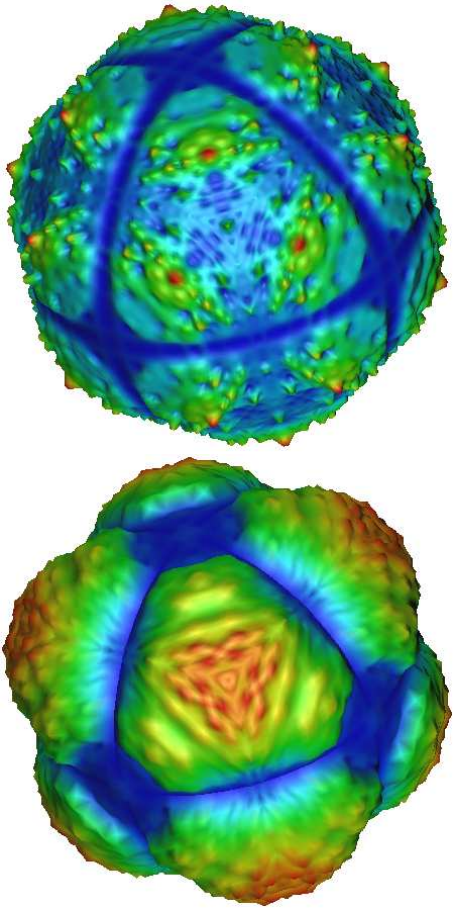

**Figure 6.13:** Strength of the solitary waves as a function of propagation direction (qualitative description). Dark blue indicates no solitary waves. Green are the intense solitary waves (i.e. three-fold axis). Yellow and red mark very strong solitary waves (i.e. [211]-direction). Top: momentum mirror method, bottom: two block method.

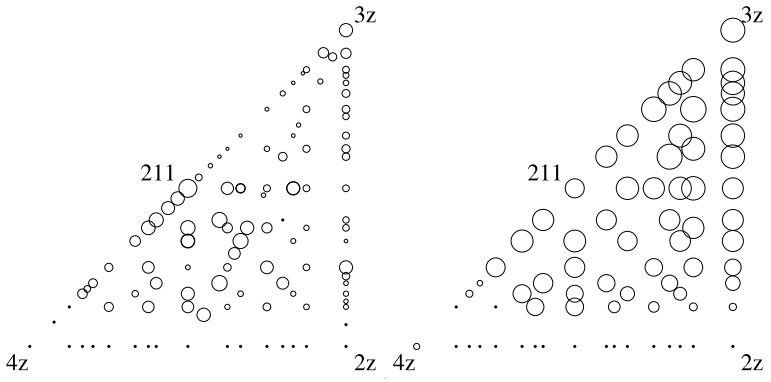


**Figure 6.14:** Strength of the solitary waves as a function of propagation direction (quantitative description). The area of the circles is proportional to the intensity of the solitary waves. Dots mark the directions were no solitary waves have been observed. The plane perpendicular to the three-fold axis contains the [211]- and the two-fold direction. Left: momentum mirror method, right: two block method.

### Results for the momentum mirror

If the momentum mirror method is used then the intensity of the solitary waves varies rapidly and unsystematically with direction. Solitary waves exist along many low index directions and along the [211]-direction for example they are stronger than along the three-fold axis! Other directions with strong solitary waves include the [321]- and the [531]-direction. In contrast, solitary waves along the [421]-direction, which is closely nearby, are very weak. Between the two- and the three-fold axis remnants of solitary waves exist. The strongest solitary waves seem to exist in the plane perpendicular to the three-fold axis, especially between the three- and four-fold direction.

The half width at half maximum around the three-fold axis is 3 degrees. Within a ring of about 18 degrees around the three-fold axis almost no solitary waves occur (Figs. 6.13 and 6.14). Thus solitary waves of the usual type will be found only if the shock direction is well aligned with the three-fold axis. The belt between about 20 and 30 degrees to the three-fold axis indicates that a continuous contribution to the solitary waves might exist. But it is more likely that the solitary waves depend

strongly on the lattice direction since even in the belt huge differences of closely lying peaks exist which cannot be resolved in Figs. 6.13 and 6.14. So the figure should look more like a spherical diffraction pattern.

**Results for symmetric impact**

If two blocks of material are moved against each other at constant speed $u_p$ then the intensity distribution of the solitary waves looks completely different. The intensity decreases (up to random fluctuations) continuously with the angle to the three-fold axis (Figs. 6.13 and 6.14). The reason for the different behavior for the two boundary conditions is rather obvious: In the momentum mirror method we have a rigid boundary, and therefore it should play a role how for example the densely packed lattice planes are oriented with respect to it. Extinction effects and a strong angle dependency are expected. Furthermore the boundary acts like a twin boundary. In the case of two colliding blocks we have a soft boundary condition at their common interface. The dense lattice planes will bend and adjust otherwise. Therefore a smooth variation of the solitary wave intensity with direction is more likely.

We have plotted the atoms in the solitary wave peak for [211]-solitary waves simulated by the mirror method. It is clearly visible that diagonal collision cascades exists (See Fig. 6.15). The open question is why this is the case for some directions and not for others? A possible explanation might be the lack of symmetry: In the case of the two-and four-fold direction diagonal cascades are impossible since the environment of the colliding atom is centrally symmetric. This is not the case for the directions with large solitary waves, except for the three-fold axis. But for the latter we can explain the solitary waves by the existence of direct collision partners (See Sec. 6.8).

Since [211] is still a rather low indexed direction as compared to [531] for example, this result demonstrates how difficult it must be to work out an explanation for the solitary wave phenomenon for arbitrary directions. We have looked at atomic distances parallel to the shock wave direction and at layer distances perpendicular to it, but none of this measures gives a reasonable explanation for the appearance of solitary waves.

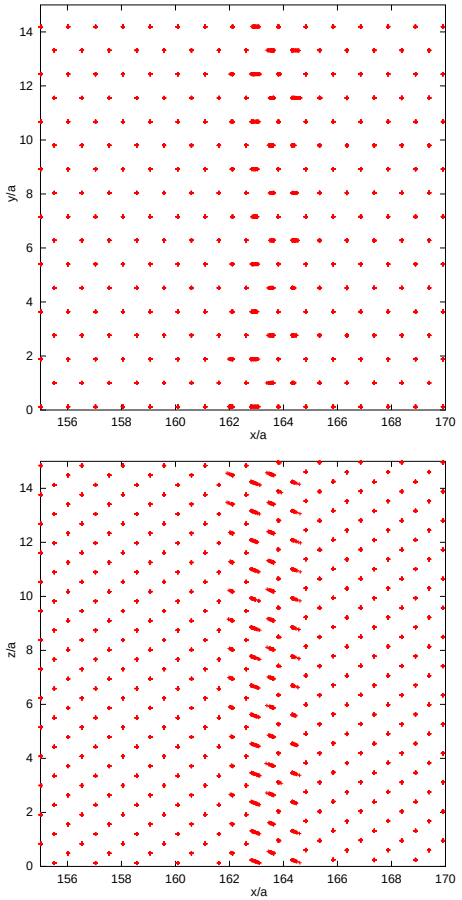


**Figure 6.15:** Solitary wave along the [211]-direction. Upper part: x-y-plane, lower part: x-z-plane.

## 6.6 Ramping up the velocity

The question which arises in this context is: Are all the solitary wave trains merely artefacts of the boundary conditions and is it possible to avoid them. The answer is that the solitary waves are indeed stable and independent of the boundary conditions. The problem with the momentum mirror as indicated at the beginning of this chapter is that there exists an acceleration singularity. To resolve it we have changed the simulation setup, i.e. we have increased the piston velocity linearly from zero to the desired end velocity. This introduces a new variable, namely the time interval $t_r$ of ramping up the velocity. If $t_r$ is large, only a step instead of the solitary wave is present. If $t_r$ is very large, it is indeed possible to suppress the solitary waves completely. In contrast, if $t_r$ is short, almost nothing changes: The solitary wave gets broadened but at the end of the accelerating phase it sharpens and increases its height. If the accelerating phase is enlarged several solitary peaks show up. It may occur that the subsequent solitary peaks are damped away, but this was not the case until the end of the sample has been reached. In summary the following is observed: If the piston velocity $u_p$ is ramped up from zero the final state of the solitary waves is shifted to an effective $u_{p,\mathrm{eff}}$ with $u_{p,\mathrm{eff}} < u_p$. If $u_{p,\mathrm{eff}}$ is in the low underdriven range, no solitary waves exist any more. If $u_{p,\mathrm{eff}}$ is in the low overdriven range, a scenario with several solitary wave peaks unfolds. Thus the examination demonstrates that the solitary waves are an inherent feature of the system. They may be modified, but they will rise up later if they are suppressed at the beginning of the simulation.

## 6.7 Theoretical explanation of the occurance of the ω-phase

The ω-phase observed in the simulations is never perfect. We therefore have to deal with possible defects and imperfections.

### 6.7.1 Geometrical description of the ω-phase

The properties of the imperfect ω-phase can be described by different pictures as summarized by de Fontaine [64, 62]. A certain picture must

not exclude another.

### (111)-plane collapse picture

In the perfect, completely collapsed $\omega$-phase of infinite extension all $B$ and $C$ planes are shifted by the full displacement, i.e. they coincide. This situation has never been observed. To our opinion it is not expected to occur: it is not appropriate to describe bcc as a stacking of layers, but as a dense packing of close-packed atom chains. The basic defect is a shift of the chains. This view is also very important for the explanation of the solitary waves (See Sec. 6.8). Fcc on the opposite is a stacking of densely packed layers and the basic defect is a stacking fault.

In the crumpled $\omega$-phase the displacement is incomplete, i.e. the $B$ and $C$ planes do not coincide. This situation does not occur in the simulations. It is certainly not present in the case of weak shock waves where the $\omega$-phase spans a long distance. But since the transition is dynamical it cannot be ruled out completely, especially for the modulated structures and the solitary waves.

The $\omega$-phase in real crystals forms ellipsoids with the long axis parallel to the three-fold direction [218] or small cubes (size 1.5nm). In the simulations, the $\omega$-phase fills the whole cross section of the samples and stretches from bcc to the close-packed phase.

Stacking solitons, extra or missing planes have been proposed but could not be detected in the simulations. The same is true for transverse defects, i.e. large domains separated by grain boundaries [22, 23, 105].

This model clearly fails to explain the simulation results.

### $\frac{2}{3}[111]2\pi/a$-longitudinal displacement wave picture

The $\omega$-phase can be generated by a longitudinal phonon wave with $\mathbf{k} = \frac{2}{3}[111]2\pi/a$ and amplitude $\sqrt{3}/12a$. If the wave vector is different from this ideal value, a modulated structure occurs. A wrong amplitude can have the same effect as a wrong wave vector. The crumpled phase and stacking defects can be the consequence. A further possibility is the lock-in to a sequence of bcc and $\omega$-domains [183] which is found in our simulations. If the piston velocity is increased beyond $u_p/c = 0.2 - 0.3$. A strong modulation sets in as predicted by this model.

### [111]-atomic row movement picture

Up to now the descriptions of the ω-phase were 2+1 dimensional, i.e. planar patches move correlated. Only longitudinal and perhaps large-scale transverse defects occur. The behavior observed in the simulations should better be described as 1+2 dimensional, i.e. the atoms along one-dimensional chains move correlated, but neighboring chains are independent. This picture fits best for weak shock waves below $u_p/c = 0.175$: in contrast to the predictions of the first model we do not find a perfect hexagonal network and a distribution of the atoms in the ratio 1:2 into the two ω-phase layers but a ratio of 0.444:0.556 (±0.002). The reason is the following: There are three variants of the ω-phase depending on how the planes collapse ($A$+$B$, $B$+$C$, or $C$+$A$). Since the domains fit together coherently, there has to be an adjustment between the variants which changes the trivially expected distribution of the atoms in the three layer structure from 1:2 to 4:5.

De Fontaine and Buck have carried out Monte Carlo simulations of the ω-phase transformation [63]. They describe the transformation as a one-dimensional linear displacive defect, together with a two-dimensional cooperative ordering of neighboring chains. Their results support the third model and resemble most closely our shock wave simulations: Especially Fig. 9 and the central part of Fig. 10 of Ref. [63] are practically the same as our Fig. 6.4.

Petry et al. [148] called the behavior of β-Ti (which transforms into an ω-phase) "liquid-like". This is another way to express that along the [111] chains there are strong restoring forces and a long-range correlation. But if a [111] chain vibrates, its neighboring chains do not follow this motion. Thus the perpendicular motion is localized, the correlation is lost rapidly, and the lifetime corresponds to roughly a vibrational period. Petry et al's description fits nicely to the decay of the solitary wave found in our simulations and is similar to our crude model.

The only other model which take a transverse variation of the structure into account is the Bragg-Williams model of de Fontaine and Kikuchi [64] where a Landau-type order parameter is constructed for the average shift of a bcc plane. A full analytical model of the transverse modulations observed in the ω-phase transformation and in the solitary waves is still lacking.

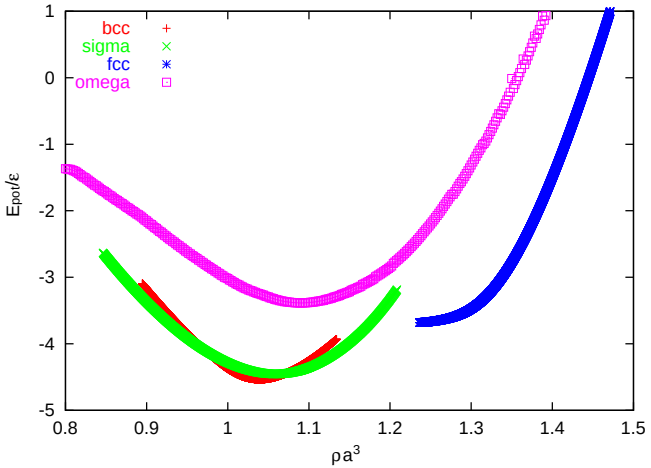


**Figure 6.16:** Potential energy of the $\omega$-phase vs. density for isotropic volume change. The lattice constants were adjusted to the optimal ratio $d/b$, where $b$ is the in-plane and $d$ the perpendicular lattice constant of the $\omega$-phase.

### 6.7.2 The stability of the $\omega$-phase in Dzugutov materials

At first sight there seems to be no reason why the $\omega$-phase should form in Dzugutov materials. The potential energy at the optimum differs by about $1.4\epsilon$ between bcc and the $\omega$-phase, and the $\omega$-phase is never stable with respect to bcc, the $\sigma$-phase, and close-packed phases if only isotropic deformations are permitted (Fig. 6.16).

This picture changes completely if the bcc-phase is compressed uniaxially as it happens in the shock wave simulations: at a compression of $d/d_0 = 0.917$ ($d_0 = \sqrt{3}/2a$ is the axial lattice constant of bcc in hexagonal representation) the $\omega$-phase becomes more stable than bcc, but at $d/d_0 = 0.835$ the stability switches again to bcc (Fig. 6.17). Remarkably, bcc and the $\omega$-phase both have their optimal lattice constant in the (111) plane at the same value $b = 1.76a$ ($b = \sqrt{2}a$ is the planar lattice constant of bcc in hexagonal description) which indicates that there is no lattice mismatch and no transversal stress is created by the shock wave and the phase transformation. Furthermore, there is no bar-

rier between bcc and the $\omega$-phase if the potential energy is considered as a function of the lattice parameters $b$ and $d$ and the position of the collapsing layers $w/d$. The optimal aspect ratio $b/d$ is also similar for bcc ($b/d = 0.614$) and the $\omega$-phase ($b/d = 0.574$)[1].
The stability of the bcc- and the $\omega$-phase switches several times with increasing compression, but we consider this to be irrelevant since the absolute potential energy increases rapidly and reaches $1.2\epsilon$ at a compression of $d/d_0$=0.835, but $88\epsilon$ at the next intersection at $d/d_0$=0.71. The bcc-structure itself is no longer stable at this compression.
The instability of bcc at a compression of $d/d_0$=0.917 is the reason for the transition to the $\omega$-phase. The reentrance of the bcc-phase stability at $d/d_0$=0.835 causes the modulation of the phase and the solitary wave phenomenon.

### 6.7.3 Phonon dispersion and softening

We have applied the Born-von Kármán theory (For an overview see [24], the details required can be found in [33] and [61]) to compute the phonon dispersion relation for bcc with the Dzugutov potential. Since this potential is very short ranged a limitation of the interaction parameters to only three atomic shells yields the exact phonon dispersion relation in the harmonic approximation. We find that the soft mode occurs at $0.52[111]2\pi/a$ already instead of the $\frac{2}{3}[111]2\pi/a$ in the ideal case. The deviation is large compared to the maximum of $\pm 9\%$ for real materials (Fig. 6.19). Thus the symmetry-induced cancellation [59, 60, 58] of the phonon modes in bcc at $\frac{2}{3}[111]2\pi/a$ does not play a role in our case.
The strong offset leads to a minimal modulation of about $d_{\mathrm{mod}} = 4a$. This value agrees well with the thinnest bcc- and $\omega$-slabs observed in the simulations. If the bcc structure is compressed, the soft mode shifts towards the ideal value, which indicates that the modulation length rises rapidly, in agreement with the simulations (Fig. 6.20).
The soft mode mechanism can also explain qualitatively why solitary waves are observed along certain directions: these directions coincide

[1] On the other hand, there is no low-lying transition path from bcc to the high-pressure fcc phase which is also present in the given parameter space. Bcc and fcc both have $w/d = 1/3$, but different aspect ratios (for fcc $b/d = 2.457$).

[1] If the nearest neighbor Born-von Kármán interaction constant is scaled to one, this leads to $\omega_0$=4 at $k_0 = |[111]2\pi/a|$, the boundary of the reciprocal lattice cell.

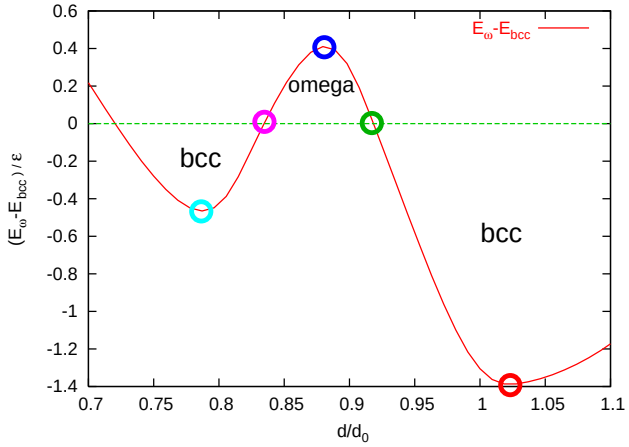


**Figure 6.17:** Difference between the binding energies of bcc and the $\omega$-phase with respect to uniaxial compression.

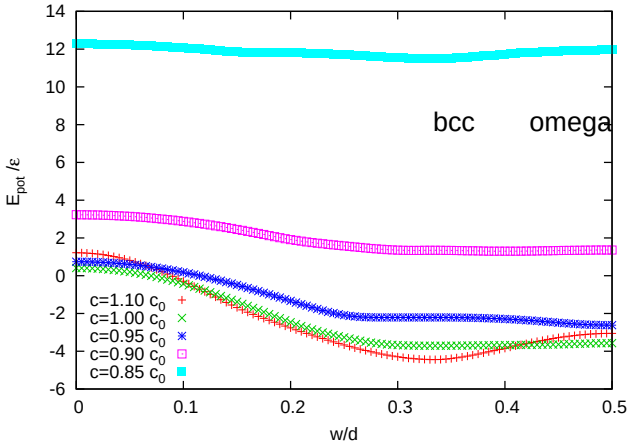


**Figure 6.18:** Potential energies in dependency of the position of the $B$ and $C$ planes. Bcc is at $w/d = 1/3$ and the $\omega$-phase at $w/d = 1/2$. The colors of the lines correspond to the circles in the previous graph.

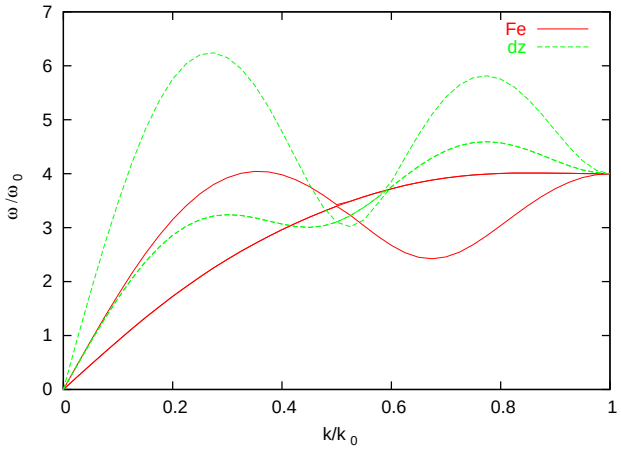


**Figure 6.19:** Phonon dispersion of the longitudinal $\frac{2}{3}[111]2\pi/a$ mode for iron and for the Dzugutov potential. The phonon dispersion relations for other bcc metals look similar to iron. Their minimum is also around $k/k_0 = 2/3$[1].

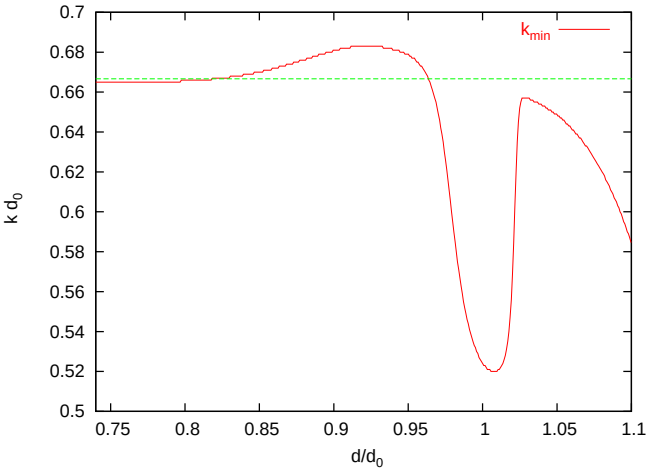


**Figure 6.20:** Position of the minimum of the longitudinal $\frac{2}{3}[111]s\pi/a$ phonon. The green line at $kd_0 = \frac{2}{3}$ indicates the ideal wave length. The strong minimum at bcc ($d/d_0 = 1$) leads to a pronounced modulation.

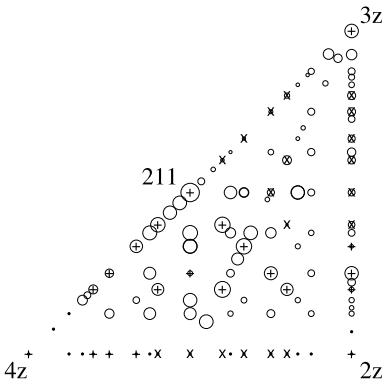


**Figure 6.21:** Intensity of the solitary waves determined by the mirror method compared to the properties of the phonon modes. The crosses indicate the directions where quasi-longitudinal modes with softening exist. The x-signs indicates a strong mixing between quasi-longitudinal and quasi-transverse modes. For the unsigned directions the phonon dispersion has not been determined.

with the existence of a minimum in the quasi-longitudinal mode, namely the mode which becomes longitudinal in the long-wave limit (Fig. 6.21). Along the other directions a mixing occurs with transverse modes. The softening modes exist along the three-fold direction and in a belt between the line going through the [211]- and [331]-direction and the plane perpendicular to the four-fold axis. No softening modes exist in a circle of about 20 degrees around the three-fold direction. The similarity of this pattern with the intensity of the solitary waves measured with the mirror method is quite good except for the plane perpendicular to the four-fold direction. But for this plane another explanation exists for the missing of the solitary waves (Compare Sec. 6.4.5). No suitable agreement, however, is found in the case of the symmetric impact method simulations. This is surprising since we would expect from the arguments given in (Sec. 6.4.5) that continuum description apply better in this case than for the momentum mirror simulations.

### 6.7.4 Evaluation of the Landau theory

Cook and de Fontaine [29, 30, 31, 32] have presented a one-dimensional phenomenological Landau theory to explain the $\omega$-phase transition. The order parameter is the amplitude of the $\frac{2}{3}[111]2\pi/a$ phonon. A modulated phase can easily be explained with this model since it is quite natural that the minimum of the free energy with respect to $\mathbf{k}$ shifts if the Landau parameters change. Sanati and Saxena [181, 182] have extended the Landau theory by Cook by including a spatial gradient (Ginsburg) term. Kinks corresponds to $\omega$–bcc or bcc–$\omega$ domain walls if both phases are equally stable. A soliton represents a slab of the $\omega$-phase within bcc if the $\omega$-phase is more stable than bcc and an anti-soliton represents the opposite case. Moving domain walls can be generated by boosting the static solutions. The lattice cases occur if the sequence of phases is repeated.
Only kinks and solitons are found in the simulations which tells us that the phase transformation is driven by an instability of bcc with respect to the $\omega$-phase. The lattice solutions which are realized by modulated structures observed in the simulations cannot be used to judge the stability of bcc and the $\omega$-phase since these occur in all cases. Unfortunately the analytical theories are only one-dimensional whereas our results require a full three-dimensional treatment. To our knowledge, nobody has attempted yet to create a three-dimensional theory.

**Application to the simulation results**

We have calculated the parameters of the Landau free energy

$$F = F_0 + H\eta + \frac{A}{2}\eta^2 + \frac{B}{3}\eta^3 + \frac{C}{4}\eta^4 \tag{6.1}$$

for the $\omega$-phase transformation induced by a uniaxial compression of bcc. The gradient term $(\nabla\eta(x))^2$ has been omitted since we assume that $\eta$ is constant throughout the sample. At $T = 0$ the free energy is equivalent to the potential energy $E_{\mathrm{pot}}$ and can be computed directly from the lattice sum of the Dzugutov potential as a function of the compression $d/d_0$ and the position $w/d$ of the shifted layers for fixed $b = 1.76a$. The usual assumptions for the Landau theory are that $A$ is temperature-dependent, whereas $B$ and $C$ are essentially temperature-independent such that the equation for the free energy can be brought

into a reduced form with $f - f_0 = C^3/B^4(F - F_0)$, $\phi = C/|B|\eta$, $a = AC/B^2$, $b = -1$, $c = 1$, and $h \approx 0$. Thus $f = f_0 + a\phi^2/2 - \phi^3/3 + \phi^4/4$. The dependence on temperature has to be replaced by a dependence on uniaxial compression $d/d_0$ in our case.

A further prerequisite for the Landau theory is that there is a stable phase and a competing metastable phase which are separated by a barrier and change their roles as a function of $T$ or $d/d_0$ respectively.

The order parameter $\eta$ should be related to $w/d$. A direct identification of $\eta$ with $w/d$ fails since $w/d$ is a periodic function modulo $d$. Dmitriev et al. [41] have described how to apply the Landau theory to a periodic order parameter. If we set

$$\eta = \frac{2}{3}\left[\sin\left(2\pi\frac{w}{d} + \frac{\pi}{6}\right) - \frac{1}{2}\right], \tag{6.2}$$

then the parameters $H(d/d_0)$, $A(d/d_0)$, $B(d/d_0)$ and $C(d/d_0)$ can be computed as functions of the compression $d/d_0$. We find that the linear coefficient $H$ is almost zero which indicates that bcc is always close to an extremum.

But in contrast to the expectations we observe that all the other parameters are strongly dependent on $d/d_0$ (See Fig. 6.22). The situation is even worse: $B$ and $C$ are directly proportional and vary much stronger as a function of $d/d_0$ than the parameter $A$. They even change signs in the range of interest. Thus a reduction of the free energy equation is not possible. On the other hand we have to stress that the Landau free energy $F$ fits $E_{\mathrm{pot}}$ very well in the whole range $0.8 < d/d_0 < 1.1$.

Now we will consider the second set of Landau conditions: The coexistence of stable and metastable phases. We find that these conditions are violated in the uncompressed state $d = d_0$ since the ω-phase forms a local maximum and not a minimum. Only in the ranges between $d/d_0 = 0.77$ and 0.78 and between 0.82 and 0.92 two phases coexist (See Fig. 6.23). The presence of the second range tells us that the Landau principle is indeed applicable since the ω-phase is the global minimum in the largest part of this range and bcc or a slightly distorted bcc structure form a local minimum. A barrier between both phases exists. At low compression there is a sudden jump from bcc to the ω-phase whereas there is a continuous crossover at the reentry of bcc.

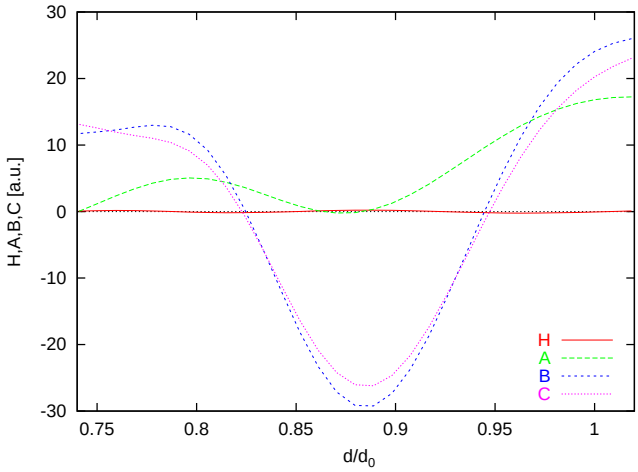


**Figure 6.22:** The parameters of the Landau energy.

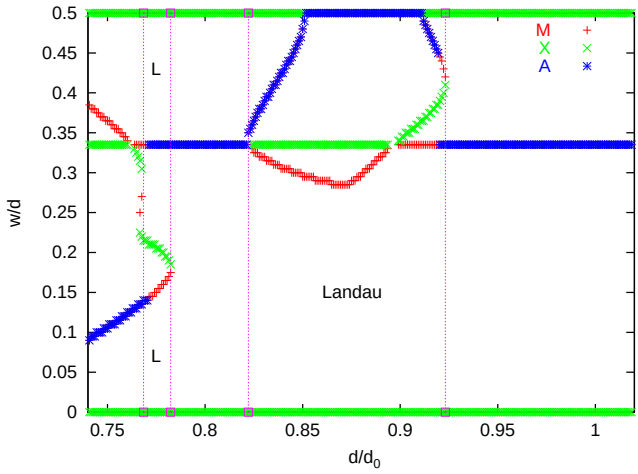


**Figure 6.23:** Position of the extrema of the potential energy as a function of $w/d$. A indicates global minima, M local minima and X local maxima. The global maximum lies at $w = 0$. Bcc is at $w/d = 1/3$, the $\omega$-phase at $w/d = 1/2$. The two vertical stripes labeled "L" and "Landau" respectively, indicate the regions where the Landau conditions for coexisting phases are fulfilled.

We conclude that the transformation from bcc to the $\omega$-phase can indeed be explained in the spirit of a Landau theory but a quantitative application fails since the prerequisites for the Landau theory are not fulfilled.
A more quantitative application of the Landau-Ginsburg theory in conjunction with the Born-von Kàrmán parameterization of the interactions should be possible. A better achievement, however, would be a three-dimensional analytical model of the shock waves and phase transitions which can also predict the transverse modulation.

## 6.8 Theoretical explanations of the solitary waves

We will first present a very crude model which simply claims that the solitary waves occur along the direction where the atoms have the shortest distance, and that the solitary waves are quasi-hard sphere collisions in the spirit of Nesterenko [145]. We have tested the model for different lattices and proved that it works for all cases where solitary waves have been observed up to now. But it cannot explain the solitary waves along arbitrary directions.
Second we will present a few analytical approaches that could be applied to the solitary wave phenomenon and discuss how these approaches have to be adapted and generalized.

**Crude model for the solitary waves**

The solitary waves can be understood in a crude model which assumes that they are caused by direct hits of close-neighbor quasi-hard spheres. The directions in bcc where the atoms form chains with distances of the potential radius $1a$ are exactly the three-fold axes. These chains are close-packed. In a characteristic soliton peak the distance between two atoms is reduced by 25%. The potential energy increases to about $21\epsilon$ which is large, and the interaction can be regarded as a hard collision (If the compression is 30% the energy grows to $70\epsilon$). If shocked along a four-fold or two-fold direction the momentum of the moving atom points directly into a gap between two atoms, and no direct collision partner is present. The increase in energy at the same displacement is only $4.3\epsilon$ for the four-fold direction. For the two-fold direction it is

negligible. Therefore the solitary waves cannot persist. The observation of the decay of the transverse correlation of the collisions would also be in agreement with this model. In the transverse direction a loss of correlation leads only to a small increase of the binding energy of the atoms.
In the tcp-structures the close-packed chains (dotted atoms in Figs. 3.8 - 3.10) are thinned out by the other black and white atoms which do not form close-packed chains. Therefore the solitary wave is also not stable in these phases if shocked perpendicular to the basic layers. In the plane of the basic tiles, in the quasicrystalline plane, and in the 45 degree directions there are no well-defined atomic layers at all, thus no solitary waves are expected.
We have to admit that this model cannot explain more complicated cases of solitary waves along high-index directions in bcc. It also misses the connection to the intermediate ω-phase, but it could be demonstrated that it applies also in other cases if we assume that the solitons there are of the same type as the ones described here: In fcc the solitary waves are found along the two-fold directions which are the close-packed chains. The model also works for a specially prepared single cubic crystal where the solitary waves can be switched on and off along the four-fold direction if the interaction is tuned such that it is strong along the four-fold or two-fold direction.

**Tunable solitary waves**

To figure out how reasonable this crude model is we have tried to generate solitary waves in single cubic (sc) crystals. Since the coordination number of sc crystals is only six, they are not stable with respect to shear distortion if isotropic potentials are used. Therefore we have introduced two sets of bonds: Nearest neighbors along the four-fold direction interact with one set, next nearest neighbors along the two-fold direction interact with the other set. We can tune the relative strength $r_s$ of these two sets of interactions. If the next nearest neighbor interactions are strong then the system behaves as if it would consist of two independent interpenetrating fcc crystals. The depth of the edge-connected atoms has been kept fixed at $v_e = -1\epsilon$, the strength for diagonal-connected atoms has been varied between $v_d = -0.25$ and $-4\epsilon$.
The results are the following: Along the four-fold direction solitary waves are observed for any value of $r_s$ as predicted by our crude model,

since these atoms always have the shortest distance. If the shock wave propagation is along two-fold direction we find solitary waves only for large $r_s$ as known from the fcc crystals [72] since in the case of large $r_s$ second nearest neighbors have direct contact. The cross-over occurs between $r_s = v_d/v_e = 0.5$ and 1.0. Shock waves along the three-fold direction never lead to solitary waves even in the case of extremely high piston velocities. These results nicely fit into the predictions of our crude model.

**Continuum approach**

The simplest description of solitary waves in one-dimensional shocked crystals involves Korteweg-de Vries (KdV) and Toda solitons [97]. Thus a natural extension would be the Kadomtsev-Petviashvili (KP) solitary waves [111], which are nonlinear along one direction and linear in the transverse directions. Moreover, these solitary waves include the KdV and Toda solitons as one-dimensional limits. There exist two varieties with positive (II) and negative dispersion (I) for the transverse part. The solitons of KPI equation behave indeed like our solitary waves, i.e. they decay into so-called bullets similar to what we have seen in Fig. 6.11. An application of this approach is currently far beyond the scope of this thesis since the general continuum case has not yet been treated (which has to be solved numerically), but in our case the more complicated discrete limit would be needed.

## 6.9 Discussion

### 6.9.1 Experiments

Experimentalists [114] are interested to observe the solitary wave peaks found in our simulations in single crystals in the picosecond range at low temperatures with the help of lasers. Although the possibility of detection seems to be rather limited due to the strong restrictions indicated above, there is a certain probability of success. Peter Lomdahl [114] has observed solitary waves in granular media on the oscilloscope along the hard directions in fcc and bcc. An experimental verification would certainly clear out the doubts about the existence of these phenomena.

### 6.9.2 Comparison to one-dimensional solitons

Holian et al. [102] have simulated shock waves in one-dimensional lattice models and described the results by analytical means [97]. For Toda interactions they could show that solitary wave trains exist. Morse and Lennard-Jones potentials can be treated as perturbations of the Toda interaction. The important parameter is the product $\alpha\nu$ of the relative anharmonicity $\alpha = -a_0\Phi'''(a_0)/\Phi''(a_0)/2$ of the potential $\Phi(r)$ at its minimum $a_0$ and the relative piston velocity $\nu = u_p/c$ with respect to the velocity of sound $c$. The entire shock profile may be described as a soliton wave train. If $\alpha\nu$ is small, the continuum KdV description can be applied and the discrete Toda description if it grows. Isolated solitons exist near the shock front. At small $u_p$ they separate logarithmically, at large $u_p$ they are locked in a periodic pattern. If one moves from the shock front to the piston, the phase between neighboring particles increases until it reaches $\pi$. Near the piston the particles are in an optical mode, their displacement is equal and opposite. The optical mode is the highest wave number which a discrete lattice can support. If $\alpha\nu$ is small the long time behavior is quasiharmonic, and hard-rod-like otherwise. The crucial point is that the system is one-dimensional which prevents plasticity since the particles cannot change their order. No dissipation is present. In three dimensions we have dissipation due to the possibility of transverse motion. A comparison of the predicted speed of the leading soliton $u_s/c = 1+2/3\alpha\nu$ for small amplitudes (weak shock waves) and $u_s/c = 2\alpha\nu/\ln(4\alpha\nu)$ for large amplitudes (stronger shock waves) with the propagation speed of our solitary waves shows that there is no agreement.

The one-dimensional results also hold in three dimensions if the shock strength is below the Hugoniot elastic limit, in the elastic-plastic regime, or if the temperature is zero [102, 95]. Then there are steady solitary waves locked-in to an oscillatory profile. Holian [95] claims that if the cross-section of the samples is too small, distortions will be locked out and lead to an ever-growing non-steady soliton profile. He is referring to Germann et al. [72]'s simulations in the elastic-plastic regime with cross-sections of up to $200 \times 200a^2$. We have observed non-steady solitary waves in the overdriven regime in samples with up to $120 \times 120a^2$. But we found that the averaged solitary waves are decaying by loosing the inter-chain correlation, while the solitary waves on a single atom

chain persisted. Our results can be compared to those of Kadau [119]. He studied bcc iron equipped with different sets of EAM potentials. In general his results are very similar to ours, at least for the three-fold direction. The solitary wave trains in his simulations seem to consist of more peaks than in our case, and to decay more slowly. A direct comparison, however, is lacking. In general his results are in good agreement with ours, but there are some notable differences:

1. No $\omega$-phase has been observed. The reason is unclear. Since we have shown that the $\omega$-phase and the solitary waves are two sides of the same phenomenon, and solitary waves have been observed in both cases, one should expect the $\omega$-phase in both systems.

   But it is certainly possible that another origin of the solitary waves exists.

2. A modulated $\omega$-phase is not present in iron since the softening occurs close to the ideal wave vector.

3. The solitary waves in Kadau et al.'s simulations are not modulated in the transverse direction. Since they do not loose their correlation they decay much slower. Our first conjecture was that the range of the interaction may be responsible for the different decay speed, but this cannot be the case since the interaction ranges are of comparable size. Other reasons might be the many-body part of the EAM-interaction or the low stability of bcc with the Dzugutov potential.

# Final Remarks

In this work we have demonstrated that the study of defects generated of shock waves is a challenging subject. Our results show once again that shock wave physics has made a huge leap with the introduction of massively parallel supercomputers and large-scale computing.

The treatment of the diatomic case has revealed that plasticity of ordinary crystals has to be studied in more detail. More detailed analysis methods are also required. The modes of plasticity turned out to be much more complicated than in the monatomic case. It would be preferable to compare the results to experiments. This is not possible yet since we have used model potentials. Currently we have a project running which aims to produce material-specific interactions for Laves crystals and Frank-Kasper quasicrystals starting from ab-initio calculations. These interactions will permit to study models with realistic properties and to compare them to experiment.

With regard to the quasicrystals we were able to demonstrate in the mono- and diatomic case that quasicrystal-specific defects are induced by the plastic precursor. It would be interesting to study shock waves in decagonal AlNiCo quasicrystals for which precise models and optimized interactions are available [5]. Equilibrium results have been obtained already [65, 66]. Simple modes of plasticity in quasicrystals, like dislocations or phason walls in the binary model, are no longer expected for Frank-Kasper quasicrystals since newer results on crack propagation have shown that no dislocations are emitted [159, 160], despite the possibility to generate dislocations under extreme conditions [185]. The issue of steady and non-steady waves and long-term relaxations which is much more severe for complex structures has not yet been addressed adequately and deserves a closer investigation.

The most controversial part of this thesis may be the solitary waves. Solitons generated by shock waves have long been a matter of debate. Meanwhile a picture has evolved which says that locked-in solitary waves are observed along certain directions in three-dimensional crystals. The case of non-steady solitary waves has not yet been settled. We are eager

to determine the possibility of experimental observations. In granular model systems they have been seen, but it would be more interesting to measure them on an atomic scale. The latest results by Kadau [118] predict that the solitary waves should still be detectable at low temperatures after traveling $1\mu m$ through a perfect single crystal.
For bcc-materials interacting with the Dzugutov potential and shocked along the three-fold direction we have shown that the solitary waves are the super-sonic continuation of a sub-sonic phase transition to the intermediate $\omega$-phase.
The solitons observed by Kadau [118] decay much slower than our solitary waves. The speculation goes that this is mainly due to the many-body part of interaction, and not to the range of interaction. We are preparing new simulations with modified interactions to solve this question.

# Future Perspectives

What are the next steps? Here we have collected a few ideas on how the research on shock waves in complicated crystal structures can be continued.

The synchroshear mechanism, predicted for the Laves crystals as a mode of plasticity, deserves a closer investigation. Specific EAM-interactions can help to clarify the question whether the Lennard-Jones potentials are responsible for the unsuccessful search or if there is a more general reason like the topology of the $\gamma$-surface for example.

For the quasicrystals, we plan to go back to two dimensions where the analysis and representation of the results is much easier. A two-dimensional binary model exists which permits the generation of dislocations and phason walls [178, 177] despite the fact that the model is also rather densely packed. In three dimensions we will soon be able to study stable icosahedral quasicrystals of the AlCuFe- or AlPdMn-type when the EAM-potentials become available. Precise models of these materials exists and dislocations and phason walls are well known from experiment. In conclusion we have not yet reached the end of the road in the study of shock waves in quasicrystals although the first results have suggested a close similarity between crystals and quasicrystals.

We have only shortly reported two studies of amorphous structures. It turned out that the Dzugutov potential is very suitable for the simulation of glasses since it prevents crystallization very effectively. The same is true for the set of parameters of the Lennard-Jones potentials in the diatomic case. A more thorough investigation of amorphous materials will be appropriate. Differences in the behavior of weak and strong shock waves have been found already but they could not be characterized in detail. New analysis tools are required and a closer look at the shock effects on the atomic structure level is necessary.

The analytical treatment of the solitary wave problem is still challenging. The first attempts to bring the discrete nature of the crystal lattice into connection with soliton equations had appeared to be tremendously

complicated. But the realization that an easier way may exist by employing the Born-von-Kármán formalism for the interactions has revived this topic again. At least for the short-ranged Dzugutov potential and the simple bcc-lattice the problem appears to be solvable and will be addressed soon.

The size of the simulated models has increased dramatically, but they are still far too small in many instances and can be simulated for a far to short time in several cases. Especially in the more realistic case of polycrystals no stationary state could be achieved [95] until now. Great hopes for improvement lie in the Hugoniostat which permits to decouple the simulation time and the propagation velocity of the shock waves since it allows to study a (quasi-)stationary system.

Another field of application has recently come into vision: the simulation of the laser ablation process. The interaction of lasers with solids is a very challenging and exciting subject. Shock waves are only a part of the complex processes observed there, but show up in the solid and in the plasma produced by the laser (See App. C). The simulation of laser ablation will require the interplay of different physical discipline like plasma physics, electron theory and solid state physics and the treatment of the problem with multi-scale methods. The electron system for example has to be modeled by finite element methods to capture the essentials of the heat and energy transfer to the atom system since the heat conduction of the electrons and the ions is very different.

# Appendix

## A The Mie-Grüneisen-Debye-theory

As long as no phase transition occurs, experiment and simulations obey the following astonishing relation between the piston velocity $u_p$ and the shock wave velocity $u_s$, valid in a broad range of piston velocities:

$$u_s = s\ u_p + c \quad (+k\ u_p^2 + \cdots). \tag{A.1}$$

In polycrystals, $c$ is the bulk velocity of sound and $s$ and $k$ are constants [180]. Usually $k$ is very small, and the linear relation is valid over a range of 40 Gbar to within 20% [189]! This indicates that the Grüneisen ratio $\gamma$ is a constant, since it is given by

$$\gamma = 2\ \frac{\mathrm{d}u_s}{\mathrm{d}u_p} - 1. \tag{A.2}$$

There is no solid theoretical foundation for this linearity, but an explanation is given by the Mie-Grüneisen-Debye theory (See [156] p. 40ff), which describes a solid as a collection of harmonic oscillators. The contribution of the electrons is neglected and the material is considered to be isotropic. Experience has shown that the Mie-Grüneisen-Debye theory works pretty well for solids at high temperatures.
With the given assumptions we can write down the thermal energy $E$, the pressure $P$ and the Grüneisen ratio $\nu_\alpha$ per mode by:

$$\begin{aligned} E &= \Phi + \frac{1}{2}\sum_\alpha h\nu_\alpha + \sum_\alpha \frac{h\nu_\alpha}{e^{h\nu_\alpha/kT}-1}, \quad \alpha = 1,\ldots,3N \\ P &= -\frac{\mathrm{d}\Phi}{\mathrm{d}V} + \frac{1}{V}\sum \gamma_\alpha \left\{ \frac{1}{2} h\nu_\alpha + \frac{h\nu_\alpha}{e^{h\nu_\alpha/kT}-1} \right\} \\ \gamma_\alpha &= -\mathrm{d}\ln\nu_\alpha / \mathrm{d}\ln V \end{aligned}$$

$\Phi$ is the ground state energy, $V$ the volume, $\nu_\alpha$ are the phonon modes. The ordinary Grüneisen ratio $\gamma$ is given as an average over all $\gamma_\alpha$.

The pressure may be represented by:

$$P = -\frac{\mathrm{d}\phi}{\mathrm{d}V} + \gamma\frac{3NkT}{V}. \tag{A.3}$$

After some rewriting, this gives the Mie-Grüneisen equation of state [136, 79, 80]

$$P - P_K = \frac{\gamma(V)}{V}(E - E_K) \tag{A.4}$$

where the index $K$ means pressure and energy at the starting point, usually ambient conditions.
The constant $\gamma$ for an elastic continuum can be derived with Slater's assumptions [197] of an isotropic body and a constant Poisson ratio $(c_{11}/c_{12})$:

$$\gamma = -\frac{V}{2}\frac{(\partial^2 P/\partial V^2)}{(\partial P/\partial V)} - \frac{2}{3}. \tag{A.5}$$

Slater's result follows from the usual equations

$$\begin{aligned} c_l &= \sqrt{V c_{11}} \\ c_t &= \sqrt{\frac{(c_{11}-c_{12})V}{2}} \\ -V\frac{dP}{dV} &= \frac{c_{11}+2c_{12}}{3} \end{aligned}$$

for the longitudinal and transversal velocity of sound and the bulk modulus of an isotropic body, together with the relation $\nu_\alpha = c/\lambda_\alpha$, where $\lambda_\alpha \propto V^{1/3}$ leads to $\gamma_\alpha$ being all equal.
For the longitudinal mode in particular we get

$$\gamma = \frac{1}{2}\frac{\mathrm{d}\ln c_{11}}{\mathrm{d}\ln V} - \frac{1}{6}. \tag{A.6}$$

and together with Slater's formula for $\gamma$ at $P = 0$:

$$\gamma = 2s - 1,\ s = \mathrm{d}u_s/\mathrm{d}u_p \tag{A.7}$$

Other derivations, assuming different equations of state are also possible. Dugdale and MacDonald [47] for example give an improved relation:

$$\gamma = -\frac{V}{2}\frac{(\partial^2(PV^{2/3})/\partial V^2)}{(\partial(PV^{2/3})/\partial V)} - \frac{1}{3} \tag{A.8}$$

Although their original derivation was wrong, the formula gives excellent results. Meanwhile it has been obtained by an alternative deduction (for example [144]).

# B Shock waves in one-dimensional crystals and quasicrystals

Shock waves in one-dimensional hard-sphere structures have been studied by Holian and Straub [102,204]. The model applied is equivalent to the "beads on a wire" model of Duvall and Band [25]. Rabie [36] treats the "bead on a string" model, a generalization to inelastic scattering.
Spheres of diameter $\sigma$ and distance $a$ are placed on a regular lattice. If a further sphere is colliding with this arrangement at a constant velocity $u_p$ then the shock velocity can be calculated easily by geometric means (Fig. B.1, left). It is helpful in this context to define a collision time $t_c = (a - \sigma)/2u_p$ and to express the shock velocity by $u_s = a/t_c = 2u_p/(1 - \sigma/a)$.
The scheme can easily be extended to "quasicrystals" built with two distances $l$ and $s$ in an aperiodic arrangement like for example a Fibonacci sequence (Fig. B.1, right). An inspection of the figure shows that one has only to replace the distance $a$ by the average $\overline{a} = n_l l + n_s s$, $n_l$ and $n_s$ being the frequency of the $l$ and $s$ distances. This method can certainly be applied to more complicated structures with a well-defined average.

# C Ablation and generation of shock waves with lasers

Laser ablation is a method of great technological relevance which is still being developed. To understand the physical processes and to optimize ablation, a modeling with computer simulations is urgently required.
In laser ablation there are several time scales which last up to seconds. Excitingly, the shortest time scales can be assessed directly by molecular dynamics. Often the timescales and sizes treatable by molecular dynamics are short and small compared to their true orders of magnitude. This

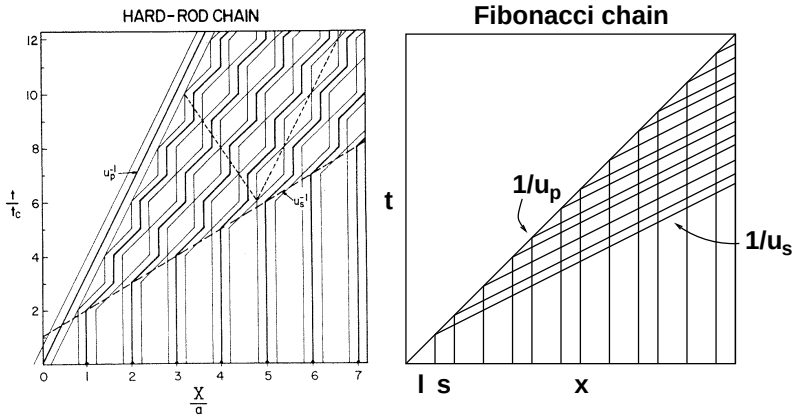


**Figure B.1:** Shock waves in one-dimensional hard sphere materials. Left: ordinary crystal (From [102]), right: quasicrystal, drawn for $\sigma = 0$. Each crossing denotes the collision of two particles.

is not the case for short-time laser ablation with femtosecond pulses as can be read of the following list (data for example from [12, 55, 225]):

- laser power: $10^8 - 10^{18}$ W/cm$^2$
- pulse interval: 100 fs – 10 ns
- pulse duration: 10 fs – 100 $\mu$s
- heating: 3000 K – 10000 K
- pressure: 1 GPa – 2 TPa
- penetration depth: 100 – 300 nm
- observation time: few ps – ns

The numbers should be compared to typical sample sizes: In the simulations we used rods with up to $120 \times 120 \times 600a^3$ (average atom distance $a$) and up to 5 million atoms. The achievable simulation time is about 100 ps. These numbers are not dictated by computing power but by practical purposes. It would be no problem to simulate samples with up to 5 billion atoms [173]. We will not conceal, however, that there is one

aspect which has not been treated adequately, namely the laser spot is a thousand times larger than the cross section treated up to now. But such large samples are in the range of present day computers.
Laser ablation is a huge challenge even in the most simple case of metals: The interaction of the laser with the electron system and the coupling of the electrons and the ions have to be modeled. The process usually takes place in the phase coexistence region of the phase diagram such that single atoms, liquid drops and solid clusters play a role in the ablated material. Shock waves moving out of the sample may be modeled with continuum methods. Our special concern are shock waves moving into the sample through highly stressed material where they interact with dislocations and other extended defects.

# Bibliography


[1] T. J. Ahrens, Equation of state, in *High-Pressure Shock Compression of Solids* (Edited by J. Asay and M. Shahinpoor), volume 1, pages 75–113, Springer, New York, (1993).

[2] R. Ahuja, J. M. Wills, B. Johansson, and O. Eriksson, Crystal structures of Ti, Zr, and Hf under compression: Theory, *Phys. Rev. B* **48** (1993) 16269–16279.

[3] Y. Akahama, Y. Mori, H. Kawamura, K. Kimura, and S. Takeuchi, Pressure-induced phase transformation of quasicrystals, in *Proceedings of the XIII AIRAPT conference: Recent trends in high pressure research*, volume 13, pages 156–158. Pergamon Press, Oxford, (1991).

[4] Y. Akahama, Y. Mori, M. Kobayashi, H. Kawamura, K. Kimura, and S. Takeuchi, Pressure-induced amorphization of quasi crystals, *J. Phys. Soc. Jpn.* **58** (1989) 2231–2234.

[5] I. Al-Lehyani, M. Widom, Y. Wang, N. Moghadam, G. M. Stocks, and J. A. Moriarty, Transition-metal interactions in aluminum-rich intermetallics, *Phys. Rev. B* **64** (2001) 075109.

[6] D. Alfe, M. J. Gillan, L. Vočadlo, J. Brodholt, and G. D. Price, The ab initio simulation of the Earth's core, *Proc. R. Soc. London, Ser. A* **360** (2002) 1227–1244.

[7] S. I. Anisimov, V. V. Zhakhovskiĭ, and V. E. Fortov, Shock wave structure in simple liquids, *JETP Lett.* **65** (1997) 755–761.

[8] J. R. Asay and L. C. Chhabildas, Paradigms and challenges in shock wave research, in *High-Pressure Shock Compression of Solids* (Edited by Y. Horie, L. Davison, and N. N. Thadhani), volume 6, pages 57–119, Springer, New York, (2002).

[9] J. R. Asay and M. Shahinpoor, A chronological bibliography on shock compression of solids, in *High-Pressure Shock Compression of Solids* (Edited by J. Asay and M. Shahinpoor), volume 1, pages 361–376, Springer, New York, (1993).

[10] M. Audier and P. Guyot, Microcrystalline AlFeCu phase of pseudo icosahedral symmetry, in *Quasicrystals* (Edited by M. Jaric and S. Lundqvist), pages 74–91, World Scientific Singapore, (1990).

[11] R. R. Balokhonov, P. A. Makarov, V. A. Romanova, and I. Yu.Smolin, Simulation of crystal plasticity under dynamic loading, *Comp. Mat. Sci.* **16** (1999) 355–361.

[12] D. Batani, A. Balducci, D. Beretta, A. Bernardinello, T. Löwer, M. Koenig, A. Benuzzi, B. Faral, and T. Hall, Equation of state data for gold in the pressure range $< 10$ TPa, *Phys. Rev. B* **61** (2000) 9287–9294.

[13] S. S. Batsanov, Changing atomic structure by shock compression, in *Effects of Explosions on Materials*, pages 99–116, Springer, New York, (1994).

[14] S. S. Batsanov, Foundations of the physics of shock waves, in *Effects of Explosions on Materials*, pages 1–45, Springer, New York, (1994).

[15] S. S. Batsanov, Mechanical characteristics and microstructural changes in solids under shock compression, in *Effects of Explosions on Materials*, pages 66–98, Springer, New York, (1994).

[16] A. B. Belonoshko, Atomistic simulations of shock wave-induced melting of argon, *Science* **275** (1997) 955–957.

[17] A. B. Belonoshko, Response: Atomistic simulations of shock wave-induced melting of argon, *Science* **278** (1997) 1475–1476.

[18] G. Ben-Dor, O. Igra, and T. Elperin, editors, *Handbook of Shock Waves*, Academic Press, San Diego, (2001).

[19] H. A. Bethe, On the theory of shock waves for an arbitrary equation of state, in *Classical Papers in Shock Compression Science* (Edited by Johnson and Chéret), pages 421–492, Springer, New York, (1998).

[20] E. Bitzek, F. Gähler, J. Hahn, C. Kohler, G. Krdzalic, J. Roth, C. Rudhart, G. Schaaf, J. Stadler, and H.-R. Trebin, Recent developements in IMD: Interactions for covalent and metallic systems, in *High Performance Computing in Science and Engineering 2000* (Edited by E. Krause and W. Jäger), pages 37–47, Springer, Heidelberg, (2001).

[21] J. C. Boettger and D. C. Wallace, Metastability and dynamics of the shock-induced phase transition in iron, *Phys. Rev. B* **55** (1997) 2840–2849.

[22] B. Borie, S. L. Sass, and A. Andersen, The short-range structure of Ti and Zr b.c.c. solid solutions containing the $\omega$ phase. I. general diffraction theory and development of computational techniques, *Acta Crystallogr. Sect. A* **29** (1973) 585–594.

[23] B. Borie, S. L. Sass, and A. Andersen, The short-range structure of Ti and Zr b.c.c. solid solutions containing the $\omega$ phase. II. solution of the structure determination, *Acta Crystallogr. Sect. A* **29** (1973) 594–602.

[24] M. Born and K. Huang, *Dynamical Theory of Crystal Lattices*, Clarendon Press, Oxford, (1954).

[25] M. B. Boslough and J. R. Asay, Basic principles of shock compression, in *High-Pressure Shock Compression of Solids* (Edited by J. Asay and M. Shahinpoor), volume 1, pages 7–42, Springer, New York, (1993).

[26] E. M. Bringa, B. D. Wirth, M. J. Caturla, J. Stölken, and D. Kalantar, Metals far from equilibrium: From shocks to radiation damage, *Nucl. Instrum. & Methods B* **202** (2003) 56–63.

[27] E. Cockayne and M. Mihalkovič, Stable quasicrystalline sphere packing, *Phil. Mag. Lett.* **79** (1999) 441–448.

[28] C. S. Coffey, Mechanisms of elastoplastic response of metals to impact, in *High-Pressure Shock Compression of Solids* (Edited by L. Davison and M. Shahinpoor), volume 3, pages 59–80, Springer, New York, (1998).

[29] H. E. Cook, On the nature of the omega transformation, *Acta Metall.* **21** (1973) 1445–1449.

[30] H. E. Cook, A theory of the omega transformation, *Acta Metall.* **22** (1974) 239–247.

[31] H. E. Cook, On first-order structural phase transitions – I. general considerations of pre-transition and nucleation phenomena, *Acta Metall.* **23** (1975) 1027–1039.

[32] H. E. Cook, On first-order structural phase transitions – II. the omega transformation in Zr-Nb alloys, *Acta Metall.* **23** (1975) 1041–1054.

[33] H. E. Cook and D. D. Fontaine, On the elastic free energy of solid sulutions – I. microscopic theory, *Acta Metall.* **17** (1969) 915–924.

[34] W. C. Davis, Shock waves; rarefaction waves; equation of state, in *Explosive Effects and Applications* (Edited by J. A. Zukas and W. P. Walters), pages 47–113, Springer, New York, (1998).

[35] L. Davison, Attenuation of longitudinal elastoplastic pulses, in *High-Pressure Shock Compression of Solids* (Edited by L. Davison and M. Shahinpoor), volume 3, pages 277–327, Springer, New York, (1998).

[36] L. Davison, The discontinuous shock–fact or fancy?, in *High-Pressure Shock Compression of Solids* (Edited by Y. Horie, L. Davison, and N. N. Thadhani), volume 6, pages 297–321, Springer, New York, (2002).

[37] L. Davison, The universal role of turbulence in the propagation of strong shocks and detonation waves, in *High-Pressure Shock Compression of Solids* (Edited by Y. Horie, L. Davison, and N. N. Thadhani), volume 6, page 1, Springer, New York, (2002).

[38] L. Davison and R. A. Graham, Shock compression of solids, *Phys. Rep.* **55** (1979) 255–379.

[39] M. Deza and M. Shtogrin, Isometric embedding of mosaics into cubic lattices, *Discr. Math.* **244** (2002) 43–54.

[40] C. Dilger, R. Mikulla, J. Roth, and H.-R. Trebin, Simulation of shear stress in icosahedral quasicrystals, *Phil. Mag. A* **75** (1997) 425–441.

[41] V. P. Dmitriev, S. B. Rochal, Y. Gufan, and P. Toledano, Definition of a transcendental order parameter for reconstructive phase transitions, *Phys. Rev. Lett.* **60** (1988) 1958–1961.

[42] J. P. K. Doye and D. J. Wales, Polytetrahedral clusters, *Phys. Rev. Lett.* **86** (2001) 5719–5772.

[43] J. P. K. Doye, D. J. Wales, and S. I. Simdyankin, Global optimization and the energy landscapes of dzugutov clusters, *Farad. Discuss.* **118** (2001) 159–170.

[44] V. V. Dremov, A. L. Kutepov, A. V. Petrovtsev, and A. T. Sapozhnikov, Equation of state and phase diagram of iron, in *Shock Compression of Condensed Matter - 2001* (Edited by M. D. Furnish, N. N. Thadhani, and Y. Horie), volume 620, pages 87–90, (2001).

[45] B. Dubost, J. M. Tanaka, P. Sainfort, and M. Audier, Large AlCuLi single quasicrystals with triacontahedral solidification morphology, *Nature* **324** (1986) 48–50.

[46] L. S. Dubrovinsky, Comment: Atomistic simulations of shock wave-induced melting of argon, *Science* **278** (1997) 1474–1475.

[47] J. S. Dugdale and D. K. C. MacDonald, The thermal expansion of solids, *Phys. Rev.* **89** (1953) 832–834.

[48] G. E. Duvall and R. A. Graham, Phase transitions under shock-wave loading, *Rev. Mod. Phys.* **49** (1977) 523–579.

[49] M. Dzugutov, Glass formation in a simple monoatomic liquid with icosahedral inherent local order, *Phys. Rev. A* **46** (1992) R2984 R2987.

[50] M. Dzugutov, Formation of a dodecagonal quasicrystalline phase in a simple monatomic liquid, *Phys. Rev. Lett.* **70** (1993) 2924–2927.

[51] M. Dzugutov, Hopping diffusion as a mechanism of relaxation stretching in a stable simple monatomic liquid, *Europhys. Lett.* **26** (1994) 533–538.

[52] M. Dzugutov, Phason dynamics and atomic transport in an equilibrium dodecagonal quasi-crystal., *Europhys. Lett.* **31** (1995) 95–100.

[53] M. Dzugutov and U. Dahlborg, Molecular dynamics study of the coherent density correlation function in a supercooled simple one-component liquid, *J. Non-Cryst. Solids* **131** (1991) 62–65.

[54] M. Dzugutov, S. I. Simdyankin, and F. H. Zetterling, Decoupling of diffusion from structural relaxation and spatial heterogeneity in a supercooled simple liquid, *Phys. Rev. Lett.* **89** (2002) 195701.

[55] K. Eidmann, J. Meyer-ter-Vehn, T. Schlegel, and S. Hüller, Hydrodynamic simulation of subpicosecond laser interaction with solid-density matter, *Phys. Rev. E* **62** (2000) 1202–1214.

[56] M. L. Elert, S. V. Zybin, and C. T. White, Molecular dynamics study of shock-induced chemistry in small condensed-matter hydrocarbons, *J. Chem. Phys.* **118** (2003) 9795–9801.

[57] A. G. Every, Ballistic phonons and the shape of the ray surface in cubic crystals, *Phys. Rev. B* **24** (1981) 3456–3467.

[58] C. Falter, A unifying approach to lattice dynamical and electronic properties of solids, *Phys. Rep.* **164** (1988) 1–117.

[59] C. Falter, W. Ludwig, M. Selmke, and W. Zierau, The LA-$\frac{2}{3}(1,1,1)$ anomaly in bcc structure, *Phys. Lett.* **90A** (1982) 250–252.

[60] C. Falter, W. Ludwig, W. Zierau, and M. Selmke, A model case study of the LA-$\frac{2}{3}(1,1,1)$ anomaly in bcc structure, *Phys. Lett.* **93A** (1983) 298–302.

[61] D. D. Fontaine, Mechanical instabilities in the b.c.c. lattice and the beta to omega phase transformation, *Acta Metall.* **18** (1970) 275–279.

[62] D. D. Fontaine, Simple models for the omega phase transformation, *Metall. Trans. A* **19** (1988) 169–175.

[63] D. D. Fontaine and O. Buck, A Monte Carlo simulation of the omega phase transformation, *Phil. Mag.* **71** (1973) 967–983.

[64] D. D. Fontaine and R. Kikuchi, Bragg-Williams and other models of the omega phase transformation, *Acta Metall.* **22** (1974) 1139–1146.

[65] F. Gähler and S. Hocker, Atomic dynamics in decagonal Al-Ni-Co quasicrystals, *J. Non-Cryst. Solids* **334-335** (2004) 308–311.

[66] F. Gähler, S. Hocker, U. Koschella, J. Roth, and H.-R. Trebin, Phason elasticity and atomic dynamics of quasicrystals, in *Quasicrystals: Structure and Physical Properties* (Edited by H.-R. Trebin), pages 338–358, Wiley-VCH, (2003).

[67] F. Gähler, C. Kohler, J. Roth, and H.-R. Trebin, Strain distributions in quantum dot nanostructures, in *High Performance Computing in Science and Engineering 2002* (Edited by E. Krause and W. Jäger), pages 3–14, Springer Heidelberg, (2002).

[68] J. E. Garcés, G. B. Grad, A. F. Guillermet, and S. J. Sferco, Theorectical study of the structural properties and thermodynamic stability of the omega phase in the 4d-transition series, *J. All. Comp.* **289** (1999) 1–10.

[69] T. C. Germann, A short history of shock wave simulations of solids, CECAM Workshop on Atomistic modeling of materials at extreme conditions: experimental validation of atomistic modeling, Lyon 2004.

[70] T. C. Germann, Large-scale molecular dynamics simulations of shock-induced plasticity, phase transformations, and detonation, in *Shock Compression of Condensed Matter - 2001* (Edited by M. D. Furnish, N. N. Thadhani, and Y. Horie), volume 620, pages 333–338, (2001).

[71] T. C. Germann, B. L. Holian, and P. S. Lomdahl, Plastic deformation in shock waves via molecular-dynamics simulations, in *Shock Compression of Condensed Matter - 1999* (Edited by M. D. Furnish, L. C. Chhabildas, and R. S. Hixson), volume 505, pages 297–300, (1999).

[72] T. C. Germann, B. L. Holian, P. S. Lomdahl, and R. Ravelo, Orientation dependence in molecular dynamics simulations of shocked single crystals, *Phys. Rev. Lett.* **84** (2000) 5351–5354.

[73] T. C. Germann, D. Tanguy, B. L. Holian, P. S. Lomdahl, M. Mareschal, and R. Ravelo, Dislocation structure behind a shock front in fcc perfect crystals: atomistic simulation results, *Minerals, Metals & Mater. Society and ASM Int. Metallurgical & Mater. Transactions A-Physical Metallurgy & Mater. Sci* **35 A** (2004) 2609–2615.

[74] J. J. Gilman, Responses of condensed matter to impact, in *High-Pressure Shock Compression of Solids* (Edited by Y. Horie, L. Davison, and N. N. Thadhani), volume 6, pages 279–296, Springer, New York, (2002).

[75] R. A. Graham, Basic concepts and models, in *Solids under High-Pressure Shock Compression: Mechanics, Physics and Chemistry*, pages 15–52, Springer, New York, (1993).

[76] R. A. Graham, Introduction, in *Solids under High-Pressure Shock Compression: Mechanics, Physics and Chemistry*, pages 1–12, Springer, New York, (1993).

[77] R. A. Graham, Introduction to high-pressure shock compression of solids, in *High-Pressure Shock Compression of Solids* (Edited by J. Asay and M. Shahinpoor), volume 1, pages 1–6, Springer, New York, (1993).

[78] R. A. Graham, Physical properties under elastic-plastic compression, in *Solids under High-Pressure Shock Compression: Mechanics, Physics and Chemistry*, pages 97–138, Springer, New York, (1993).

[79] E. Grüneisen, Theorie des festen Zustands einatomiger Elemente, *Ann. Phys.* **39** (1912) 257–306.

[80] E. Grüneisen, Zustand des festen Körpers, in *Handbuch der Physik* (Edited by H. Geiger and K. Scheel), volume X, pages 1–59, Springer, Berlin, (1926).

[81] J. Hahn and H.-R. Trebin, Molecular dynamics of covalent crystals, in *High Performance Computing in Science and Engineering 1999* (Edited by E. Krause and W. Jäger), pages 92–99, Springer, Heidelberg, (2000).

[82] P. M. Hazzledine and P. Pirouz, Synchroshear transformations in laves phases, *Scr. Mat. Metall.* **28** (1993) 1277–1282.

[83] L. R. F. Henderson, General laws of propagation of shock waves through matter, in *Handbook of Shock Waves* (Edited by G. Ben-Dor, O. Igra, and T. Elperin), volume 1, pages 143–183, Academic, New York, (2001).

[84] C. L. Henley, Sphere packings and local environments in Penrose tilings, *Phys. Rev. B* **34** (1986) 797–816.

[85] C. L. Henley, Progress on the atomic structure of quasicrystals, in *Quasicrystals* (Edited by T. Fujiwara and T. Ogawa), pages 38–47. Springer Berlin, (1990).

[86] C. L. Henley, Cell geometry for cluster-based quasicrystal models, *Phys. Rev. B* **43** (1991) 993–1020.

[87] C. L. Henley and V. Elser, Quasicrystal structure of $(Al, Zn)_{49}Mg_{32}$, *Phil. Mag. B* **53** (1986) L59 L66.

[88] F. Hippert and D. Gratias, editors, *Lectures on Quasicrystals*. Les Editions de Physique, Les Ulis, (1994).

[89] J. P. Hirth, R. G. Hoagland, B. L. Holian, and T. C. Germann, Shock relaxation by strain induced martensitic phase transition, *Acta Mater.* **47** (1999) 2409–2415.

[90] K.-M. Ho, C.-L. Fu, and B. N. Harmon, Microscopic analysis of interatomic forces in transition metals with lattice distortion, *Phys. Rev. B* **28** (1983) 6687–6694.

[91] K.-M. Ho, C. L. Fu, and B. N. Harmon, Vibrational frequencies via total-energy calculations. applications to transition metals, *Phys. Rev. B* **29** (1984) 1575–1587.

[92] M. Hohl, J. Roth, and H.-R. Trebin, Correlation functions and the dynamical structure factor of quasicrystals, *Eur. Phys. J. B* **71** (2000) 595–601.

[93] B. L. Holian, Modeling shock-wave deformation via molecular dynamics, *Phys. Rev. A* **37** (1988) 2562–2568.

[94] B. L. Holian, Atomistic computer simulations of shock waves, *Shock Waves* **5** (1995) 149–157.

[95] B. L. Holian, What is a shock wave ? - The view from the atomic scale, in *High-Pressure Shock Compression of Solids* (Edited by Y. Horie, L. Davison, and N. N. Thadhani), volume 6, pages 149–168, Springer, New York, (2002).

[96] B. L. Holian, Molecular dynamics comes of age for shockwave research, *Shock Waves* **13** (2004) 489–495.

[97] B. L. Holian, H. Flaschka, and D. W. McLaughlin, Shock waves in the Toda lattice: Analysis, *Phys. Rev. A* **24** (1981) 2595–2623.

[98] B. L. Holian, T. C. Germann, P. S. Lomdahl, J. E. Hammerberg, and R. Ravelo, Shock waves and their aftermath: a view from the atomic scale, in *Shock Compression of Condensed Matter - 1999* (Edited by M. D. Furnish, L. C. Chhabildas, and R. S. Hixson), volume 505, pages 185–188, (1999).

[99] B. L. Holian, J. E. Hammerberg, and P. S. Lomdahl, The birth of dislocations in shock waves and high-speed friction, *J. Comput.-Aided Mat. Design* **5** (1998) 207–224.

[100] B. L. Holian, W. G. Hoover, B. Moran, and G. K. Straub, Shock-wave structure via non-equilibrium molecular dynamics and Navier-Stokes continuum mechanics, *Phys. Rev. A* **22** (1980) 2798–2808.

[101] B. L. Holian and P. S. Lomdahl, Plasticity induced by shock waves in nonequilibrium molecular-dynamics simulations, *Science* **280** (1998) 2085–2088.

[102] B. L. Holian and G. K. Straub, Molecular dynamics of shock waves in one-dimensional chains, *Phys. Rev. B* **18** (1978) 1593–1608.

[103] B. L. Holian and G. K. Straub, Molecular dynamics of shock waves in three-dimensional solids: transition from non-steady to steady waves in perfect crystals and implications for the Rankine-Hugoniot conditions, *Phys. Rev. Lett.* **43** (1979) 1598–1600.

[104] W. G. Hoover, Structure of a shock-wave front in a liquid, *Phys. Rev. Lett.* **42** (1979) 1531–1534.

[105] B. Horovitz, J. L. Murray, and J. A. Krumhansl, Stacking solitons in $\omega$-phase systems and quasielastic scattering, *Phys. Rev. B* **18** (1978) 3549–3558.

[106] L. M. Hsiung and D. H. Lassila, Shock-induced deformation twinning and omega transformation in tantalum and tantalum-tungsten alloys, *Acta Mater.* **48** (2000) 4851–4865.

[107] H. Hugoniot, On the propagation of motion in bodies and in perfect gases in particular I, in *Classical Papers in Shock Compression Science* (Edited by Johnson and Chéret), pages 161–244, Springer, New York, (1998).

[108] H. Hugoniot, On the propagation of motion in bodies and in perfect gases in particular II, in *Classical Papers in Shock Compression Science* (Edited by Johnson and Chéret), pages 244–358, Springer, New York, (1998).

[109] P. H. Hugoniot, Mémoire sur la propagation du mouvement dans les orps et plus spécialement dans les gaz parfaits. 1ê partie, *J. Ecole Polytech. (Paris)* **57** (1887) 3–97.

[110] P. H. Hugoniot, Mémoire sur la propagation du mouvement dans les orps et plus spécialement dans les gaz parfaits. 2ê partie, *J. Ecole Polytech. (Paris)* **59** (1889) 1–125.

[111] E. Infeld and G. Rowlands, Soliton metamorphosis, in *Nonlinear Waves, Solitons and Chaos*, pages 296–359, Cambridge University Press, Cambridge, (2000).

[112] C. Janot, *Quasicrystals: A Primer*, Clarendon Press (Oxford), (1994).

[113] J. N. Johnson, Micromechanical considerations in shock compression of solids, in *High-Pressure Shock Compression of Solids* (Edited by J. Asay and M. Shahinpoor), volume 1, pages 217–264, Springer, New York, (1993).

[114] K. Kadau, Experimental investigations of solitary waves, private communication.

[115] K. Kadau, *Moleculardynamik-Simulationen von strukturellen Phasenumwandlungen in Festkörpern, Nanopartikeln und ultradünnen Filmen*, Ph.D. thesis, Gesamthochschule Duisburg, (2001).

[116] K. Kadau, T. C. Germann, P. S. Lomdahl, and B. L. Holian, Shock-induced structural phase transformations studied by large-scale molecular-dynamics simulations, in *Shock Compression of Condensed Matter - 2001* (Edited by M. D. Furnish, N. N. Thadhani, and Y. Horie), volume 620, pages 351–355, (2001).

[117] K. Kadau, T. C. Germann, P. S. Lomdahl, and B. L. Holian, Microscopic view of structural phase transitions induced by shock waves, *Science* **296** (2002) 1681–1684.

[118] K. Kadau, T. C. Germann, P. S. Lomdahl, and B. L. Holian, Atomistic simulations of shock-induced transformations and their orientation dependence in bcc Fe single crystals, *Phys. Rev. B* **72** (2005) 064120.

[119] K. Kadau, T. C. Germann, P. S. Lomdahl, B. L. Holian, and F. J. Cherne, Atomistic simulations of shock-induced phase transitions, in *Shock Compression of Condensed Matter - 2003* (Edited by M. D. Furnish, N. N. Thadhani, and Y. Horie), volume 706, pages 229–234, (2004).

[120] A. M. Kimura, K. Sasamori, and A. Inoue, Formation, microstructure and mechanical properties of Al-Fe base quasicrystalline alloys, *Mater. Sci. Eng. A* **294-296** (2000) 168–172.

[121] U. Koschella, F. Gähler, J. Roth, and H.-R. Trebin, Phason elastic constants of a binary tiling quasicrystal, *J. All. Comp.* **342** (2002) 287–290.

[122] P. Kramer and R. Neri, Non-periodic central space filling with icosahedral symmetry using copies of seven elementary cells, *Acta Crystallogr. Sect. A* **38** (1982) 257–264.

[123] P. Krehl, History of shock waves, in *Handbook of Shock Waves* (Edited by G. Ben-Dor, O. Igra, and T. Elperin), volume 1, pages 1–142, Academic, New York, (2001).

[124] F. Lançon and L. Billard, Thermodynamical Properties of a Two-Dimensional Quasicrystal from Molecular Dynamics Calculations, *Europhys. Lett.* **2** (1986) 625–629.

[125] J. Lee, The universal role of turbulence in the propagation of strong shocks and detonation waves, in *High-Pressure Shock Compression of Solids* (Edited by Y. Horie, L. Davison, and N. N. Thadhani), volume 6, pages 121–148, Springer, New York, (2002).

[126] A. Lindbaum, E. Gratz, and S. Heathman, Pressure-induced order-disorder transitions in $RNi_2$ compounds, *Phys. Rev. B* **65** (2002) 134114.

[127] R. A. MacDonald and D. H. Tsai, Molecular dynamical calculations of energy transport in crystalline solids, *Physics Reports* **46** (1978) 1–41.

[128] J.-B. Maillet and S. Bernard, Uniaxial hugoniostat: method and applications, in *Shock Compression of Condensed Matter - 2001* (Edited by M. D. Furnish, N. N. Thadhani, and Y. Horie), volume 620, pages 367–377, (2002).

[129] J.-B. Maillet, M. Mareschal, L. Soulard, R. Ravelo, P. S. Lomdahl, T. C. Germann, and B. L. Holian, Uniaxial hugoniostat: a method for atomistic simulations of shocked materials, *Phys. Rev. E* **63** (2000) 016121.

[130] P. V. Makarov, Localized deformation and fracture of polycrystals at mesolevel, *Theo. Appl. Frac. Mech.* **33** (2000) 23–30.

[131] P. V. Makarov and V. A. Romanova, Mesoscale plastic flow generation and development for polycrystals, *Theo. Appl. Frac. Mech.* **33** (2000) 1–7.

[132] T. Mashimo, Shock compression of ceramic materials: yielding properties, in *High-Pressure Science and Technology – 1993* (Edited by S. C. Schmidt, J. W. Shaner, and M. Ross), volume 309, pages 757–760, (1994).

[133] T. Mashimo, Effects of shock compression on ceramic materials, in *High-Pressure Shock Compression of Solids* (Edited by L. Davison and M. Shahinpoor), volume 3, pages 101–146, Springer, New York, (1998).

[134] M. A. Meyers, F. Gregori, B. K. Kad, M. S. Schneider, D. H. Kalantar, B. A. Remington, J. S. Wark, T. Boehly, and G. Ravichandran, Plastic deformation in laser-induced shock compression of monocrystalline copper, in *Shock Compression of Condensed Matter - 2001* (Edited by M. D. Furnish, N. N. Thadhani, and Y. Horie), volume 620, pages 619–622, (2001).

[135] M. A. Meyers and L. E. Murr, Defect generation in shock wave deformation, in *Shock Waves and High Strain Rate Phenomena in Metals* (Edited by L. E. Murr and M. A. Meyers), pages 487–530, Plenum, New York, (1981).

[136] G. Mie, Zur kinetischen Theorie der einatomigen Körper, *Ann. Phys.* **11** (1903) 657–697.

[137] R. Mikulla, P. Gumbsch, and H.-R. Trebin, Dislocations in quasicrystals and their interaction with cluster-like obstacles, *Phil. Mag. Lett.* **78** (1998) 369–376.

[138] R. Mikulla, F. Krul, P. Gumbsch, and H.-R. Trebin, Numerical simulations of dislocation motion and crack propagation in quasicrystals, in *New Horizons in Quasicrystals: Research and Applications* (Edited by A. I. Goldman, D. J. Sordelet, P. A. Thiel, and J. M. Dubois), pages 200–207. World Scientific, (1997).

[139] R. Mikulla, J. Roth, and H.-R. Trebin, Simulation of shear stress in two-dimensional decagonal quasicrystals, *Phil. Mag. B* **71** (1995) 981–989.

[140] R. Mikulla, J. Stadler, F. Krul, H.-R. Trebin, and P. Gumbsch, Crack Propagation in Quasicrystals, *Phys. Rev. Lett.* **81** (1998) 3163–3166.

[141] M. A. Mogilevski, Mechanism of deformation under shock loading, in *Shock Waves and High Strain Rate Phenomena in Metals* (Edited by L. E. Murr and M. A. Meyers), pages 531–546, Plenum, New York, (1981).

[142] Y. Mori, Y. Akahama, M. Kobayashi, H. Kawamura, K. Hamada, and M. Motoyama, X-ray diffraction analysis of icosahedral phase under high pressures, *J. Phys. Soc. Jpn.* **58** (1989) 1482–1483.

[143] W. J. Murri, D. R. Curran, C. F. Petersen, and R. C. Crewdson, Response of solids to shock waves, in *High Pressure Physics and chemistry* (Edited by R. S. Bradley), volume 2, pages 1–163, Academic Press, New York, (1963).

[144] K. Nagayama, Theory of shock waves, in *Handbook of Shock Waves* (Edited by G. Ben-Dor, O. Igra, and T. Elperin), volume 1, pages 315–338, Academic, New York, (2001).

[145] V. Nesterenko, Nonlinear impulses in particulate materials, in *Dynamics of Heterogeneous Materials*, page 1, Springer, New York, (2001).

[146] Y. Noda, Y. Yamada, and S. M. Shapiro, Lattice dynamics of quenched diffuse $\omega$ phase in $Zr_{0.8}Nb_{0.2}$, *Phys. Rev. B* **40** (1989) 5995–6002.

[147] A. Paskin and G. J. Dienes, Molecular dynamics simulations of shock waves in a three-dimensional solid, *J. Appl. Phys.* **43** (1972) 1605–1610.

[148] W. Petry, A. Heiming, J. Trampenau, M. Alba, C. Herzig, H. R. Schober, and G. Vogl, Phonon dispersion of the bcc phase of group-IV metals. I. bcc titanium, *Phys. Rev. B* **43** (1991) 10933–10947.

[149] S. Ranganathan, K. F. Kelton, and K. Chattopadhyay, 8th international conference on quasicrystals, *J. Non-Cryst. Solids* **334-335** (2004) 1–564.

[150] W. J. M. Rankine, On the thermodynamic theory of waves of finite longitudinal disturbance, *Philos. Trans. R. Soc. London* **160** (1870) 277–288.

[151] W. J. M. Rankine, On the thermodynamic theory of waves of finite longitudinal disturbance, in *Classical Papers in Shock Compression Science* (Edited by Johnson and Chéret), pages 133–147, Springer, New York, (1998).

[152] R. Ravelo, B. L. Holian, T. C. Germann, and P. S. Lomdahl, Constant-stress hugoniostat for following the dynamical evolution of shocked matter, *Phys. Rev. B* **70** (2004) 014103.

[153] E. J. Reed, L. E. Fried, and J. D. Joannopoulos, A method for tractable dynamical studies of single and double shock compression, *Phys. Rev. Lett.* **90** (2003) 235503.

[154] E. J. Reed, J. D. Joannopoulos, and L. E. Fried, Hugoniot constraint molecular dynamics study of a transformation to a metastable phase in shocked silicon, in *Shock Compression of Condensed Matter - 2001* (Edited by M. D. Furnish, N. N. Thadhani, and Y. Horie), volume 620, pages 343–346, (2001).

[155] L. Reinhard, J. L. Robertson, S. C. Moss, G. E. Ice, P. Zschack, and C. J. Sparks, Anomalous-x-ray-scattering study of local order in bcc $Fe_{0.53}Cr_{0.47}$, *Phys. Rev. B* **45** (1992) 2662–2676.

[156] M. H. Rice, R. G. McQueen, and J. M. Walsh, Compression of solids by strong shock waves, in *Solid State Physics* (Edited by F. Seitz and D. Turnbull), volume 6, pages 1–63, Academic, New York, (1958).

[157] Y. Richeng, X. Dapeng, S. Wenhui, and C. Shucheng, Study on quasicrystal formation of $Al_{65}Co_{20}Mn_{15}$ by quenching under high static pressure, in *Proceedings of the XIII AIRAPT Conference: Recent Trends in High Pressure Research*, volume 13, pages 178–180. Pergamon Press, Oxford, (1991).

[158] D. H. Robertson, D. W. Brenner, and C. T. White, Molecular dynamics analysis of shock phenomena, in *High-Pressure Shock Compression of Solids* (Edited by L. Davison and M. Shahinpoor), volume 3, pages 37–57, Springer, New York, (1998).

[159] F. Rösch, C. Rudhart, P. Gumbsch, and H.-R. Trebin, Cleavage planes of icosahedral quasicrystals: A molecular dynamics study,

in *Mater. Research Society Symposium Proceedings* (Edited by E. Belin-Ferre, M. Feuerbacher, Y. Ishii, and D. Sordelet), volume 805, page LL.9.3.1 LL.9.3.6, (2004).

[160] F. Rösch, C. Rudhart, J. Roth, H.-R. Trebin, and P. Gumbsch, Dynamic fracture of icosahedral model quasicrystals: A molecular dynamics study, *Phys. Rev. B* **72** (2005) 014128.

[161] J. Roth, The phase diagram of the Dzugutov potential, unpublished results.

[162] J. Roth, *Thermodynamische Stabilität von Quasikristallen und der Einfluß von Frenkeldefekten.*, Ph.D. thesis, Universität Stuttgart, (1992).

[163] J. Roth, The fluid-solid transition of Dzugutov's potential, *Eur. Phys. J. B* **14** (2000) 449–458.

[164] J. Roth, IMD — A Molecular Dynamics Program and Applications, in *Proceedings of the Workshop on Molecular Dynamics on Parallel Computers* (Edited by R. Esser, P. Grassberger, J. Grotendorst, and M. Lawerenz), page 83. World Scientific, Singapore, (2000).

[165] J. Roth, Jumps in icosahedral quasicrystals, *Eur. Phys. J. B* **15** (2000) 7–13.

[166] J. Roth, Shock waves in quasicrystals, *Mater. Sci. Eng. A* **294-296** (2000) 753–756.

[167] J. Roth, Shock waves in quasicrystals, *Ferroelectrics* **250** (2001) 365–368.

[168] J. Roth, M. Brunelli, D. Bunz, F. Gähler, J. Hahn, M. Hohl, C. Horn, J. Kaiser, R. Mikulla, G. Schaaf, J. Stelzer, and H.-R. Trebin, IMD - a massively parallel molecular dynamics package for classical simulations in condensed matter physics, in *High Performance Computing in Science and Engineering '99* (Edited by E. Krause and W. Jäger), pages 72–81, Springer Heidelberg, (2000).

[169] J. Roth and Ch.Henley, A new binary decagonal Frank-Kasper quasicrystal phase, *Phil. Mag. A* **75** (1997) 861–887.

[170] J. Roth and A. Denton, Solid phase structures for the Dzugutov pair potential, *Phys. Rev. E* **61** (2000) 6845–6857.

[171] J. Roth and F. Gähler, Atomic self-diffusion in quasicrystals: A molecular dynamics study, in *Diffusion in Materials* (Edited by H. Mehrer, Chr.Herzig, N. A. Stolwijk, and H. Bracht), volume 143-147, pages 815–820, (1997).

[172] J. Roth and F. Gähler, Self-diffusion in dodecagonal quasicrystals, *Eur. Phys. J. B* **6** (1998) 425–455.

[173] J. Roth, F. Gähler, and H.-R. Trebin, A molecular dynamics run with 5.180.116.000 particles, *Int. J. Mod. Phys. C* **11** (2000) 317–322.

[174] J. Roth, R. Schilling, and H.-R. Trebin, Stability of monoatomic and diatomic quasicrystals and the influence of noise, *Phys. Rev. B* **41** (1990) 2735–2747.

[175] J. Roth, R. Schilling, and H. R. Trebin, Nucleation of quasicrystals by rapid cooling of a binary melt: A molecular dynamics study, *Phys. Rev. B* **51** (1995) 15833–15840.

[176] C. Rudhart, The $\gamma$-surface of the BI model, private communication.

[177] C. Rudhart, P. Gumbsch, and H.-R. Trebin, Crack propagation in perfectly ordered and random tiling quasicrystals, *J. Non-Cryst. Solids* **334 & 335** (2004) 453–456.

[178] C. Rudhart, P. Gumbsch, and H.-R. Trebin, From crystalline to glassy: Crack propagation modes in decagonal quasicrystals, in *Mater. Research Society Symposium Proceedings* (Edited by E. Belin-Ferre, M. Feuerbacher, Y. Ishii, and D. Sordelet), volume 805, page LL.9.2.1 LL.9.2.6, (2004).

[179] C. Rudhart, F. Rösch, F. Gähler, J. Roth, and H.-R. Trebin, Crack propagation in icosahedral model quasicrystals, in

*High Performance Computing in Science and Engineering 2003* (Edited by E. Krause, W. Jäger, and M. Resch), pages 107–116, Springer Heidelberg, (2003).

[180] A. L. Ruoff, Linear shock-velocity-particle-velocity relationship, *J. Appl. Phys.* **38** (1967) 4976–4980.

[181] M. Sanati and A. Saxena, Domain walls in $\omega$-phase transformations, *Physica D* **123** (1998) 368–379.

[182] M. Sanati and A. Saxena, Landau theory of domain walls for one-dimensional asymmetric potentials, *Am. J. Phys.* **71** (2003) 1005–1012.

[183] J. M. Sanchez and D. D. Fontaine, Structural model for the $\omega$-phase transformation, *J. Appl. Crystallogr.* **10** (1977) 220–227.

[184] G. Schaaf, F. Gähler, C. Kohler, U. Koschella, N. Resta, J. Roth, C. Rudhart, and H.-R. Trebin, Simulation of dislocations in icosahedral quasicrystals with IMD, in *High Performance Computing in Science and Engineering 2001* (Edited by E. Krause and W. Jäger), pages 3–11, Springer, Heidelberg, (2002).

[185] G. Schaaf, J. Roth, and H.-R. Trebin, Dislocation motion in icosahedral quasicrystals at elevated temperatures: numerical simulation, *Phil. Mag. A* **83** (2003) 2449–2465.

[186] G. D. Schaaf, J. Roth, H.-R. Trebin, and R. Mikulla, Numerical simulation of dislocation motion in three-dimensional icosahedral quasicrystals, *Phil. Mag. A* **80** (2000) 1657–1668.

[187] J. Schiøtz, K. W. Jacobsen, and O. H. Nielsen, Kinematic generation of dislocations, *Phil. Mag. Lett.* **72** (1995) 245–250.

[188] J. Schiøtz, T. Leffers, and B. N. Singh, Dislocation nucleation and vacancy formation during high-speed deformation of fcc metals, *Phil. Mag. Lett.* **81** (2001) 301–309.

[189] A. E. Seigel, Strong shock waves in solids, in *High pressure technology* (Edited by I. L. Spain and J. Paauwe), volume 2, pages 481–521, Dekker, New York, (1977).

[190] D. Shechtman, I. Blech, D. Gratias, and J. W. Cahn, Metallic phase with long-range orientational order and no translational symmetry, *Phys. Rev. Lett.* **53** (1984) 1951–1953.

[191] D. P. Shoemaker and C. B. Shoemaker, Icosahedral coordination in metallic crystals, in *Introduction to Quasicrystals* (Edited by M. V. Jarić), pages 27–32, Academic Press, Incorporated, (1988).

[192] S. K. Sikka, B. K. Godwal, and R. Chidambaram, Equation of state at high pressure, in *High-Pressure Shock Compression of Solids* (Edited by L. Davison and M. Shahinpoor), volume 3, pages 1–35, Springer, New York, (1998).

[193] S. K. Sikka, Y. K. Vohra, and R. Chidambaram, Omega phase in materials, *Prog. Mat. Sci.* **27** (1982) 245–310.

[194] A. Silberstein and P. C. Clapp, Modeling and interpretation of tweed microstructures in face-centered-cubic solids, *Phys. Rev. B* **38** (1988) 9555–9566.

[195] S. I. Simdyankin, M. Dzugutov, S. N. Taraskin, and S. R. Elliott, Connection between vibrational dynamics and topological order in simple glasses, *Phys. Rev. B* **63** (2001) 184301.

[196] S. I. Simdyankin, S. N. Taraskin, M. Elenius, S. R. Elliott, and M. Dzugutov, Nature of vibrational eigenmodes in topologically disordered solids, *Phys. Rev. B* **65** (2002) 104302.

[197] J. C. Slater, Debye's theory of specific heats, in *Introduction to Chemical Physics*, pages 222–240, McGraw-Hill, New York, (1940).

[198] C. S. Smith, Metallograpic studies of metals after explosive shock, *Trans. Metall. Soc. AIME* **212** (1958) 574–589.

[199] S. G. Song and G. T. G. III, Microscopic and crystallographic aspects of retained omega phase in shock-loaded zirconium and its formation mechanism, *Phil. Mag. A* **71** (1995) 275–290.

[200] L. Soulard, Shock polar calculation using Gauss' principle of least constraint, in *Shock Compression of Condensed Matter - 1999*

(Edited by M. D. Furnish, L. C. Chhabildas, and R. S. Hixson), volume 505, pages 185–188, (1999).

[201] L. Soulard, Shock polar calculation of inert nitromethane by molecular dynamics simulations, in *Shock Compression of Condensed Matter - 2001* (Edited by M. D. Furnish, N. N. Thadhani, and Y. Horie), volume 620, pages 173–176, (2001).

[202] J. Stadler, R. Mikulla, and H.-R. Trebin, IMD: a software package for molecular dynamics studies on parallel computers, *Int. J. Mod. Phys. C* **8** (1997) 1131–1140.

[203] P. Stampfli, A dodecagonal quasi-periodic lattice in 2 dimensions, *Helv. Phys. Acta* **59** (1986) 1260–1263.

[204] G. K. Straub, B. L. Holian, and R. G. Petschek, Molecular dynamics of shock waves in one-dimensional chains II. Thermalization, *Phys. Rev. B* **19** (1979) 4049–4055.

[205] W.-H. Su, R.-C. Yu, D.-P. Xu, X.-Z. Li, Z. Zhang, and K.-H. Kuo, Formation of six new orthorhombic approximants of decagonal quasicrystal in $Al_{70}Co_{15}Ni_{10}Tb_5$ alloy by quenching under high-static pressure, in *High-Pressure Science and Technology – 1993* (Edited by S. C. Schmidt, J. W. Shaner, and M. Ross), volume 309, pages 481–484, (1994).

[206] D. Tanguy, M. Mareschall, P. S. Lomdahl, T. C. Germann, B. L. Holian, and R. Ravelo, Dislocation nucleation induced by a shock wave in a perfect crystal: Molecular dynamics simulations and elastic calculations, *Phys. Rev. B* **68** (2003) 144111.

[207] H.-R. Trebin, editor, *Quasicrystals. Structure and Physical Properties*, WILEY-VCH, (2003).

[208] H.-R. Trebin, R. Mikulla, and J. Roth, Motion of dislocations in two-dimensional decagonal quasicrystals, *J. Non-Cryst. Solids* **153-154** (1993) 272–275.

[209] R. F. Trunin, Shock compression of condensed materials (laboratory studies), *Phys. Usp.* **44** (2001) 371–396.

[210] D. H. Tsai, An atomistic theory of shock compression of a perfect crystalline solid, in *Acute Characterization of the High Pressure Environment* (Edited by E. C. Lloyd), pages 105–122, Nat. Bur. Stand, Washington, DC, USA, (1971).

[211] D. H. Tsai and C. W. Beckett, Shock wave propagation in cubic lattices, *J. Geophys. Res.* **71** (1966) 2601–2608.

[212] D. H. Tsai and C. W. Beckett, Shock wave propagation in a two-dimensional crystalline lattice, in *Behaviour of Dense Media Under High Dynamic Pressures*, pages 99–108, Gordon and Breach, New York, (1968).

[213] D. H. Tsai and R. A. MacDonald, Second sound in a solid under shock compression, *J. Phys. C* **6** (1973) L171 L175.

[214] D. H. Tsai and R. A. MacDonald, An atomistic view of shock wave propagation in a solid, *High Temp. High Pres.* **8** (1976) 403–418.

[215] K. Urban, J. Mayer, M. Rapp, M. Wilkens, A. Csanady, and J. Fidler, Studies on aperiodic crystals in Al-Mn and Al-V alloys by means of transmission electron microscopy, *J. Phys. (Paris) Coll. C3* **47** (1986) 465–475.

[216] D. C. Wallace, Flow process of weak shocks in solids, *Phys. Rev. B* **22** (1980) 1487–1494.

[217] D. C. Wallace, Computer simulation of nonequilibrium process, in *Shock Waves in Condensed Matter* (Edited by Y. M. Gupta), pages 37–49. Plenum, New York, (1986).

[218] C. M. Wayman and H. K. D. H. Bhadeshia, Phase transformations, nondiffusive, in *Physical Metallurgy* (Edited by R. W. Cahn and P. Haasen), volume II, pages 1546–1548, North Holland, Amsterdam, (1996).

[219] J. Weertman, Moving dislocations in a shock front, in *Shock Waves and High Strain Rate Phenomena in Metals* (Edited by L. E. Murr and M. A. Meyers), pages 469–486, Plenum, New York, (1981).

[220] S. Wenhui, X. Dapeng, X. Xingtang, Y. Richeng, and X. Zhiming, The formation of quasicrystal in $Al_{0.77}Mn_{0.19}Yb_{0.04}$ by quenching under high static pressure, in *Proceedings of the XIII AIRAPT Conference: Recent trends in High Pressure Research*, volume 13, pages 181–183. Pergamon Press, Oxford, (1991).

[221] M. Widom, K. J. Strandburg, and R. H. Swendsen, Quasicrystal Equilibrium State, *Phys. Rev. Lett.* **58** (1987) 706–709.

[222] J. C. Williams, D. D. Fontaine, and N. E. Paton, The $\omega$-phase as an example of an anusual shear transformation, *Met. Transactions* **4** (1973) 2701–2708.

[223] K. Yano and Y. Horie, Discrete element modeling of shock compression of polycrystalline copper, *Phys. Rev. B* **59** (1999) 13672–13680.

[224] K. Yano and Y. Horie, Mesomechanics of the $\alpha - \epsilon$ transition in iron, *Int. J. Plast.* **18** (2002) 1427–1446.

[225] B. S. Yilbas and A. F. M. Arif, Laser short pulse heating and elastic-plastic wave generation, *Jpn. J. Appl. Phys.* **39** (2000) 5879–5888.

[226] V. Yu.Klimenko and A. N. Dremin, Structure of a shock-wave front in a solid, *Sov. Phys. Dokl.* **25** (1980) 288–289.

[227] I. Yu.Smolin, P. A. Makarov, D. V. Shmick, and I. V. Savlevich, A micropolar model of plastic deformation of polycrystals at the mesolevel, *Comp. Mat. Sci.* **19** (2000) 133–142.

[228] Y. Zel´dovich and Y. Raizer, *Physics of Shock Waves and High-Temperature Hydrodynamic Phenomena*, Dover, Mineola, (2002).

[229] F. H. M. Zetterling, M. Dzugutov, and S. Lidin, $\gamma$ -brass crystallization in a simple monatomic liquid, in *Quasicrystals - Preparation, Properties and Applications* (Edited by E. Belin-Ferre, P. A. Thiel, A.-P. Tsai, and K. Urban), volume 643, page K9.5.1 K9.5.6, (2001).

[230] V. V. Zhakhovskiĭ, K. Nishihara, S. I. Anisimov, and N. A. Inogamov, Molecular-dynamics simulations of rarefaction waves in media that can undergo phase transitions, *JETP Lett.* **71** (2000) 241–248.

[231] V. V. Zhakhovskiĭ and S. V. Zybin, Numerical simulations of shock waves in crystalline solid by nonequilibrium molecular dynamics, *Seminário Brasileiro de Análise* **49** (1999) 635–650.

[232] V. V. Zhakhovskiĭ, S. V. Zybin, and K. Nishihara, Orientation dependence of shock structure in L-J crystal, in *Proceedings of of the Japanese Symposium on Shock Waves*, page 262, (2000).

[233] V. V. Zhakhovskiĭ, S. V. Zybin, K. Nishihara, and S. I. Anisimov, Shock wave structure in L-J-solid, in *Proceedings of of the Japanese Symposium on Shock Waves*, pages 241–244, (1999).

[234] V. V. Zhakhovskiĭ, S. V. Zybin, K. Nishihara, and S. I. Anisimov, Shock wave structure in Lennard-Jones crystal via molecular dynamics, *Phys. Rev. Lett.* **83** (1999) 1175–1178.

[235] V. V. Zhakhovskiĭ, S. V. Zybin, K. Nishihara, and S. I. Anisimov, Orientational dependence of shock structure with melting in L-J crystal from molecular dynamics, *Progress of Theoretical Physics Supplement* **138** (2000) 223–228.

[236] M. F. Zhorovkov and V. V. Kulagina, Phonon anomalies and martensitic transitions, *Russ. Phys. Journal* **36** (1993) 917–923.

[237] S. V. Zybin, M. L. Elert, and C. T. White, Orientation dependence of shock-induced chemistry in diamond, *Phys. Rev. B* **66** (2002) 220102(R).

[238] S. V. Zybin, V. V. Zhakhovskiĭ, M. L. Elert, and C. T. White, Molecular dynamics studies of orientation dependence of shock structure in solids, in *Shock Compression of Condensed Matter - 2003* (Edited by M. D. Furnish, N. N. Thadhani, and Y. Horie), volume 706, pages 310–318, (2003).

# Acknowledgment

First of all I would like to thank my wife Antje and my children Jonathan, Stephan and Althea for supporting me and for their patience when their father was working day and night.
I am especially indebted to Ralf Mikulla who has pointed out to me a number of problems in earlier shock wave simulations and has supplied me with valuable references.
A lot of thanks to Kai Kadau from Los Alamos National Lab for collaborating. The chapter about solitary waves is the outcome of this teamwork. Part of the research was carried out during a three-week stay at LANL. Financial support from LANL and SFB 382 is gratefully acknowledged.
I furthermore acknowledge helpful discussions with Brad L. Holian, Peter S. Lomdahl, Domë Tanguy, Sergei Zybin, and Jean-Bernard Maillet about shock waves.
At the ITAP, I thank Ulrich Koschella for running the computer system instead of me, Franz Gähler for keeping IMD in good shape and implementing new features, and especially Christoph Rudhart for the discussions about the $\gamma$-surface and other properties of binary icosahedral model. Franz Gähler also provided the data for the dodecagonal quasicrystals. Christoph Rudhart helped me with the LaTeX problems, and Frohmut Rösch carefully read the manuscript. I am grateful to all other members of the group and to our secretaries Ulrike Mergenthaler, Sabrina Heldele, and Simone Blümlein.
This habilitation thesis will be judged by some referees as part of the habilitation procedure. I thank them in advance for their efforts. I also thank my "Mentorengruppe" at the University of Stuttgart, consisting of Profs. Denninger, Hermann, Muramatsu, Mahler, Trebin, for supporting my habilitation.
Last but not least I am grateful to Prof. Trebin. He encouraged me to pursue a scientific career and always strongly supported this habilitation work. He provided an environment in which I could freely follow my scientific interests. Many thanks.